Engineering and Applied Science Theses & Dissertations

McKelvey School of Engineering

Summer 8-15-2020

New Modeling Approaches for the Prediction of Combustion Pollutants

Phillip R. Johnson
Washington University in St. Louis

WASHINGTON UNIVERSITY IN ST. LOUIS

McKelvey School of Engineering
Department of Energy, Environmental, and Chemical Engineering
Center for Aerosol Science and Engineering

Dissertation Examination Committee:
Rajan Chakrabarty, Chair
Benjamin Kumfer, Co-Chair
Richard Axelbaum
Pratim Biswas
Chun Lou
Jay Turner
Gregory Yablonsky

New Modeling Approaches for

the Prediction of Combustion Pollutants

by

Phillip R. Johnson

A dissertation presented to
The Graduate School
of Washington University in
partial fulfillment of the
requirements for the degree
of Doctor of Philosophy

August 2020
St. Louis, Missouri

Table of Contents

List of Tables

List of Figures

Nomenclature

Latin:

A   fitting constant

A_s surface area (m^2)

B   fitting constant

C   fitting constant

$[C_nH_m]$ concentration of species $(kmol/m^3)$

C_s leading constant

C_{sp} leading constant (smoke-point basis)

CFD   computational fluid dynamics

D   Delichatsios (et al.) model

d_p particle diameter (m)

D   fitting constant

E   fitting constant

F   fitting constant

$f(S)$ surface area function

f_v soot volume fraction

G similarity parameter for radial velocity $(kg/m^3 \cdot s)$

K   extinction coefficient

K_L strain rate

K strain rate $(1/s)$

KG   Khan-Greeves model

LL   Leung-Lindstedt model

La   Lindstedt model, type a

Lb   Lindstedt model, type b

Lc   Lindstedt model, type c

Ld Lindstedt model, type d

LES   Large Eddy Simulation

m   refractive index

M   Moss (et al.) model

MB   Moss-Brookes model

MBH   Moss-Brookes-Hall model

n particle number $(\#_{part}/kg_{gas})$

n^* seed particle number $(\#_{part}/kg_{gas})$

N_{AV} Avogadro's number

$N_{C,inc}$ number of Carbon atoms per nascent soot particle

n_{soot} number of particles per kg of gas

n_T soot precursor (Tesner model)

N_T soot particle (Tesner model)

P_F fuel partial pressure

P_F fuel partial pressure (Pa)

psp particle stagnation plane

RANS Reynolds-Averaged Numerical Simulation

Sc_T turbulent Schmidt number

svf soot volume fraction

Stk Stokes number

T gas temperature.

T_a activation temperature

T   Tesner (et al.) model

T temperature (K)

T_A Arrhenius temperature (K)

u gas velocity

u axial velocity (m/s)

v_t thermophoretic velocity

W_i molecular weight of species i $(kmol/kg)$

X_i mole fraction of species i

X_F fuel mole fraction

Y_i mass fraction of species i

Y_F fuel mass fraction

Y_{F0} fuel mass fraction in the fuel inlet

Y_{soot} soot mass fraction

$Y_{F,B}$ mass fraction of fuel, in a burning mixture

$Y_{F,U}$ mass fraction of fuel, in an unburning mixture

$Y_{O,U}$ mass fraction of oxidizer, in an unburning mixture

z   axial dimension

Z mixture fraction

Z_{cr} critical mixture fraction at which soot can being to form

Z_{ox} oxidative mixture fraction at which soot can no longer form

Z_{st} mixture fraction at stoichiometry

Greek:

β coagulation kernel

ζ either Y_i or n (as applicable)

ν stoichiometric quantity

λ stoichiometric ratio

λ_{PO} stoichiometric ratio of the primary air

ρ gas mass density (kg/m^3)

ρ_S soot particle mass density (kg/m^3)

τ characteristic reaction time

ϕ local equivalence ratio

Φ normalized local equivalence ratio

Φ_{cr} critical normalized local equivalence ratio

χ HACA variable

ω_{coag} soot particle coagulation rate

ω_{form} soot formation rate (mature particle) $(kg/m^3 \cdot s)$

ω_{inc} soot inception rate (nascent particle) $(kg/m^3 \cdot s)$

ω_n overall soot number reaction rate $(kg/m^3 \cdot s)$

ω_{oxid} soot oxidation reaction rate $(kg/m^3 \cdot s)$

ω_s overall soot mass reaction rate $(kg/m^3 \cdot s)$

ω_{sg} soot surface growth reaction rate $(kg/m^3 \cdot s)$

<u>**Acknowledgments**</u>

Dedicated to my family:

To my father and mother, who prepared me for this journey and

To Abigail, who walked with me through it.

Ἅγιος ὁ Θεός, Ἅγιος ἰσχυρός, Ἅγιος ἀθάνατος, ἐλέησον ἡμᾶς

Abstract of the Disseration

New Modeling Approaches for the Prediction of Combustion Pollutants

by

Phillip Johnson

Doctor of Philosophy in Energy, Environmental, and Chemical Engineering

Washington University in St. Louis, 2020

Rajan Chakrabarty, Associate Professor, Chair

Benjamin Kumfer, Research Assistant Professor, Co-Chair

Combustion processes are ubiquitous to human technological development and provide many benefits such as large-scale power generation for electricity and transportation along with residential and commercial heating for manufacturing, cooking, and warmth. However, these various processes can also have harmful effects on human health and the environment via emission of CO_2 and other pollutants such as NOx and particulate matter (PM; often in the form of soot). For these reasons, there is a continued need for controlling, improving, and optimizing combustion processes. Modeling of these processes provides powerful insights into system-level dynamics and their control. Due to the size and complexity of industrial-scale combustion systems, there is a pressing need for the development of computationally-inexpensive models that can accurately predict gaseous and PM emissions. The research described in this dissertation addresses this need by: 1) careful evaluation of existing soot formation models for application in oxygen-enriched flames, 2) development of new, robust soot modeling capabilities with improved accuracy for flames outside of the normal fuel/air condition, and 3) production of a large data set for the

development of machine learning-based algorithms for predicting pollutant emissions under a wide range of combustion operating conditions.

Over the past decades, several semi-empirical soot models have been developed for specific applications with unique characteristic timescales and/or validated only under fuel-air combustion conditions. Hence, their universal use, especially under oxygen-enriched combustion conditions, could lead to highly inaccurate predictions. Twelve semi-empirical models (1-step or 2-step) are evaluated based on their ability to respond to changes in stoichiometric mixture fraction (Z_{st}) and strain in a series of ethylene counterflow flames spanning across the sooting-to-non-sooting (yellow to blue) transition. Results show that no existing model is able to predict a blue flame when Z_{st} is increased beyond the experimentally-measured sooting limit.

Motivated by this finding, a novel modeling approach is presented to account for the unique flame characteristics at elevated-Z_{st} environments and their effect on soot formation. This modeling approach is designed to capture both the formation and the reversible processes that occur on the fuel-side of a diffusion flame in a robust yet simple manner and can be utilized in many industrial combustion applications. A new semi-empirical formulation is presented that achieves this goal. In addition, extensions are presented for two widely-used semi-empirical models (Leung-Lindstedt and Moss-Brookes) which would otherwise be inaccurate at these conditions. Upon application of this approach to counterflow flame systems, the predicted soot volume fraction profiles agree well with experimental findings reported by previous studies under low Z_{st}. This improved approach also resulted in the prediction of blue (soot-free) limit conditions in a non-premixed counterflow flame for the first time. Thus, the performance of semi-empirical soot formation models can be dramatically improved when the reversible nature of soot formation at high temperature is considered.

The next goal was to develop a machine-learning based modelling approach for combustion systems. As part of this collaborative effort, a series of experiments were performed using a lab-scale (25 kW) combustor that was operated under varying the fuel and air ratios. Measurements were made of temperature profiles along the reactor wall and gas composition and pollutants (CO, NOx, PM) in the exhaust. A series of tests were performed totaling 60 hours of runtime and 140,000 data points corresponding to each parameter. Findings from these experiments highlight a series of trends in the reactor: low and high primary air flows lead to elevated PM and NOx emission levels, respectively; NOx levels correlate with varying swirl ratios under fixed fuel / air ratio. Based on the generated data set, a model may be developed to accurately predict pollutant levels and subsequently recommend optimized operating conditions for the combustion system.

Chapter 1: Introduction

"For what is more beautiful than a fire, with all the vigor of its flames and the splendors of its light? And what more useful with its heat, its comfort, and its help in cooking? And yet nothing can cause more distress than the burns inflicted by fire. Thus a thing which is dangerous and destructive in some situations proves to be of the greatest utility when properly employed. Who could give a complete account of all the useful functions of fire in the whole universe?"

– Augustine of Hippo, de Civitate Dei, X.4 (ca. 5th century AD)

1.1   Overview / Motivation

Since these words were written down in late antiquity, human dependence on combustion processes has not yet subsided. Ovens continue to generate heat for cooking with increasing levels of sophistication. Residential and bathhouse heat are still provided by burning natural gas. Even when these processes are driven by electricity, even then a majority of the energy source is derived from combustion. While the candle as a source of luminosity has been eclipsed by the light bulb, it is still a fire which gives light.

The important of combustion processes has drawn large scientific interest to unravel the many complexities of these processes and to address many challenges which affect society at large. An example of a highly-complex process which is encountered by most humans is related to that visibly yellow region of a flame which is due to incandescent carbonaceous particulate matter, referred to as 'soot'. This material is typically a fractal aggregate of micrometer scale and composed of spherical graphitic monomers of nanometer scale. Soot is produced in a wide range of combustion processes and to this day remains a significant area of research in the combustion community. There are unresolved questions related to its formation and unsolved challenges for applications such as engines, gas turbines, power generation furnaces, and fires of various sorts.

Soot can behave as a "good aerosol", enhancing radiation when heat transfer is desired, and it can behave as a "bad aerosol" when emitted into the atmosphere or around human populations. It is therefore important to control and accurately predict soot formation to achieve optimal combustion conditions while preventing harmful emissions and modeling provides an avenue to achieve this aim.

1.2 Modeling Combustion Processes

An ideal model is like a "law" of physics, which can be universally applied in a controlled environment with little margin of error. Unfortunately, almost all real-world applications involve levels of complexities that require scientists and engineers to resort to either a) deeper and more fundament levels of physics and chemistry that can constrain the scope of a project due to current computational limits or b) adding empiricism in some form to achieve a modeling tool which becomes 'simple'; i.e., it achieves goals for accuracy but at the cost of constraining the scope of applicability. In between these two extremes lies a spectrum of available models and modeling techniques.

This dissertation will focus on two different modeling techniques which are relevant to predicting these pollutant quantities and possible ideal operating conditions: semi-empirical soot modeling for non-traditional flames and machine-learning algorithms for industrial combustion processes. The bulk portion of this research is focused on the former task and the remainder of the introduction reflects this focus. But the reader should be reminded that the particular challenge described here is related to a wide range of applications where modeling efforts can be challenged and improved for novel flame environments.

1.3 The Challenges of Novel Flame Environments

The study of soot formation has a long-research history and many aspects of it can be considered as a mature field, barring notable exceptions such as the open questions related to precursors and particle inception. Soot has been studied in scales ranging from the well-known laboratory flames such as the coflow, counterflow, or shock-tube configurations to gas turbines and engines to industrial coal burning and forest wildfires. Most of the soot studies in these applications have been investigated with compositions close to that of pure fuel burning in air with little excess oxygen. However, some important combustion applications make use of non-traditional compositions which can significantly affect soot formation.

One of these non-traditional applications is oxygen-enhanced combustion (OEC), which generally describes a process where oxygen is used to supplement or replace air in the oxidizer of the flame. This technique has found uses in areas such as glass production, metallurgy, and developing power generation techniques such as oxy-coal combustion.

Soot formation is known to be strongly affected by oxygen enrichment. Flames can even transition from soot-producing (yellow) to non-sooting (blue) through the combination of oxygen enrichment and fuel dilution [1, 2]. This result occurs even when the stoichiometric flame temperature is held constant and has been confirmed in a wide variety of non-premixed flame configurations including normal and inverted laminar coflow flames [3, 4], counterflow flames [5], and spherical flames produced in microgravity [6]. Soot formation is also strongly influenced by the characteristic time of the flame, as evidenced by the hydrodynamic suppression of soot formation in a coflow flame [7] and upon increasing strain rate (K) in the counterflow flame [5, 8]. This result displays the importance of the flow field and residence time in the system of interest.

For these reasons described, there is still a need to predict soot quantities in systems using OEC or varying the characteristic time. While the changes to soot under these conditions have been studied above, there has not yet to date been a model capable of predicting soot quantities for such flames.

1.4 Soot Modeling Scope

The importance of capturing soot formation processes and accurately modelling them quantitatively can be attested to by the fact that the most recent model referred in this work is a mere five years old while the earliest is nearly fifty. Thus soot modeling is a research field with both a history of progress and also contemporary motivation. These models span a range of complexity and accuracy and are discussed in greater detail in chapter two below.

Tremendous progress has been made towards the development of detailed soot formation models, which involve large chemical reaction mechanisms and aerosol dynamics to capture the complex processes of fuel pyrolysis, particle inception, growth and oxidation [9-16]. However, such models are often too computationally expensive to be included in CFD simulations of industrial systems, which are the targets of this work. There remains a need for less complex soot formation models that are easy to use and give a prediction of soot volume fraction with reasonable accuracy over a wide range of combustion conditions. For these reasons, some commercial CFD software packages, such as ANSYS FLUENT [17], include empirical or semi-empirical models for soot formation. However, many such models were developed and validated only for specific laboratory conditions and are limited to combustion of pure fuel in air. Therefore, the accuracy of these existing models may be questioned when applied to other situations such as oxygen-enhanced combustion, or oxy-combustion for carbon capture [18].

1.5　Objective and Outline

The goal of this research is to provide new modeling capabilities for predicting pollutants such as soot. The following chapter will briefly discus the theory of soot formation and give a review of various semi-empirical soot models and an overview of detailed modeling methods. Chapter 3 will show how these non-traditional combustion environments can significantly alter these soot formation processes. Chapter 4 will describe a methodology developed to evaluate soot models for non-traditional conditions in a counterflow flame. Chapter 5 will display results of the evaluation. Chapter 6 will unveil a series of new models and extensions to existing models which are capable of accurately predicting soot in these environments. Chapter 7 will introduce experimental data which will be used for training a machine learning-based simulation tool for optimizing combustion operating conditions for efficiency and emissions. Conclusions and recommendations for future work are given in Chapter 8.

Chapter 2: Review of Soot Formation Theory

and Modeling

2.1   Theory of Soot Formation

2.1.1 Soot Chemistry

Soot generation has been commonly described through the processes of gas pyrolysis, particle inception, and surface growth. Soot particles will also coagulate while its mass can be consumed via oxidation. These processes are highly dependent on chemical composition, temperature, and available reaction time of the surrounding flame environment.

Combustion of hydrocarbons converts reactants to products of CO_2 and H_2O if sufficient oxygen is available. During this process intermediates are formed as the parent fuel is pyrolized, an important intermediate being acetylene (C_2H_2). Indeed, the formation of C_2H_2 from an aliphatic gaseous fuel is thermodynamically favorable due to its entropy increase from de-hydrogenization while being significantly endothermic [9]. Thus high heat, as provided in combustion, is needed to transform aliphatic fuels into C_2H_2. Given sufficient fuel, temperature, and time and insufficient oxygen, aromatic compounds will form. The first aromatic ring (benzene, A_1) has been referred to as a "bottleneck" to soot formation [19]. Once this species is created, it grows via multiple pathways, two prevalent ones being hydrogen-abstraction-carbon-addition (HACA) and aromatic condensation. As the name implies, HACA describes a process where: 1) H^+ radicals attack the hydrocarbon surface to create an open site and H_2 (increasing entropy), 2) C_2H_2 bonds at the open site. This process is repeated and has been used to explain both initial ring generation and the

6

growth of additional rings on pre-existing aromatics. Also, aromatics can directly 'condense' onto other existing aromatics to create larger compounds. Through these processes, poly-cyclic aromatic hydrocarbons (PAH) are formed. Experimental evidence has long pointed to the coinciding of abundant PAH species with that of nascent soot. For this reason, these compounds have been thought to be the precursors for soot particles.

2.1.2 Soot Inception

Soot particulate has been extracted from experiments on soot inception flames, where flame conditions have been such that only nascent, rather than mature soot is formed. These experiments have shown that soot monomers can be characterized by a graphitic shell encasing an amorphous core. These results have given risen to a few theories about soot inception. It has been proposed that PAHs collide and form dimers, trimers, and transition to large amorphous PAH before collapsing into a spherical particle, a soot monomer. Pyrene (A_4) is a commonly referenced PAH for the dimerization process, which has been used in detailed models as an inception step (see modeling discussion below). However, it has been demonstrated that A_4 dimers are thermodynamically unstable at flame temperatures [20]. To achieve thermodynamic stability, PAHs must be a minimum size of coronene (A_7) [9]. However, it has also been shown that the prevalence of PAH species rapidly decreases, at a rate of approximately an order of magnitude per additional ring size. An alternative model of soot inception has been recently proposed [21] where resonantly-stabilized radicals (RSR) were observed in high quantities and were hypothesized to be an inception precursor species through a chain-reaction-like process. Even with these new alternatives, the question of soot inception is still a contested area of research.

The inception step has shown a large amount variety among semi-empirical models. For example, it has been modeled as a one-step conversion from fuel, acetylene, or benzene and phenol

(see Task 1.1). Species-based formulations may be problematic, as the inception process itself is not well understood at a fundamental level. Pyrene dimerization has been proposed to describe the nucleation step [13, 16, 22, 23], although such a dimer has been shown to be unstable for temperatures experienced in a flame [9, 20, 24]. Since the dimerization of polycyclic aromatic hydrocarbons (PAH) much larger than pyrene, such as coronene, have been shown to be more stable in flames [9], recent detailed models have begun to account for such larger PAH [25, 26]. However, there are still questions regarding the chemistry behind the inception process [27] which must be addressed.

2.1.3 Soot Growth & Destruction

Once nascent particles are formed, they growth through surface-based growth processes. These reactions account for the dominant pathways of mass addition to the particles; inception merely provides the seed to grow upon. There is a plethora of potential growth reactions on a soot particle in the hot bath of hydrocarbons it encounters during the combustion process. However, unlike the inception step, there is a general consensus on surface growth processes which can qualitatively be categorized as either HACA reactions or aromatic condensation, both of which are described above. Soot will also be attacked via surface-based oxidation in the presence of oxygen and high temperatures. Flames which emit soot due to insufficient oxidative attack are referred to as "smoking".

Soot also undergoes classical aerosol processes such as coagulation, where monomers collide and form aggregates; soot has a fractal dimension of 1.8. Soot is also affected by particle transport processes such as thermophoresis due to the large temperature gradients experienced in a flame. Mature soot particles have historically been considered sufficiently large enough to ignore the effect of Brownian motion for modeling purposes in flames with significant gas velocities.

2.2 Overview and Types of Models

As mentioned above, soot formation modeling is a field which lacks neither depth nor breadth. To distinguish models, then, some important metrics should be considered. The ideal soot model should be measured in terms of its 1) accuracy, 2) simplicity, and 3) generality. *Accuracy* denotes the ability of a model to predict measured quantities, of which is a hierarchy; for example, all models seek to predict fraction and particle number, while obtaining size distributions and morphology requires more detailed models. *Simplicity* describes the aim to efficiently capture information; good models are 'concise' but not 'simplistic' in the naïve connation of the term. In comparing two models which have the same level of accuracy, the simpler model should be seen as advantageous, because it efficiently captures the information. However, this judgment is related to the desired level of accuracy; a simpler model may be sufficient for capturing soot fraction whereas a less-simple model might be necessary for capturing the size distribution. *Generality* denotes that a model should be widely applicable; for present purposes, this can mean a wide range of fuels, flame conditions, and flame types including, but not limited to, turbulent systems and fuel-dilute / oxygen-enriched systems.

The most recent comprehensive review on semi empirical soot modeling was published by Kennedy in 1997 [28]. Since then several improvements to these models have been proposed [29-35]. In this review, models were distinguished between empirical, semi-empirical, and detailed types. Empirical models were those fitted to certain quantities thought to be relevant to soot generation; an example used is by Khan [36]. Semi-empirical models were stated to consider more of physics behind the soot formation process; examples listed in this category included the models of Moss, Leung-Lindstedt, and Delichatsios below. Our review classifies these models and several others post-1997 collectively as "semi-empirical".

Among the semi-empirical models considered in this study, a classification is made between one-step or two-step. For some models, generation is considered through one formation term that produces *mature* soot particles. For other models, generation is modeled through separate inception and surface growth steps. The inception term produces *nascent* soot particles. This distinction between formation and inception will remain throughout this proposal. In the first case, the formation rate of soot, ω_s, is calculated by assuming that mature soot particles are formed directly from a gaseous precursor species in one step. In a two-step model, soot mass formation occurs by both particle inception and surface growth, as shown in Eq. (2-1). In this case, the particle population balance equation must also be considered, and assumptions about the incipient particle size and particle morphology must be made in order to calculate the particle surface area available for growth. The soot particle number formation rate, ω_n, is given in Eq. (2-2), which includes particle inception and loss by coagulation.

$$\omega_s = \omega_{inc} + \omega_{sg} \tag{2-1}$$

$$\omega_n = \frac{N_{Av}}{MW_C N_{C,inc}} \omega_{inc} - \beta n^2 \tag{2-2}$$

Where the various reaction rates are Arrhenius-type functions of concentration, temperature, physical constants, and empirical constants.

Finally, detailed models are full chemical mechanisms which can range from twenty equations to a several hundred. What distinguishes these models as detailed is that they require detailed chemistry, notably for the inception step(s) which requires the use of one or more PAHs (minimum size A_4) as a precursor. Additionally, reactions account for surface site openings (which requires knowledge of hydrogen radical species), surface HACA growth, aromatic condensation, and oxidation. This level of detail is in-line with an attempt to match the reactions as close as

possible to the current understanding of precursor species. These models also account for coagulation and track particle size distributions through various methods (see further below).

Each stage of the modeling hierarchy has its advantages and challenges. Semi-empirical models have the advantage of low computational cost (simplicity), which makes them desirable in many practical applications, which can be large-scale, three-dimensional, and turbulent and where the addition of each conservation equation adds large computational costs and time to a simulation. However, even with the low computational cost, the generality of many of these semi-empirical models is under question. Many of them are fine-tined to a specific set of conditions: flame type (pre-mixed, non-pre-mixed) or configuration (co-flow, counter-flow, furnace), and fuel type (methane, ethylene, diesel fuel, coal, etc.). Deviation from these parameters results in a need to re-configure some of the model constants. This re-fitting requirement compromises the predictive capability of a model for untested conditions. Further, these models show deviations concerning oxidative species and surface area dependences which pertain to the flames they were validated against. Other criticisms note that semi-empirical models have inception rates based on the fuel, acetylene, benzene, pyrene, or lumped PAH concentrations, which are not considered true precursors; however, as will be noted shortly, a criticism of inception modeling also extends to detailed models.

On the other hand, detailed models require greater computational expense with the presumed advantage of greater accuracy. Indeed, these models can provide details to a level that cannot be obtained with semi-empirical models (e.g. the size distribution). However, the open status of the inception question has generated a series of problems for modelers which must compensate in various ways (adjusting PAH concentration, creating sticking efficiencies for pseudo-irreversible dimerization, etc.); these steps are discussed in greater detail below. Since the

11

inception step is a bottleneck for the entire soot formation process, improvement of these models is a continual work-in-progress. In brief, while detailed soot models perhaps show greater long-term promise for sufficiently capturing all relevant soot quantities, it should not be immediately assumed that these models in their current state will always provide a tremendous improvement of accuracy over other models for any given flame.

These criticisms notwithstanding, the results of this research will demonstrate that semi-empirical models have the capability of matching the accuracy of detailed models in terms of soot mass fraction and both model types can match experimentally measured soot fraction relatively well in certain circumstances. This research has focused primarily on semi-empirical models due to considerations of computational expense, with some additional results for detailed models included to highlight a conceptual point about how soot formation is generally approached by modelers. However, little-to-no modeling of either kind has been done for flames with an enriched oxidizer where the accuracy of such models remains an open question. Before addressing this question, individual models are discussed in greater detail to serve as a review and to provide information which will benefit the subsequent analysis.

2.3 Semi-Empirical Models

Despite a near consensus on which processes to model (inception, surface growth, coagulation, and oxidation), the modeling description of these processes are somewhat divergent. The nucleation species could be acetylene, benzene, or PAH. Most surface growth processes model HACA using acetylene, with some differences in the importance of surface area; some, but not all include PAH condensation. Oxidation is not always included, and its form varies widely with differences among the oxidizing species; some use OH, others O_2. Questions reside concerning the

role of surface; if included, it is usually on the order of 1 or ½ (square root). Units for all equations are: kg, m, s, Pa, K.

Khan and Greeves (KG) developed one of the earliest soot formation models for diesel engines, which was considered a pre-mixed system [36, 37]. The model, as originally proposed is:

$$\omega_{form} = 4.68 * 10^5 \frac{V_u}{V_{ntp}} \, \phi^3 \, P_F \, e^{-\frac{20,202}{T}} \tag{2-3}$$

Where V_u and V_{ntp} are jet velocities in the intake. The velocity terms are commonly dropped when this model is used in applications other than diesel engines. The equivalence ratio exponent was found in Khan and Greeves [36] by data fitting. Modifications to this exponent have been proposed [38, 39]. This model has found frequent usage in coal combustion for traditionally fired systems [40, 41] and for oxy-coal combustion [42]. In these cases, the *local* equivalence ratio is used for ϕ and the variables pertaining to jet velocities have been removed. Examples of these modified versions are shown in Eqs. 2-4, 2-5.

$$\omega_{form} = 1.5 \, \phi^3 \, P_F \, e^{-\frac{2,000}{T}} \tag{2-4}$$

and is shown in Eq. (2-5):

$$\omega_s = 4.68 * 10^5 \, \phi^3 \, P_F \, \exp\left(-\frac{20,202}{T}\right) \tag{2-5}$$

Lautenberger, et al. [31] developed a model for non-premixed coflow flames using separable functions of mixture fraction (*Z*) and temperature by assuming that soot was formed in a small region in mixture fraction space. Soot formation was suppressed except for a region where non-zero soot production is described by 3rd-order mixture fraction polynomials fitted to experimental

13

data. Fitting occurs between points of onset, peak, and termination of formation rate. These quantities are assumed to be multiples of Z_{st} with a 'fuel-independent' constant.

$$\omega = \omega_{form}(Z,T) - \omega_{oxid}(Z,T) \tag{2-6}$$

$$\omega_{form} = f_{form}(Z)g_{form}(T); \; \omega_{oxid} = f_{oxid}(Z)g_{oxid}(T) \tag{2-7}$$

This assumption was justified on the claim that in heavier-sooting flames or regions of a flame, homogenous processes dominate. As a result, volumetric formation is more important than surface-dependent formation. However, this formulation leads to an inability to reproduce the blue soot-free zone in lightly-sooting flames without manually suppressing the formation at low residence times. Observing that soot forms in a parabolic trend in mixture fraction space, formation suppression is accomplished by forcing the rate to be zero until a certain mixture fraction limit Z_H, rising to peak at Z_P, and again becoming zero at Z_{st}. A similar (negative) trend was found for the oxidative side of stoichiometry. All of these quantities of Z are assumed to be multiples of Z_{st}, with the multiplicative constant being fuel-independent. The $f(Z)$ $f_{form}(Z)$ functions used in the models were taken to be a 3rd-order polynomials fitted to experimental data. Likewise, $g_{form}(T)$ was also taken to be a 3rd order polynomial (note this is a rare deviation form Arrhenius dependence seem in most models), while $g_{oxid}(T)$ increased linearly with temperature. These relationships are shown in Table 2-1.

Parameter	Location
ψZ_L	$1.05 * Z_{st}$
ψZ_P	$1.77 * Z_{st}$
ψZ_H	$2.05 * Z_{st}$
$f_{form}(\psi Z_P)$	$1.10 \text{ kg/m}^3\text{s}$

Table 2-1: Fitting parameters for mixture fraction polynomial, Lautenberger model.

Parameter	Location
T_L	T = 1375K
T_P	T = 1625 K
T_H	T = 1825 K

Table 2-2: Fitting parameters for temperature polynomial, Lautenberger model.

Relationships for temperature fitting are in Table 2-2. An example of the mixture fraction polynomial for an ethylene-air flame (Z_{st} =0.064) is below:

$$f_{form}(Z) = -16986 * Z^3 + 4418.1 * Z^2 - 349.43 * Z + 8.69 \qquad (2\text{-}8)$$

This model was compared to non-premixed co-flow flames. While this model provides applicability to various fuels through its Z_{st} formulation, these relationships are only valid for low-Z_{st} flames. As Z_{st} is increased, these relationships result in the widening of the soot formation zone, which contradicts experimental data. Further, if $Z_{st} > 0.465$ then $Z_H > 1$ (a physical impossibility), and thus this formulation breaks down at high $Z_{st.}$ These issues render this model inapplicable to soot modeling for oxygen-enhanced combustion.

The Delichatsios (D) group has developed a series of semi-empirical soot models [32-35, 43] which have been validated for several types of non-premixed flames. Initially, the model, shown in Eq. 2-9, predicted that soot formation was proportional to fuel mass fraction, in line with experimental results [44, 45]:

$$\omega_{form} = C_{sp} \, \rho^2 \left(Y_{F0} \frac{Z - Z_{st}}{1 - Z_{st}}\right) T^{2.25} \exp\left(-\frac{2000}{T}\right) \qquad (Z_{ox} < Z < Z_{cr}) \; (2\text{-}9)$$

$$Z_{ox} = Z_{C/O=0.6} \, ; Z_{cr} = 2.05 * Z_{st} \qquad (2\text{-}10)$$

The first parenthetical term is equivalent to local fuel mass fraction in a burning mixture ($Y_{F,B}$), assuming a one-step combustion reaction (this quantity includes all hydrocarbons). Like Lautenberger above [31], this rate was suppressed to zero except in a certain region of mixture fraction space defined between Z_{ox} and Z_{cr}. The onset boundary (Z_{cr}) was based on that of Lautenberger and is proportional to Z_{st} for a given flame and suffers from the same issues described above. The termination (Z_{ox}) boundary is calculated from values found in Kumfer [46] of critical local C/O ratio at the sooting limit. The integration of these values for the boundary is an important milestone for soot formation modeling in oxy-combustion, even though the Delichatsios group did not investigate this topic further. This model makes heavy use of the experimentally-determined smoke point of a fuel and even proposed developing a 'library' of smoke points could allow for easy fuel conversion for the model, as all the other parameters and trends are claimed to be fuel-independent. These papers varied on their approach to oxidation. Earlier papers did not consider oxidation [32] or used a constant rate [33], while later papers [34, 35] used the oxidation rate provided by Leung et al [47], whose model is discussed in the next section. This model was verified in laminar and turbulent non-premixed jets, as well as pool fires.

Tesner (T), et al. [48] developed a two-step formation model for an acetylene-hydrogen laminar coflow flame. The first equation is a population balance for soot precursors, n^*, between inception, branching, and termination reactions, as show in Eq. (2-11). The inception term is expanded into Eq. (2-12). The second population balance, Eq. (2-13), describes the net formation of mature soot particles, n,

$$\omega_{n^*} = n_0^* + (f-g)n^* - g_0 n n^* \tag{2-11}$$

$$n_0^* = 10^{13}[C_2H_2] \exp\left(-\frac{8.8*10^4}{T}\right) \tag{2-12}$$

$$\omega_n = (a - bn)n^* \tag{2-13}$$

Where n is a soot precursor, termed 'radical nuclei', f and g represent chain branching and termination ratios, g_0 is the termination coefficient for soot particles, N is a formed soot particle, a and b are fitted coefficients. where $f - g$ is 10^2, g_0 is 10^9, a is 10^5, and b is $8 * 10^8$ according to the author's fitting to the experimental data. The acetylene concentration is in terms of molecules per cubic centimeter. The precursors are formed from acetylene-based kinetics as well as chain branching; they are destroyed by collision with soot particles. This work gave an early consideration to the acetylene-based rate of formation. Soot particles form linearly with respect to precursors and are destroyed by collision with precursors. The various constants were obtained from fitting to experimental data taken from soot extraction measurements. Some of which change with experimental conditions, as seen in Table 2-3 below:

Burner Diameter	a	f-g	g_0	b	n_0	E_A
1 mm	10^5	100	10^{-9}	10^{-7}	$2*10^{13}$	180 kcal/mol
3mm	10^5	100	10^{-9}	10^{-6}	$1.5*10^{12}$	170 kcal/mol

Table 2-3: Values used for fitted parameters in the Tesner model.

The burner diameter and experimental set-up are described in [48]. As these conditions were determined for acetylene, it has been proposed that they would require modification before the model can be applied to other fuels [49].

Moss (M), et al. [50] produced a fuel-based two-step model for coflow (slot) flames that is still in use [51-53]. This model accounts for both particle mass and number and includes expressions for inception, surface growth, nucleation, and coagulation. The mass production rate (Eq. 2-14) is dependent on the fraction of unburned fuel, $X_{F,B}$. Moss emphasized the importance of high temperature and noted that significant soot formation only occurs in a very limited range of Z (Eq. 2-14), however, this constraint has been removed in this study so that it can be tested at higher Z_{st}. While temperature is the principal sensitivity in the mechanism, the use of the fuel mass fraction truncates the formation at the flame location (one step combustion chemistry is assumed). This termination is important, as the model did not originally have an oxidation mechanism; a later addition included this feature. This model was also of the firsts to use a surface area-dependent growth rate (Eq. 15), and it is assumed that the surface growth is directly proportional to the number of particles.

$$\omega_{inc} = 2.45 * 10^{10} \rho^2 \, T^{0.5} X_{F,B} \exp\left(-\frac{46,100}{T}\right) \quad (0.06 < Z < 0.20) \qquad (2\text{-}14)$$

$$\omega_{sg} = f(S) * 4.2 * 10^{-17} \rho X_{F,B} \exp\left(-\frac{12600}{T}\right) \qquad (2\text{-}15)$$

$$f(S) = n \qquad (2\text{-}16)$$

Kennedy et al. [54] developed a soot model whose formation rate was fitted to a Gaussian curve in mixture fraction space, as in their earlier work [55] (changes in nucleation rate with changing flame conditions were not accounted for [28]). Justification for this method is that most of the soot mass is produced through surface growth reactions [54] and that the distribution did not greatly affect results so long as the total number of particles was constant [55]:

"[m]easurements in many flames have shown that the number density of particles decays very quickly as a result of rapid coagulation near the particle inception zone. As a result, Kennedy et al. [28] ignored the equation for particle number density in favor of an average number density and hence they did not account for possible variations in nucleation rate with changing flame conditions." The particle formation region was determined by temperature boundaries of 1500-1600 K, leading to a peak at a mixture fraction of 0.22 and a standard deviation of 0.02 as seen in Eq. 2-17. The authors noted that the distribution did not great affect results so long as the total number of particles was constant. [55].

$$f(Z) = \frac{1}{\sqrt{2\pi(0.02)}} \, e^{-\frac{(Z-0.22)^2}{2(0.02)^2}} \tag{2-17}$$

Since this model 'does not account for possible variations in nucleation rate with changing flame conditions', it is not applicable to our focus. It may be further added that these conclusions were not tested for large Z_{st}.

Leung, Lindstedt, and Jones (LL) [47] proposed a model for counterflow flames which is similar to that of Moss et al. [50], but acetylene was selected as the dependent species for both inception (Eq. 2-18) and surface growth (Eq. 2-19) instead of the parent fuel. The authors also gave a review of activation temperatures and concluded that previous estimations were too high. A geometry-based formulation for the surface area was derived, shown in Eq. (2-20), before an empirically-based square root was added to capture aging effects on the particle.

$$\omega_{inc} = 10^4 \, [C_2H_2] \, \exp\left(-\frac{21100}{T}\right) \tag{2-18}$$

$$\omega_{sg} = f(S) * 6 * 10^3 \, [C_2H_2] \exp\left(-\frac{12100}{T}\right) \tag{2-19}$$

$$f(S) = (A_s)^{0.5} = \left(\pi d_p^2 * \rho n\right)^{0.5} = \left(\pi \left(\frac{6}{\pi}\frac{1}{\rho_S}\frac{Y_S}{n}\right)^{\frac{2}{3}} \rho n\right)^{0.5} \tag{2-20}$$

Lindstedt later modified this model [56], promoting a benzene-based inception step to include with the existing C_2H_2-based inception step (Eq. 2-21) and investigated alternative surface area formulations. Four different relationships (La, Lb, Lc, Ld) were used: 1) particle surface area that included a term to account for surface aging through HACA (χ) (Eq. 2-23), or 2) particle surface area which did not include χ (Eq. 2-24), 3) particle number (Eq. 2-25), 4) a constant value (Eq. 2-26). According to Lindstedt, the particle number formulation (Eq. 2-25) yielded the best fit to experimental data for the C_2H_4 counter flow flames in the study. All four formulas are evaluated in this study.

$$\omega_{inc} = 6.3 * 10^3 [C_2H_2] \exp\left(-\frac{21000}{T}\right) + 7 * 10^3 [C_6H_6] \exp\left(-\frac{21000}{T}\right) \tag{2-21}$$

$$\omega_{sg} = f(S) * 6 * 10^3 \, [C_2H_2] \exp\left(-\frac{12100}{T}\right) \tag{2-22}$$

$$f(S) = \chi * A_s = \chi * \left(\pi \left(\frac{6}{\pi}\frac{1}{\rho_S}\frac{Y_S}{n}\right)^{\frac{2}{3}} \rho n\right)^{1} \tag{2-23}$$

$$f(S) = A_s = \left(\pi \left(\frac{6}{\pi}\frac{1}{\rho_S}\frac{Y_S}{n}\right)^{\frac{2}{3}} \rho n\right)^{1} \tag{2-24}$$

$$f(S) = n \tag{2-25}$$

$$f(S) = constant \tag{2-26}$$

Brookes and Moss (MB) [29] also developed an acetylene-based soot model for non-premixed, methane, turbulent-jet flames. The framework is similar to the Leung-Lindstedt model above, but some parameters were changed so that predicted soot volume fraction would match experimental data.

$$\omega_{inc} = 7.78 * 10^3 [C_2H_2] \exp\left(-\frac{21100}{T}\right) \tag{2-27}$$

$$\omega_{sg} = f(S) * 30.7 * [C_2H_2]^{0.4} \exp\left(-\frac{12100}{T}\right) \tag{2-28}$$

$$S = A_s = \pi d_p^2 * \rho n = \left(\pi \left(\frac{6}{\pi} \frac{1}{\rho_S} \frac{Y_S}{n}\right)^{\frac{2}{3}} \rho n\right)^1 \tag{2-29}$$

The activation energy was taken from Leung above [47], making the two inception models nearly identical with the exception of the leading constant (the models differ for other terms).

This model was fitted for methane and was therefore limited to light gaseous fuels, before being extended by Hall (MBH) et al. [30], and reported by Wen et al. [57], for the combustion of heavier fuels such as kerosene. This extension includes an inception rate based on the formation rates of 2 and 3-ringed aromatics aromatic species, and is shown in Eq. (2-30), with retaining the other terms of the Moss-Brookes model.

$$\omega_{inc} = 8 * 127 * 10^{8.88} \left[\left(\frac{Y_{C_2H_2}}{MW_{C_2H_2}}\right)^2 \frac{Y_{C_6H_5}W_{H_2}}{W_{C_6H_5}Y_{H_2}}\right] \exp\left(-\frac{4378}{T}\right)$$

$$+ 8 * 178 * 10^{9.5} \left[\frac{Y_{C_2H_2}}{W_{C_2H_2}} \frac{Y_{C_6H_6}W_{H_2}}{W_{C_6H_6}Y_{H_2}} \frac{Y_{C_6H_5}W_{H_2}}{W_{C_6H_5}Y_{H_2}}\right] \exp\left(-\frac{6390}{T}\right) \tag{2-30}$$

Except where indicated above, these models were chosen for evaluation in high Z_{st} flames for a variety of reasons. ANSYS Fluent includes the KG, T, MB, MBH, models for commercial use

[17]. In recent years, the LL model remains one of the more widely used models in CFD simulations by researchers [58-63]. Less-popular models used in this study provide a contrast in the level of complexity. One example is this variance is the species chosen for as a chemical precursor. KG and M are fuel-based; their inclusion considers whether fuel alone is a sufficient precursor. LL and MB are C_2H_2-based, while La-Ld and MBH add an A1-based inception to LL and MB, respectively. Another model description showing significant variance is the surface area function. The models LL use the same equation for SG as MB, and MBH, but with different fitting constants for the C_2H_2 and SA dependencies. La-Ld use novel expressions for the SA term. T was added, despite its age, because of its unique two-step formulation. D was added due to its description of boundaries of the soot formation zone based on Z or local C/O ratio. Thus, all models included in this evaluation were either pre-existing in commercial software or offer conceptual alternatives that could either potentially capture the changes in soot formation at these conditions or else offer insights into which modeling features are necessary. Table 2-4 below shows all models, outlining their distinctive features in a concise fashion.

One-Step Models	Equation
Khan-Greeves [1]	$\omega = kP_F\phi^3$
Delichatsios et al. [2]	$\omega = kY_F$ $Z > Z_{crit}; Z < mZ_{st}$

Two-Step Models	General Equation	Inc. Species	Surface Area	SG Species
Tesner [3]	$\omega_{n^*} = n_0^* + k_o n^* - k_1 nn^*$ $\omega_n = (k_2 - k_3 n)n^*$	$[C_2H_2]$	$S = n^*$	-
Moss et al. [4]	$\omega_s = \omega_{inc} + \omega_{sg}$ $\omega_n = \dfrac{N_{Av}}{MW_C N_{C,inc}}\omega_{inc} - \beta n^2$ $\omega_{inc} = k_0 * [C_mH_n]$ $\omega_{sg} = k_1 * S(Y_s,n) * [C_mH_n]$	$[Y_F]$	$S = n$	$[Y_F]$
Leung-Lindstedt [5]		$[C_2H_2]$	$S = \left(\pi d_p^2 n\right)^{0.5}$	$[C_2H_2]$
Lindstedt A [6]		$[C_2H_2],[C_6H_6]$	$S = \chi\pi d_p^2 n$	$[C_2H_2]$
Lindstedt B [6]			$S = \pi d_p^2 n$	
Lindstedt C [6]			$S = n$	
Lindstedt D [6]			$S = k$	
Moss-Brookes [7]		$[C_2H_2]$	$S = \pi d_p^2 n$	$[C_2H_2]$
Moss-Brookes-Hall [8]		$[C_2H_2],[C_6H_6]$		

Table 2-4: Overview of semi-empirical soot formation models.

A few authors have previously compared some of these models. Nmira et al. [64] compared the models of Lindstedt et al [56], Lautenberger et al [31], and Yao et al [34] (referred to in this work as one of Delichatsios' models) with the following conclusions: the application of the smoke-point concept is questionable for weakly-sooting fuels, using the smoke-point concept leads to the over-prediction of soot, all the models reproduced the smoking behavior of very strongly smoking flames, that Lautenberger provides a better agreements than Yao for inverse diffusion flames, and that Lindstedt and Lautenberger computed radiation fractions within 10% of experimental data, while Yao had less accurate agreement. However, no author has comprehensively compared all of these models together for any flame conditions and none of these models, to this author's knowledge, have been evaluated against elevated- Z_{st} flames. The methods used to evaluate these models are described in chapter four. But first, a brief overview of detailed soot modeling is given.

2.4　Detailed Models

While the focus of soot modeling in this dissertation centers on semi-empirical models, detailed soot models play a minor role and will be briefly discussed here. These models use kinetic expressions to calculate the rates for the processes mentioned above (inception, various growth pathways, oxidation). The different expressions used by modelers are discussed below, individually. These models are also compliant with particle tracking methods such as the method of moments and the sectional method. The use of these methods is required to obtain information about the PSD. Most models include kinetic reactions. As these models often have computational costs too high to be considered in applications of our interest, this section will be brief in its summary of various models.

Chernov et al [13] modeled soot in a laminar co-flow non-premixed system using a discrete sectional method. This type of soot modeling divides the particle size distribution into 35 discrete sections based on the mass. The mass of each section is left unchanged and a geometric series is assumed to represent the mass of each section. This assumption is used because of computational constraints. The soot in each section is composed of fractal-like aggregates (Df = 1.8). All aggregates are assumed to be identical within a section and their respective sections are determined by their mass. In each section a transport equation for the number density is solved. The nucleation step connects the gaseous incipient species to the solid phase and places these particles in the first section. PAH dimerization is taken to be the nucleation step. Lower section particles move to higher sections by surface growth (HACA + PAH condensation) or coagulation. Particles move from higher to lower sections by oxidation or fragmentation.

Chen et al [14] used a population balance solver by coupling the PAH-PP model [11] with the KMC-AS model [25]. This model simulates soot aggregates that are comprised of primary particles which are comprised of individual PAH molecules. The coupling with the KMC-AS model allows for detailed modeling of active sites on the surfaces of the PAH molecules. Processes considered are: inception (PAH dimerization), surface reactions of growth and oxidation consider 18 different processes on these active sites. Coagulation and condensation are included and are directly imported from the PAH-PP model. Sintering is also included, while fragmentation is not.

Bisetti et al [65] modeled soot in a turbulent non-premixed flame. To save computational expense, a method of moments was employed. Nucleation is described as the collision of two dimers, each dimer being formed as the self-collision of naphthalene. Growth can occur by dimer condensation on a pre-existing particle and by HACA. Coagulation is considered and oxidation is a semi-empirical rate of concentrations of OH and O_2.

The model of Appel, Bockhorn, and Frencklach (ABF) [16] will be analyzed in Section 6. For the ABF mode, there is one equation for the inception: A_4 dimerization, which creates a nascent soot particle comprised of C atoms, H atoms, open sites, and closed sites (Eq. 2-31). Then Eq. 2-32 flips closed sites to become open via H-abstraction. Open sites are then available for C_2H_2-based surface growth (Eq. 2-33) and aromatic condensation (Eq. 2-34) may even occur on closed sites.

$$2A_4 \rightarrow C(s) + open(se) + H(se) \qquad (2\text{-}31)$$

$$H(se) + H \rightarrow open(se) \qquad (2\text{-}32)$$

$$Open(se) + C_2H_2 = C(s) \qquad (2\text{-}33)$$

$$H(se) + A_i = C(s) \qquad (2\text{-}34)$$
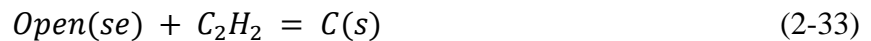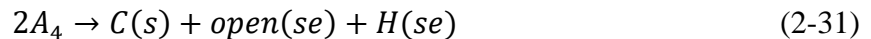
Wang et al. [10] developed a gas and soot mechanism, "KM2" to calculate soot in a counterflow diffusion flame. Inception was modelled as the dimerization of 8 different PAHs (A_4 – A_7) leading to a combination of 36 different reactions, which create C atoms, H atoms, and closed sites (but no open sites, see Eq. 2-35). Surface growth is similar to HACA above, but expanded (H abstraction can occur from any of H, OH, CH_3, C_3H_3, C_2H). PAH condensation is considered. Coagulation was modeled, while agglomeration and fragmentation were not. Particle tracked used a method of moments.

$$2A_i \rightarrow C(s) + H(se) \tag{2-35}$$

Unlike semi-empirical models, detailed models have the ability to resolve the particle size distribution. This is done through either the method of moments or by the section method. For the former method, a series of moments is calculated by:

$$M_{xy} = \sum_i V_i^x S_i^y N_i \tag{2-31}$$

Where M is the moment of order x with respect to volume (V) and of order y with respect to surface area (S), and N is number density. The resulting moments are used to calculate physical dimensions such as the primary particle diameter, the number of particles per aggregate. The sectional method tracks the size by accounting for the number of particles in a certain bin-sized. As particles grow / shrink through various reactions, they move to bins of larger / smaller particle size after crossing a certain size threshold. Inception creates particles in the smallest bin and when being attacked by oxidation, particles in the smallest bin are eliminated accordingly.

Chapter 3: Review of Stoichiometric Mixture Fraction (Z_{st}) and Soot Formation

3.1 Introduction to Z_{st} and Its Effect on Soot Formation

Mixture fraction (Z) is a conserved scalar and is thus a quantity which is invariant to chemical reaction. It is defined as the fraction of mass that originated from the fuel inlet for any particular location in the combustion system and thus expresses the mixing progress for non-premixed flames. The mixture fraction at the location at stoichiometry, i.e. the stoichiometric mixture fraction (Z_{st}, Eq. 3-1) marks the flame location in a nonpremixed flame.

$$Z_{st} = \left(1 + \frac{Y_{F,0} W_O v_0}{Y_{O,0} W_F v_F}\right)^{-1} \tag{3-1}$$

Modification to a fuel-air flame by either fuel dilution and/or oxygen-enrichment increases Z_{st} and alters the flame structure of a nonpremixed flame [19, 66]. Consequently, soot formation is significantly affected by changes in Z_{st}. An example of this behavior can be seen in Fig. 301 for a series of coflame images taken from the literature. The presence of soot can be visibly seen in three of the four flames. Moving from left to right, Z_{st} increases (see values in Fig. 301) as inert is shifted from the oxidizer to the fuel, while maintaining a constant flame temperature. Accordingly, soot formation is steadily diminished until a blue flame is achieved for the further right image at $Z_{st} = 0.4$. The underlying causes for this reduction and eventual suppression of soot formation under these flames conditions has been the study of several authors reviewed below.

27
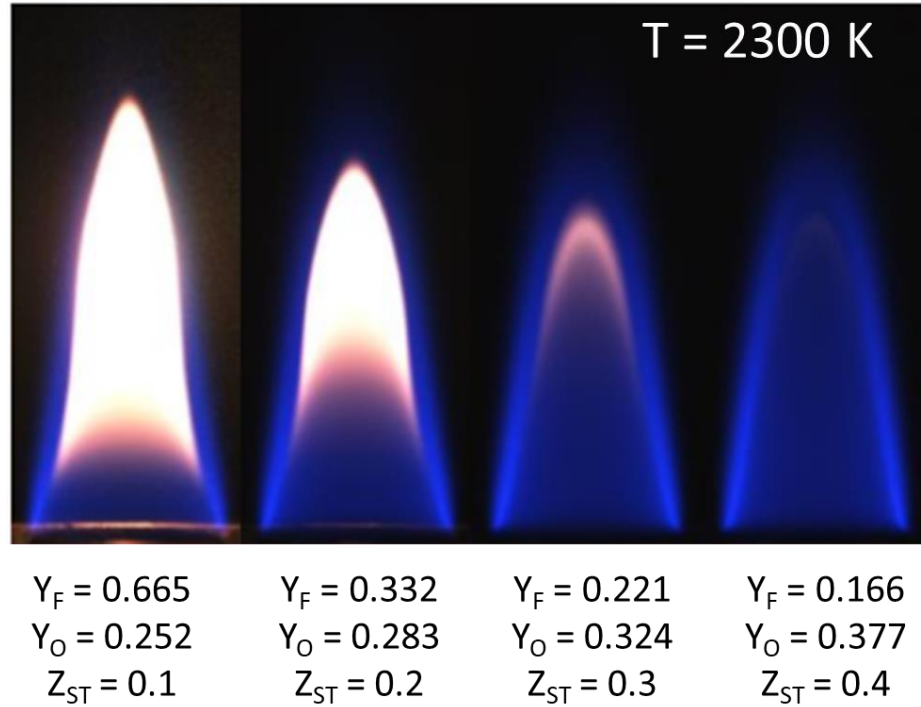
Figure 3-1. A series of coflow flames of increasing Zst for the same adiabatic flame temperature taken from [4]. Soot zone is indicated by white light.

3.2 Proposed causes of soot suppression

Early investigations into changes in flame structure resulting from increased Z_{st} showed that the soot formation zone can be described by two boundaries in mixture fraction space [3, 46, 67], which are shown in Fig 3-2a. The first boundary, where soot formation begins, termed the 'onset' boundary (labeled C1 in Fig. 3-2a.), is characterized by the location where requirements of sufficient fuel, temperature, and available reaction time are satisfied. The location of this boundary is related to the gas pyrolysis and particle inception processes. The second boundary, where soot formation ceases, termed the 'termination' boundary (labeled B1 in Fig. 3-2a), is characterized by a critical local C/O ratio that was shown to be equivalent, for a given fuel to the critical, global C/O ratio necessary for soot formation in premixed flames [46]. With increasing fuel dilution and/or oxygen enrichment, these two boundaries approach each other, leading to a smaller soot

28

formation zone as seen in Fig. 3-2b. With further increase these two boundaries will converge and

no soot will be formed, resulting in a non-sooting, blue flame (Fig. 3-2c).
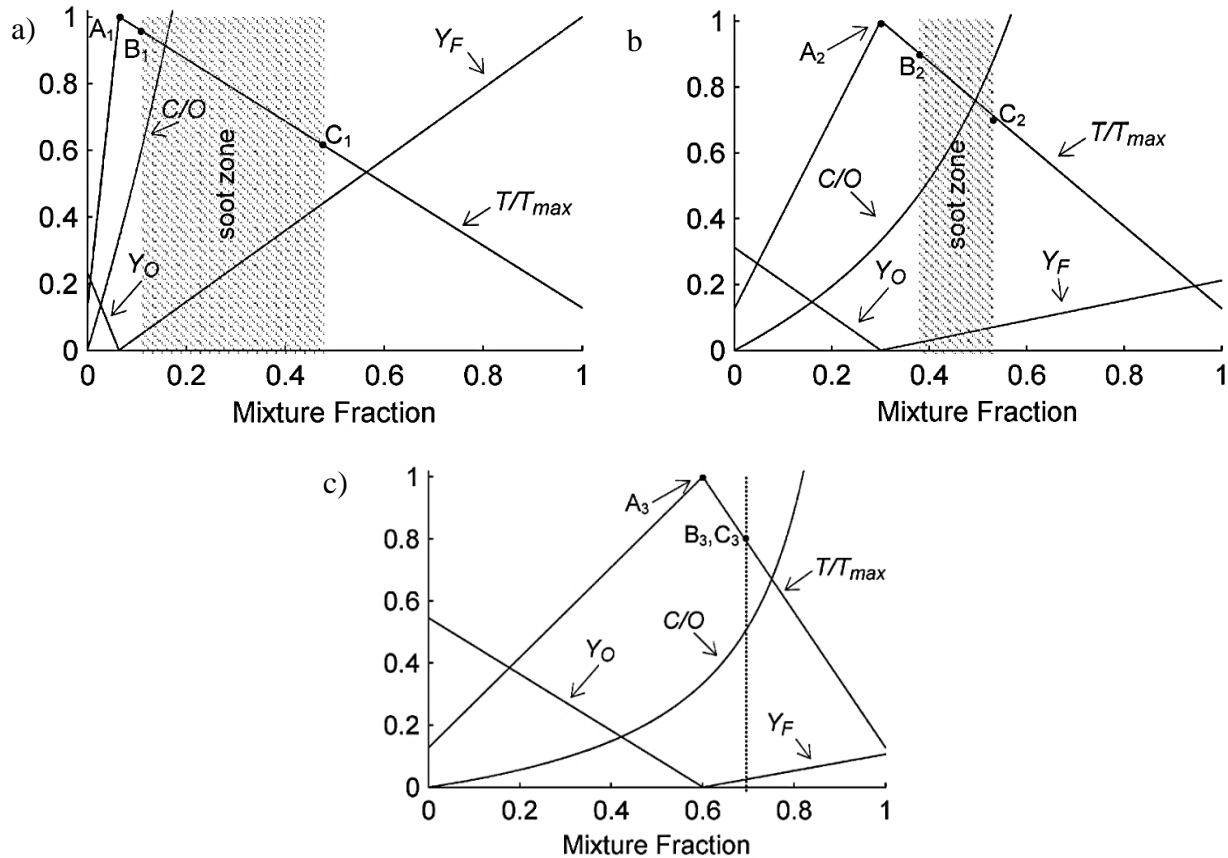
Figure 3-2: Flame structure and soot formation zone changes for increased Z_{st} in mixture fraction space for: a) $Z_{st} = 0.064$, b) $Z_{st} = 0.30$, c) $Z_{st} = 0.60$. Figures taken from Kumfer et al. [46]

The work of Kumfer et al. [46] examined the soot inception limits in nonpremixed coflow

flames for a variety of fuels. A high-temperature boundary of the soot-formation zone was

observed which was on the fuel side of the flame front. Those locations were characterized by a

critical local equivalence C/O ratio [46] for several different aliphatic fuels and are shown in Table

3-1. For example, C/O)$_{cr}$ for ethylene was determined to be 0.53 [46], which is relatively far from

the location of stoichiometry (C/O = 0.33).

Fuel	Measured critical C/O [54]	Stoichiometric C/O
CH_4	0.42	0.25
C_2H_6	0.54	0.29
C_3H_8	0.58	0.30
C_2H_4	0.60	0.33
C_2H_2	0.71	0.40

Table 3-1. Critical C/O values below which no soot can form as measured by Kumfer et al. [46], followed by the C/O of stoichiometry for each fuel.

3.3 Soot Precursor Chemistry and Z_{st}

Significant work has been done on the role of soot precursor chemistry, whether precursor consumption [68] or the reversal of pathways leading to aromatic ring formation [9, 69]. Skeen, et al. [19] examined the effect of Z_{st} on chemical reaction pathways critical to soot inception by modeling a series of counterflow flames with the USC-II mechanism. Propargyl self-combination was seen as the dominant pathway for aromatic ring formation and the authors concluded that this formation reaction reverses at high Z_{st} due to an increase in H^+ radicals. Skeen et al. analyzed several potential pathways to aromatic formation, two of which are shown in Eqs. 3-2 – 3-3. They argued that Eq. 3-2 should be given precedence over Eq. 3-3 because its integrated contribution was seven times larger and that Eq. 3-2 was affected by Z_{st}-based flame structure effects while Eq. 3-3 was pyrolysis-based and controlled by dilution. They also noted that Eq. 3-2 is endothermic, being predominant at higher temperatures (>1600 K) before reaching the H^+ pool while Eq. 3-3 is exothermic and favored and lower temperatures (<1600 K)
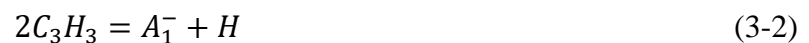
$$2C_3H_3 = A_1^- + H \tag{3-2}$$

$$C_4H_5 2 + C_2H_2 = A_1 + H \tag{3-3}$$

Skeen et al. also hypothesized that these behaviors would be observed for other soot-precursor-growth reactions where H^+ is generated as a product, e.g. there would be a reduction in PAH growth due to this set of reactions. This claim is further investigated in Section 6.

3.4   The Challenge of Z_{st} for Soot Modeling

High Z_{st} environments alter flames structures and soot formation in ways that challenge the description of soot as pyrolysis-driven process for traditional fuel-air flames. Reversibility of chemical pathways which otherwise promote soot formation can play a critical role in these environments. Thus, capturing these effects can be important for accurately modeling soot fraction in these environments. The following chapters will describe a methodology to evaluate existing soot models based upon this premise and then offer alternative modeling methods.

Chapter 4: Methodology

4.1 Counterflow Flames

4.1.1 Background

The laminar counterflow flame is chosen for this study due to the availability of experimental datasets in the literature as well as the applicability of the results to laminar "flamelets" which are present within larger turbulent structures. This flame setup is composed of two opposed flow jets, one for fuel and the other for oxidizer in the case of nonpremixed (NPM) flames, as used in this research. These two streams meet at the gas stagnation plane (*gsp*) where the axial velocity of the gas is zero. For the sake of maintaining continuity of momentum, a radial component of the velocity develops by which the gas and other products leave the system. Thus, the streamlines are similar to that indicated in the diagram shown in Fig. 4-1.
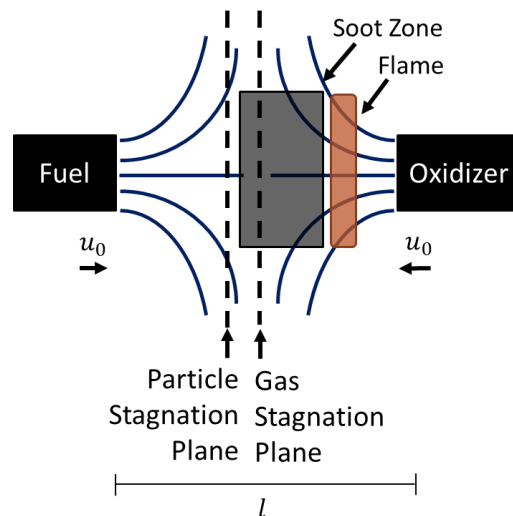
Figure 4-1. Diagram indicating basic features of a soot-forming (low Z_{st}) counterflow flame. Gas streamlines are indicated by solid blue lines. Drawing not to scale.

The flame location in a counterflow flame will vary as the inlet compositions are modified. In a NPM system, the flame is always located at the location of stoichiometry (Z_{st} or $\Phi = 0.5$). However, the location of stoichiometry is affected by a modified Z_{st}. At low Z_{st}, such as in a fuel-air flame, the flame is located on the oxidizer side of the *gsp*, as depicted in Fig. 4-1. As Z_{st} is increased, the flame shifts in physical space towards the fuel inlet. At $Z_{st} = 0.5$, the flame will be located in the *gsp* when the jet velocities and boundary conditions are the same due to the system of the flow system.

Finally, under appropriate flame conditions soot will occur on the fuel side of the flame. When the flame is on the oxidizer side of the *gsp*, soot follows the streamlines and is convected away from the flame towards the *gsp*. Due to the effect of thermophoresis on the particles, soot travels beyond the *gsp* before it reaches the *psp* where the average particle axial velocity is zero and the particles are ejected from the system due to the radial component of their velocity obtain via drag. Mature soot particles are considered large enough for Brownian motion to be neglected.

Absent from this description of soot formation and transport is oxidation. Recall that immediately after the inception process occurs that the nascent particles are transported away from not only the oxidizer region, but also the flame region. Thus, soot particles face no chemical attack in these flames once they are formed. For this reason, these types of flames have been referred to as soot-forming (SF). The soot fraction profile has a distinctive shape under this flame configuration, where the quantity steadily increases from the flame until the *psp*, where there is a total loss of soot particles as they are ejected from the system. The profiles of temperature, soot formation, C_2H_2 (an important growth species), and soot volume fraction are shown in Fig. 4-2, which is a visual aid corresponding to Fig. 4-1. In contrast to SF flames, when the flame is on the

fuel side of the *gsp*, soot will be convected towards the oxidation region and consumed. These flames are characterized as soot-forming-oxidizing (SFO) flames.
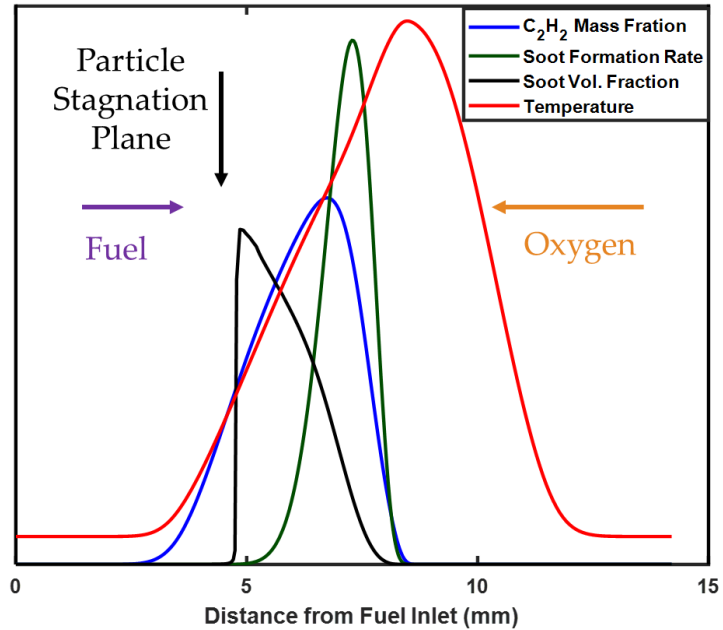
Figure 4-2. Profiles temperature, C_2H_2 mass fraction, soot formation rate, and soot volume fraction in a soot-forming counterflow flame. Quantities were obtained by solving the KM2 mechanism [10].

4.1.2 Soot inception limits

Soot formation can be greatly affected in the counterflow flame and even eliminated such that a blue flame is produced, by increasing either Z_{st} or K. This phenomenon is demonstrated by the soot inception limits measured by Du and Axelbaum [5] and Wang et al. [8] shown in Fig. 4-3. The soot inception limit data corresponds to the flame conditions at which the transition from yellow to blue occurs. The region to the left of the limit line corresponds to flame conditions for which visible emissions from soot particles could be observed; to the right of the limit the soot concentration is below the detection limits and appears blue.

34
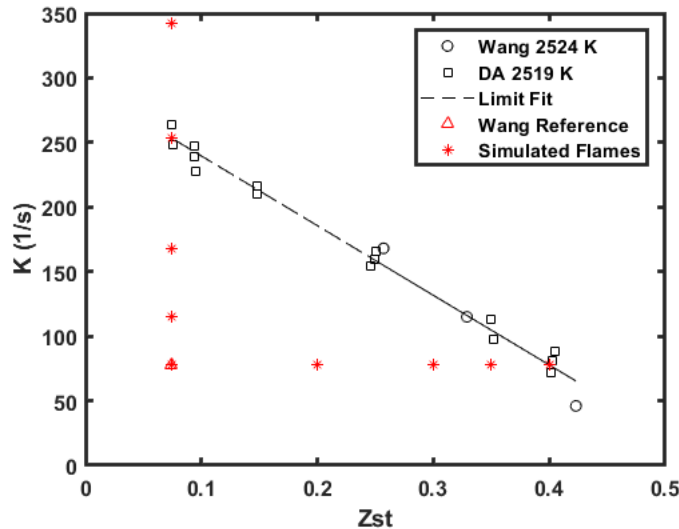
Figure 4-3. Simulated flame conditions (red) and experimentally reported sooting limits (Wang et al. [5] in black circles, Du, Axelbaum (DA) [8] in black squares) in terms of K (velocity gradient upstream of the flame on the oxidizer side [70]) and Z_{st}. Soot forms for flames to the left of the limit ("yellow") and does not form for flames to the right of the limit ("blue").

Wang et al. reported soot inception limits in terms of gas concentrations and jet velocities (measurements reproduced in Fig. 4-4) while Axelbaum et al. reported the limits in terms of Z_{st} and K (as with Fig. 4-3 above). The latter values are used for this study and it was thus necessary to convert the former data into terms of the latter. The factor of temperature also must be considered as the mapping from Wang et al. allows temperature to vary. Fig. 4-4 shows lines of constant adiabatic flame temperature imposed on the inception limit data of Wang. At the location where a constant temperature curve (red) crosses a constant velocity limit curve (blue), that location has a uniquely determined velocity, temperature, and Z_{st}.
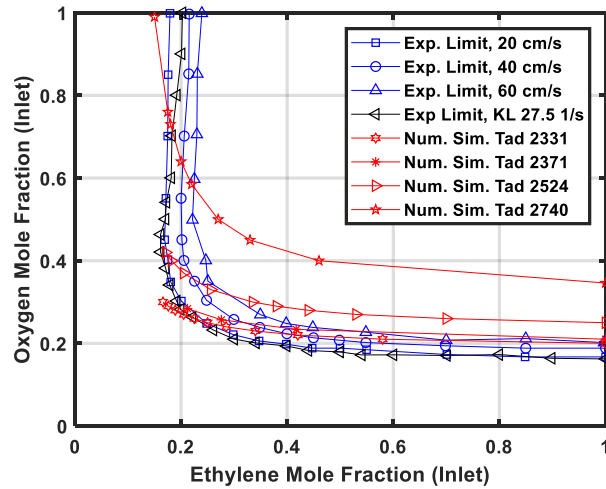
Figure 4-4. Map of soot inception limits measured by Wang et al. [8] (blue) in terms of O_2 and C_2H_4 mole fractions for a given jet velocity, with constant flame temperature curves imposed (red).

The burners used in both studies had a separation distance of 8 mm and attempted plug flow conditions. Wang et al. reported velocity conditions which were used to obtain, via modeling, the velocity gradient upstream of the flame (oxidizer side) at the soot inception limit for the given Z_{st} and T_{AD}. To do so, simulations were performed with the gas composition and inlet jet velocities as indicated in the work of Wang et al. Then a series of lines were impose on the plot in an attempt to find the radial gradient on either the oxidizer (Fig. 4-5a) or fuel (Fig. 4-5b) side by matching the tangent of the velocity prior to the flame. As can be seen from the U60 case, several different boundary conditions were used for the radial gradient to confirm that there was not a strong deviation in the upstream gradient prior to the flame. This information allowed a direct comparison between the two strain variables when comparing the inception limits of Wang et al. (jet velocity) vs. Axelbaum et al. (velocity gradient).

36

(a) Wang, Velocity Gradients F Side

(b) Wang, Velocity Gradients O Side
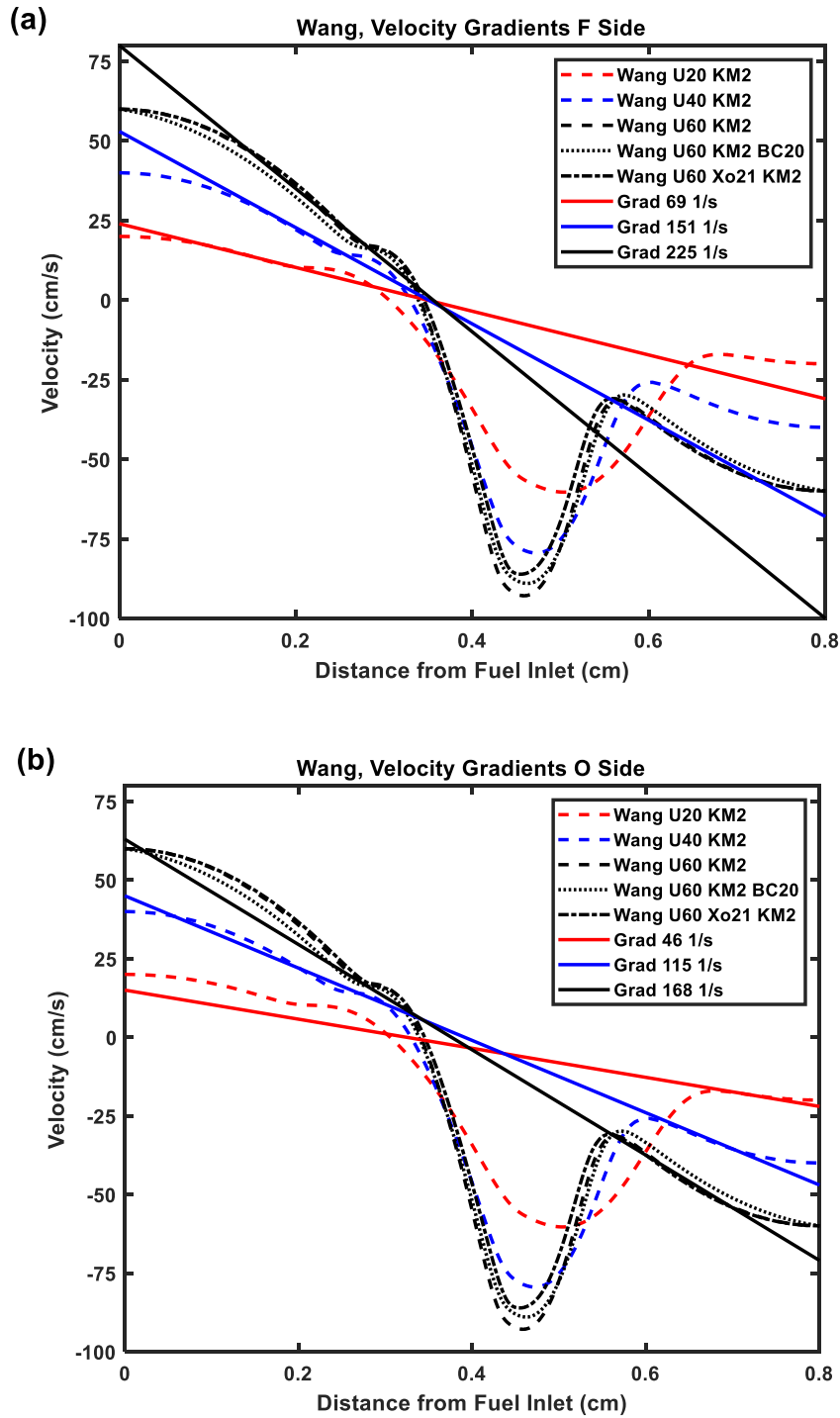
Figure 4-5. Velocity (cm/s) vs. physical space (cm) for simulations of counterflow flames with varying jet velocities with linear velocity gradients imposed to observe the gradient upstream of the flame on a) the fuel side, b) the oxidizer side, of the flame.

With the same metric for both measurements, that inception limit point can then be plotted in terms of Z_{st} and K for a given temperature. The limit data from these two studies can now be plotted together as shown in Fig. 4-6. There is good agreement observed for the intermediate flame temperature (2519 K), which was used for Fig. 4-3 above. The reason for the disagreement for other flame temperatures for this is unclear. Once X_f, X_o, and T are specified, then Z_{st} is uniquely determined. There could be potential error in converting from jet velocity to velocity gradient. It could be speculated that the exercies done in Fig. 4-5 is specific to a flame temperature; however, the purpose of choosing the velocity gradient upstream of the flame is to avoid any flame-induced velocity perturbations in defining strain rate. This question currently remains unresolved, but there is sufficient agreement at 2519 K for the model evaluations done in this research.
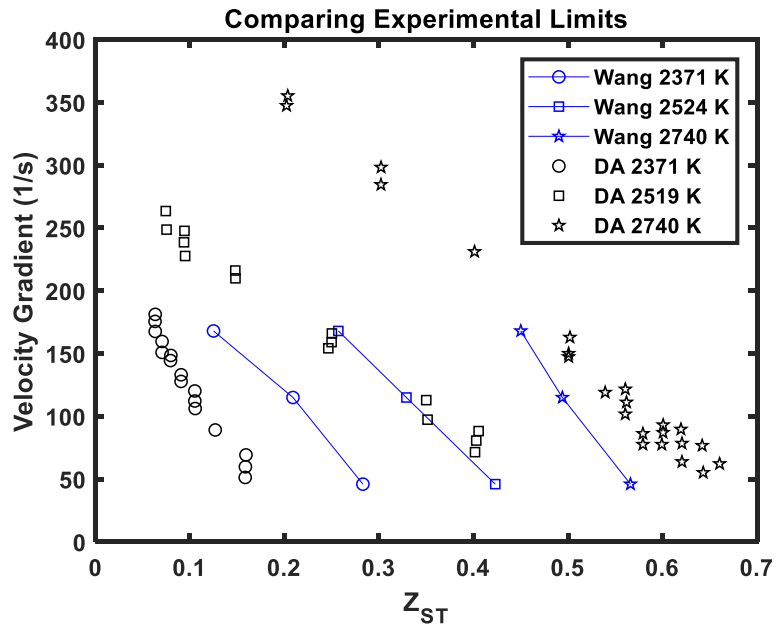
Figure 4-6. Full measurements of the soot inception limit in a counterflow flame by Du, Axelbaum for various flame temperatures (black) with inception limits from Wang, et al. (blue) as calculated by the method described above.

4.1.3 Simulated flame conditions

In order for a soot model to be useful in situations beyond the standard fuel-air flame, it should not predict substantial quantities of soot in flames that are intrinsically soot-free. The semi-emperical soot models under consideration are therefore challenged by utilizing them in simulated flames which span a broad range of Z_{st} and K that includes the yellow to blue transition. While the corresponding investigations into the flame conditions at the limit [5] did not report the minimum *svf* necessary to register a yellow flame, a previous study [44] which provided the diagnostic basis for the limit study [5] did report measured *svf* values in soot-producing flames down to 10^{-8}. For this study, any model which predicts *svf* greater than this value of 10^{-8} for flame conditions which are experimentally known to be blue is considered to be giving an inaccurate result.

The flames simulated in this study are shown above in Fig. 4-3 and the flame conditions are listed in Table 4-1. These conditions are designed to observe each models' prediction of soot formation in response to either increased Z_{st} or increased K. In one set of conditions K is held constant while Z_{st} is increased (Series 1 in Table 4-1); for the other, Z_{st} is held constant while K is increased (Series 2 in Table 4-1). Adiabatic flame temperature was held constant for all these conditions (2519 K).

Flame Name	$Y_{F,0}$	$Y_{O2,0}$	*Zst*	*K (1/sec)*
0	1.0	0.276	0.074	78
1.1	0.380	0.318	0.196	78
1.2	0.256	0.360	0.291	78
1.3	0.215	0.391	0.347	78
1.4	0.190	0.422	0.393	78
2.1	1.0	0.25	0.074	115
2.2	1.0	0.25	0.074	168
2.3	1.0	0.25	0.074	263
2.4	1.0	0.25	0.074	315

Table 4-1. Flame conditions for simulations. The adiabatic flame temperature was held constant at 2519 K.

4.2 Modeling Soot in Counterflow Flames

4.2.1 Chemkin Flame Simulations

Simulations of counterflow flames are performed using the CHEMKIN Pro [71] Opposed Flow module. The KM2 detailed combustion mechanism [10] is used to obtain the velocity, temperature and gas-phase species distributions. It should be noted that this mechanism has not been experimentally validated for the full set of flame conditions considered here (higher-Z_{st}). Additional simulations using the ABF model [16] were performed to confirm that the results of semi-empirical model evaluations were not significantly affected by the choice of detailed gas mechanism; these results can be found in Figs. 4-9, 4-10 in Section 4.3 (Supplemental Material). The CHEMKIN output data is post-processed in a MATLAB subroutine to solve the soot conservation equation(s) and calculate soot volume fraction. While the MATLAB routine is not fully coupled to CHEMKIN, the flame simulations included the detailed KM2 soot mechanism as proxy to account for the effects of precursor consumption and soot radiation. Further, the soot fraction is relatively small (< 1 ppm) in these flames studied here, so these effects are negligible.

4.2.2 Matlab Post-Process Soot Code

Following modeling techniques used for droplets in studies of spray combustion in the counterflow configuration [72-74], both axial and radial convection are mathematically considered in the soot conservation equations, since one-dimensional transport leads to a mathematical singularity at the particle stagnation plane [72, 75]. Given that the inertial force associated with soot particles is very small compared to the drag force (Stk << 1) the similarity solution for gas species in a stagnation flow can also be utilized for particle transport [76]. Thermophoresis in the

41

axial direction is also considered [77]. This particle conservation equation is discretized into an Eulerian, time-dependent, upwind finite differencing equation, shown in Eq. (4-1),

$$\zeta_i^{n+1} = \zeta_i^n + \frac{\Delta t}{\rho_i}\left(\omega_i - \frac{\Delta\rho(u+v_{th})\zeta}{\Delta x} + \rho\zeta G|_i\right) \tag{4-1}$$

$$G = \frac{\rho v}{r} \tag{4-2}$$

where G is the similarity parameter defined in Eq. (4-2). Eq. (4-1) is iteratively solved until convergence is achieved. The criteria for convergence is when the relative change in peak soot volume fraction (*svf*) is less than 10^{-5} [77, 78].

The models are evaluated in counterflow flames of sufficiently low Z_{st} such that all formed soot is convected towards the fuel source, away from the stoichiometric flame location. Oxidation reactions are, therefore, expected to be negligible [2, 56, 79]. However, surface oxidation reactions for most two-step models (M, LL, La-Ld, MB, MBH) have also been included using the original model formulations (see respective references [29, 30, 47, 50, 56, 80]). Oxidation is found to only have a minor impact on the peak *svf* for some models. See Fig. 4-11 in Section 4.3 (Supplemental Material) and subsequent discussion for more information.

For validation of the modeling approach and particle subroutine, numerical results from the Leung and Lindstedt model [47] in an ethylene counterflow flame are compared with the experimental results of Hwang et al. [2] and with corresponding modeling results of Hernandez et al. [77], who also utilized the Leung and Lindstedt model for the same flame set, as shown in Fig. 4-7. The data set includes measurements of soot volume fraction in three flames with variable oxygen fractions in the oxidizer stream (20%, 24%, and 28%). The results of our simulation are in good agreement with the modeling results of Hernandez et al et al. [74].
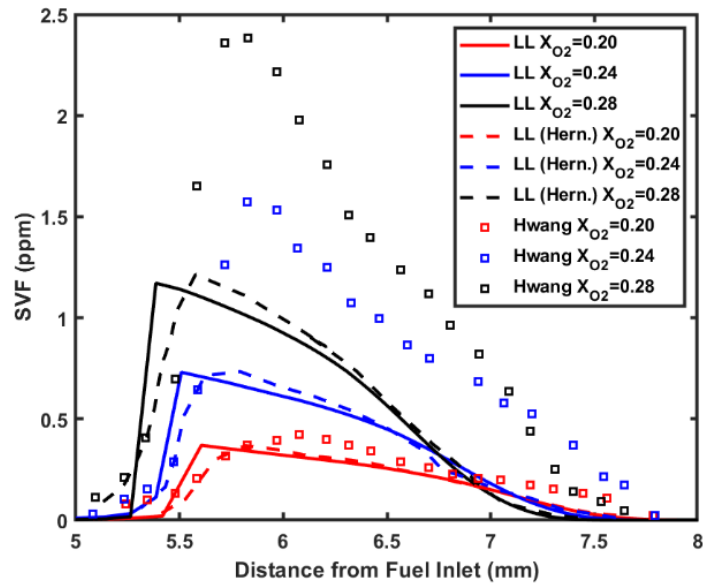
Figure 4-7. Soot volume fraction (*svf*) profiles resulting from the use of the Leung and Lindstedt (LL) model in this work and comparisons to reference numerical (Hernandez et al. [77]) and experimental (Hwang et al. [2]) data.

4.2.3 Normalization Process

Many of the semi-empirical soot models used in this study were not developed specifically for use in counterflow flames and were not validated for this flame type. Therefore, prior to the evaluation, all formation rate equations are adjusted such that the resulting peak *svf* is matched with an experimental measurement [10, 81] for the low Z_{st}, low K flame ("Wang Reference" in Fig. 4-1, Flame 0 in Table 4-1) to achieve a more reasonable comparison between models and to ensure a fair evaluation. To accomplish this end, the soot formation rates were scaled by multiplying the inception and surface growth terms in Eqs. 2-1, 2-2 by a normlization factor. By normalizing both inception and surface growth, soot formation rates are adjusted without creating bias against any model's developed balance between these terms. The relevance of inception and surface growth to total soot formation are discussed in the results section. Normalization results are shown in Fig. 4-8 and normalization factors are listed in Table 4-2. All modified models are shown to produce a *svf* profile that is in reasonable agreement with the experimental data, though

43

some models predict levels of soot higher than experimental data in the region of 0.5-1.5 mm. Comparatively, when there is no normalization, values for *svf* ranged over several orders of magnitude (see Fig. 4-8b). Aside from the standard normalization, the Tesner model required further augmentation to achieve a matching peak *svf* after it was found that elevating *k* higher than 18 resulted in unstable behavior of the soot formation equations. The growth term of mature particles (term "*a*" in Eq. 2-13) was further multiplied by 2E4.
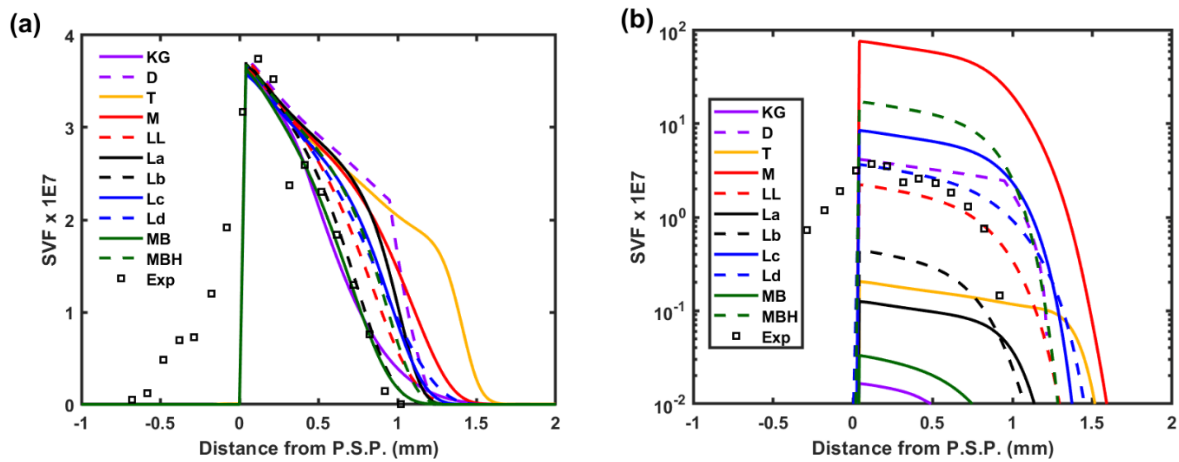
Figure 4-8. The effect of normalization for a *svf* profile a) normalized semi-empirical models with experimental data (linear scale) b) unnormalized semi-empirical models with experimental data (log scale). Fig 4-10a is equivalent to Fig. 3 in the main article and has been reproduced here for ease of comparison. Note that the flame conditions are the same between figures.

Model	Abbreviation	Normalization Factor
Khan, Greeves [36, 37]	KG	220
Delichatsios et al. [32-35, 43]	D	0.90
Tesner [48]	T	18 $k_{inc} = 2E4$
Moss et al. [50]	M	0.049
Leung-Lindstedt [47]	LL	1.44
Lindstedt A [56]	La	3.05
Lindstedt B [56]	Lb	2.12
Lindstedt C [56]	Lc	0.6
Lindstedt D [56]	Ld	1.13
Moss-Brookes [29]	MB	3.75
Moss-Brookes-Hall [57]	MBH	0.375

Table 4-2. Normalization factors used for soot formation rates.

4.3 Supplemental Material
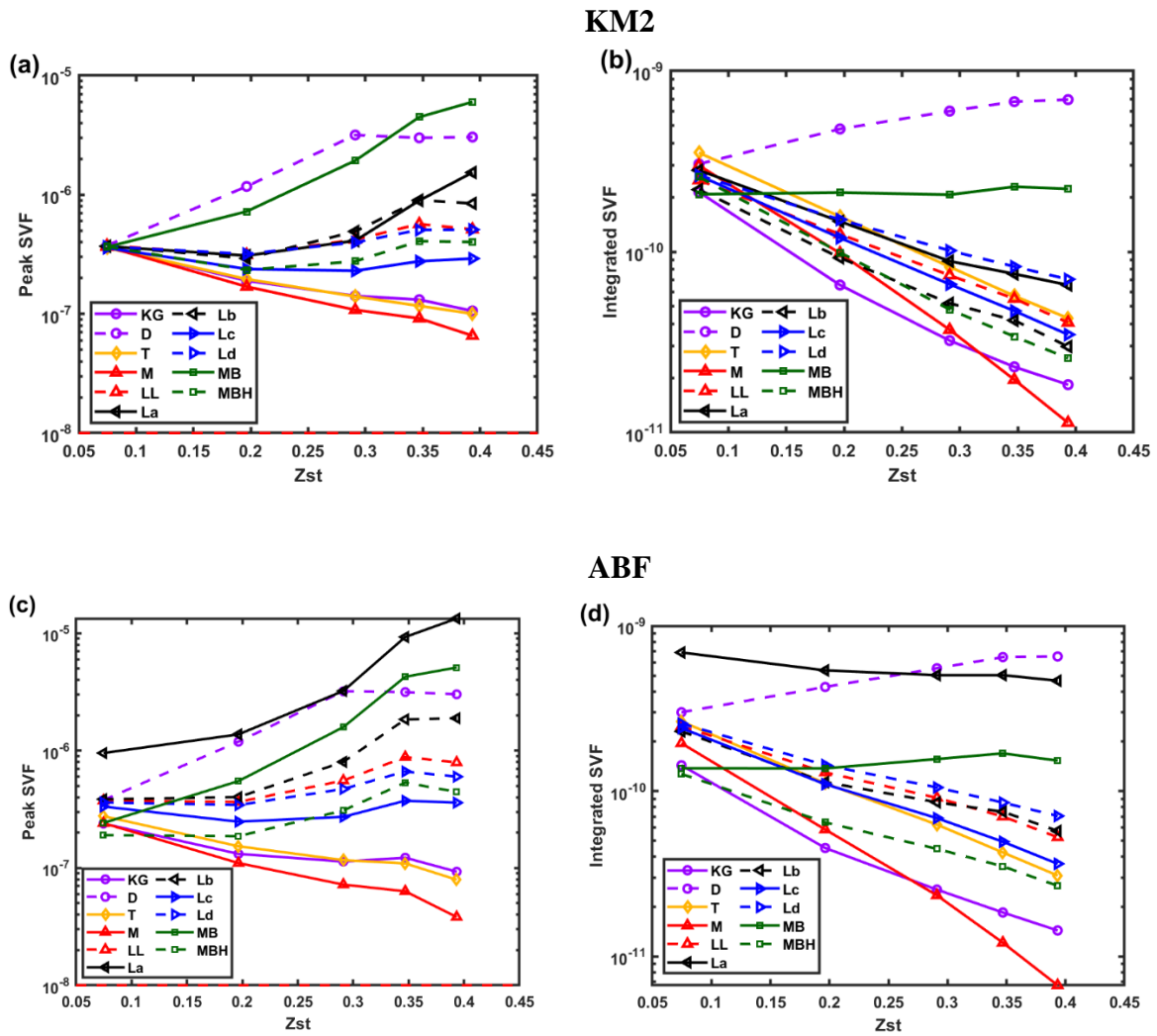
Figure 4-9. The effect of gas combustion mechanism on peak and integrated *svf* for changing Z_{st}. a) peak *svf*, KM2, b) integrated *svf*, KM2, c) peak *svf* ABF, d) integrated *svf*, ABF. Figures 4-7a,b are reproduced in Section 5 but are shown here for ease of comparison.

KM2
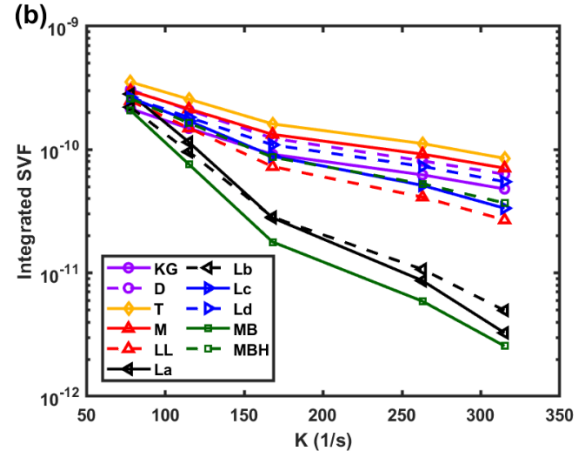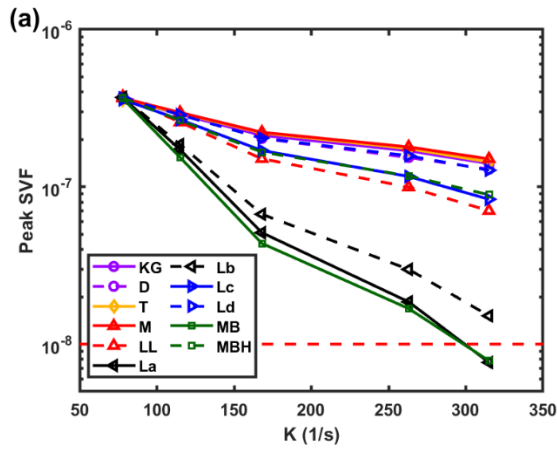
ABF
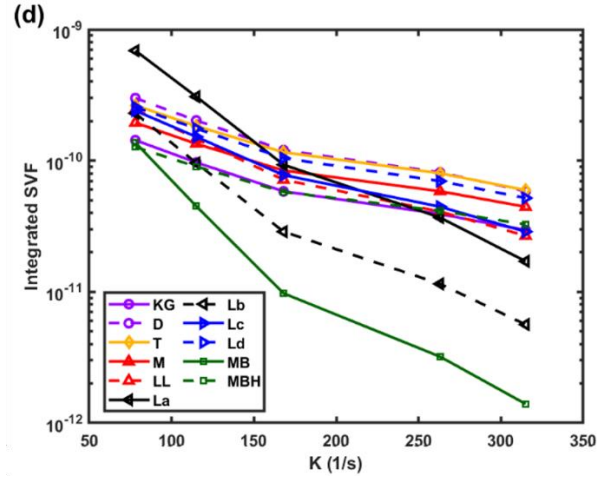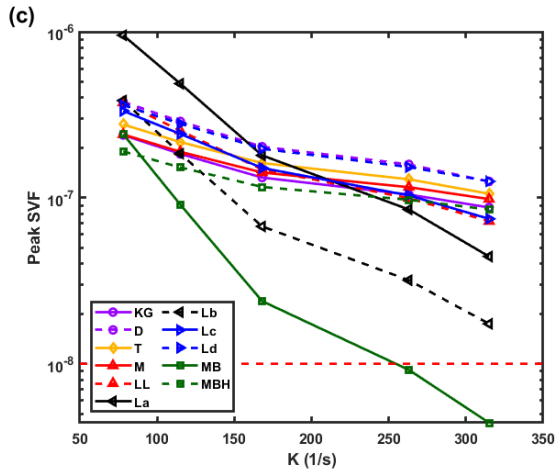
Figure 4-10. The effect of gas combustion mechanism on peak and integrated *svf* for changing *K*. a) peak *svf*, KM2, b) integrated *svf*, KM2, c) peak *svf* ABF, d) integrated *svf*, ABF. Figures 4-8a,b are reproduced in Section 5, but shown here for ease of comparison.

With Soot Oxidation

(a)

(b)
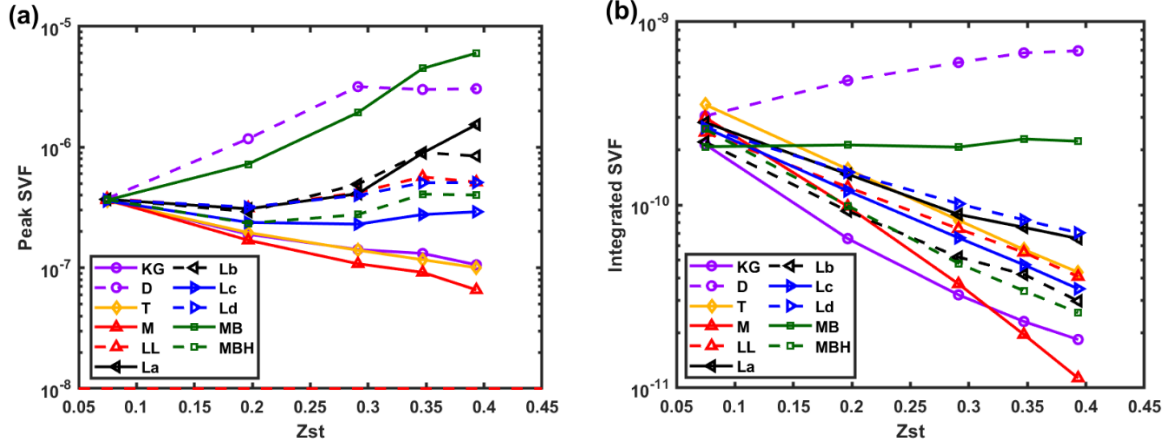
Excluding Soot Oxidation

(c)

(d)
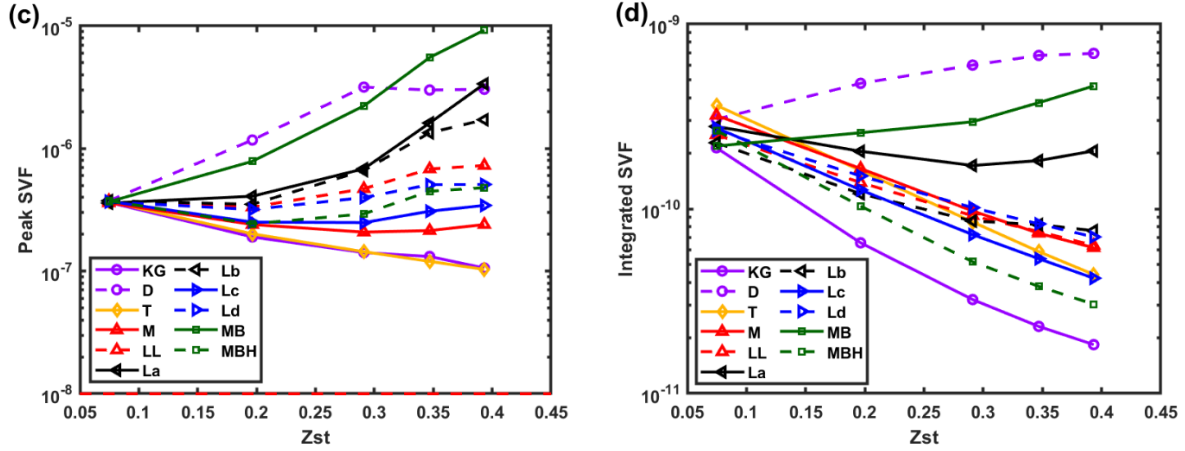
Figure 4-11. The effect of oxidation on peak and integrated *svf* for changing Z_{st}. a) peak svf with oxidation, b) integrated svf with oxidation, c) peak *svf* without oxidation, d) integrated *svf* without oxidation. Figures 4-9a,b are reproduced in Section 5, but shown here for ease of comparison.

Oxidation occurs, according to the model rate equations, due to attack from OH (M, MB, MBH) or O_2 (LL, La-d) which has leaked across the flame front. The region of oxidative attack is far away from the bulk region of soot formation and growth for most models ($\Phi > 0.6$). The largest effect due to oxidation is observed in the Moss model, which displays for $Z_{st} = 0.393$ a variance of peak *svf* by a factor of 3 and a variance of integrated *svf* by a factor of 5. All other models show a modification by less than a factor of 2 for $Z_{st} = 0.393$ (the flame condition with the highest svf variability) when comparing the two cases. The reason for the strong effect of oxidation on the Moss model is its fitting constants (namely its high Arrhenius temperature) result in a prediction of a soot formation zone which, compared to the other models, is much closer to the flame (see Section 5), which is where the oxidative species are more abundant.

Chapter 5: Semi-Empirical Model Results

5.1 Z_{st} Evaluation Results

Results for the Z_{st} evaluation (flame series 1) are shown in Fig. 5-1, which includes the predicted peak (Fig 5-1a) and integrated (Fig. 5-1b) *svf* as a function of Z_{st} at constant adiabatic flame temperature. Recall from Fig. 4-1 that Flame 1.4 ($Z_{st} = 0.4$) was experimentally determined to be blue. Nonetheless, all models predict significant fractions of soot at this flame condition, and all models, with the exception of the Moss (M) model (factor of six), predicted a peak *svf* of at least one order of magnitude above the diagnostic soot detection limit of 10^{-8}. Several models predicted increases in peak *svf* as Z_{st} increased and some showed only minor variation. Three models, Delichatsios and Moss-Brookes and Lindstedt A, showed monotonic increases in integrated *svf* (total soot formed) over the range of Z_{st}.
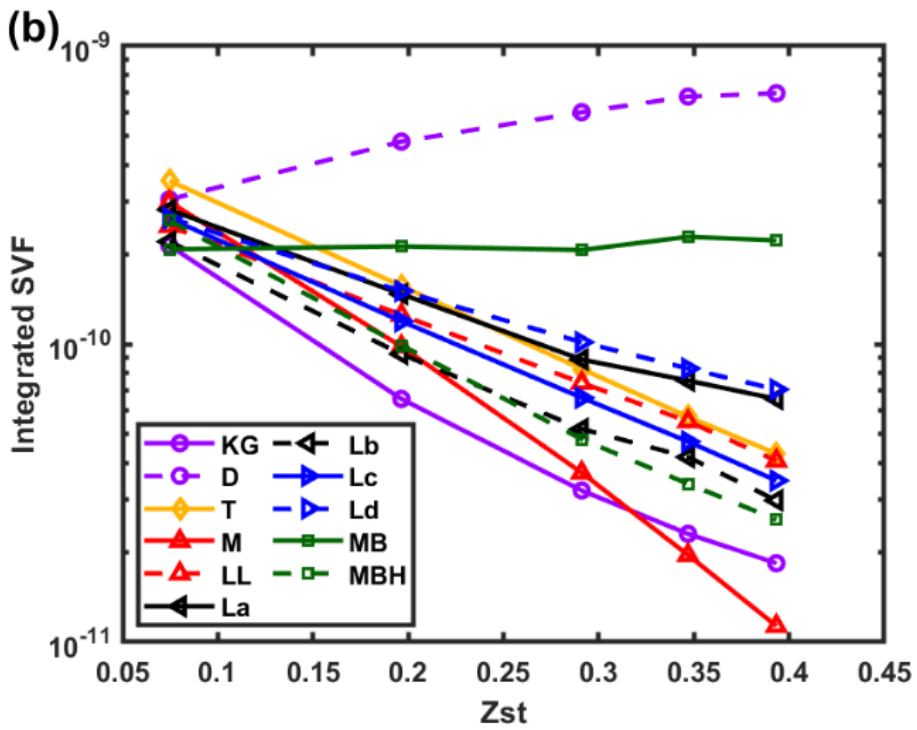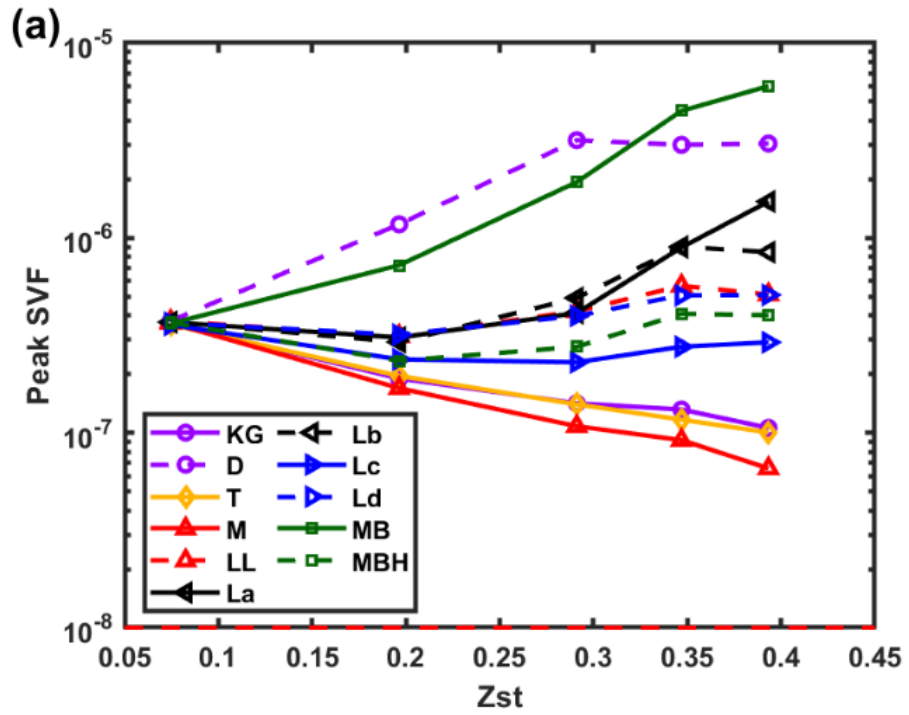
Figure 5-1. Collective results for all semi-empirical models for flames with increasing Z_{st}. a) peak svf vs. Z_{st} b) integrated svf vs. Z_{st}.

To better understand the underlying causes of these results, a unique analytical approach is taken. The profiles of soot formation rate and other key quantities are plotted in local equivalence ratio (Φ) space. It is advantageous to plot the results in Φ space, as opposed to physical space, in order to deemphasize the effects of fluid convective flow on the profile shape and focus attention on how key quantities are related to the overall progress of fuel conversion. While Z space (Z) is often used, it is less helpful for these studies since the flame location varies in Z space when Z_{st} is modified, leading to a more complicated result when results from many flames are plotted together. Local C/O ratio has been also proposed as a preferred space to study soot formation in non-premixed flames [48]. The quantity chosen for this work, φ, can be calculated numerous ways, either in terms of unburned reactants or in terms of Z, as in Eq. (5-1). It can also be derived from mass of atomic carbon, hydrogen, and oxygen, as is commonly done in CFD packages such as ANSYS Fluent.

$$\varphi = \nu * \frac{Y_{F,U}}{Y_{O,U}} = \frac{Z}{1-Z} * \frac{1-Z_{st}}{Z_{st}} = \frac{{}^{m_C+m_H}/m_O}{\left({}^{m_C+m_H}/m_O\right)_{ST}} \tag{5-1}$$

A normalized φ is used in this study to obtain a finite range of values:

$$\Phi = \frac{\varphi}{\varphi+1} \tag{5-2}$$

Some potential advantages to using local equivalence ratio are: 1) Like Z and C/O ratio, φ is invariant with chemical reaction; 2) Unlike Z and C/O, the location of stoichiometry does not change with flame conditions or with fuel species, being always located at $\varphi = 1$, ($\Phi = 0.5$). and 3) φ includes hydrogen, which is considered to play an important role in soot formation and in the cessation of soot formation [19].

An example of soot growth rate in Φ space for low-Z_{st} flames can be seen in Fig. 5-2, which was obtained by calculating the formation rate from the conservation equation and using measured

svf profiles [2]. The *svf* profiles used are from Hwang et al. [2], Wang et al. [81], and Xu et al. [82]. The Wang data set corresponds to the low Z_{st}, low K flame used in the evaluation (and for normalization) and can be considered a helpful guide for visualizing soot formation rate in Φ space. The soot formation zone is bounded on the left-hand side around $0.60 < \Phi\ 0.65$ and around $0.90 < \Phi < 0.95$ on the right hand side, and peaks between $0.70 < \Phi < 0.80$. The left boundary corresponds to a critical location where soot inception and growth are no longer favorable. Skeen et al. noted that, for ethylene flames, aromatic ring formation is cut off where C/O < 0.53 (corresponding to $\Phi < 0.64$) and this was attributed to the location of abundance of H^+ radicals. The right boundary corresponds to the location of the *psp*, where particles are ejected from the system.
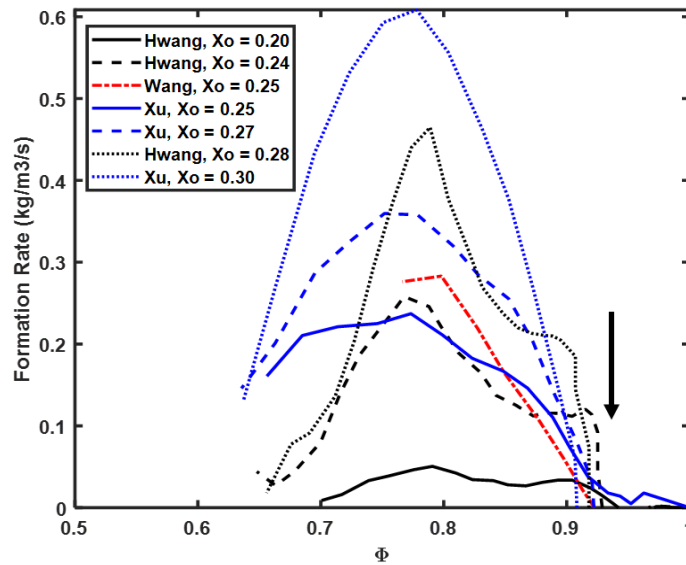
Figure 5-2. Soot formation rate vs. Φ, calculated from experimental data from Hwang et al. [2], Wang et al. [81], and Xu et al. [82]. The arrow denotes the location of the *psp* for all flame condtions.

Soot formation rates for all semi-empirical models are plotted as a function of Φ in Fig. 5-3. By inspecting these models in Φ space, several important features are highlighted. The results in Fig. 5-3(a) reveal a large variation in the resulting soot formation zones across all models, even

53

in this case of the "typical" low- Z_{st} flame. Location of peak soot formation varies from $\Phi = 0.58$ (Tesner) to $\Phi = 0.83$ (Khan). Many models show a formation rate with similar bounds as observed in Fig. 5-2, especially for those which are dependent on C_2H_2 for surface growth. The Tesner model also show peak production shifted towards the flame as a result of their high Arrhenius temperature. In contrast, the model of Khan-Greeves shows less soot production when $\Phi < 0.83$ (location of peak formation) as a result of the ϕ^3 term in Eq. (2-3), as compared to all other models. All models show a formation rate bounded on the right-hand side by the *psp*, as seen in Fig. 5-2. As Z_{st} is increased the *psp* shifts to lower values of Φ and higher temperature and intrudes into the soot formation zone (Fig. 5-3c-e). As a result, surface growth abruptly ceases for some models (La, Lb, MB) because the *psp* has been reached and there is no longer any surface on which to grow. Note that this behavior is not observed for one-step models (KG, D, Ld), which show varying amounts soot formation on both sides of the *psp*. The observed effects of increasing Z_{st} on select individual soot model performance is described below in more detail, beginning with one-step models.
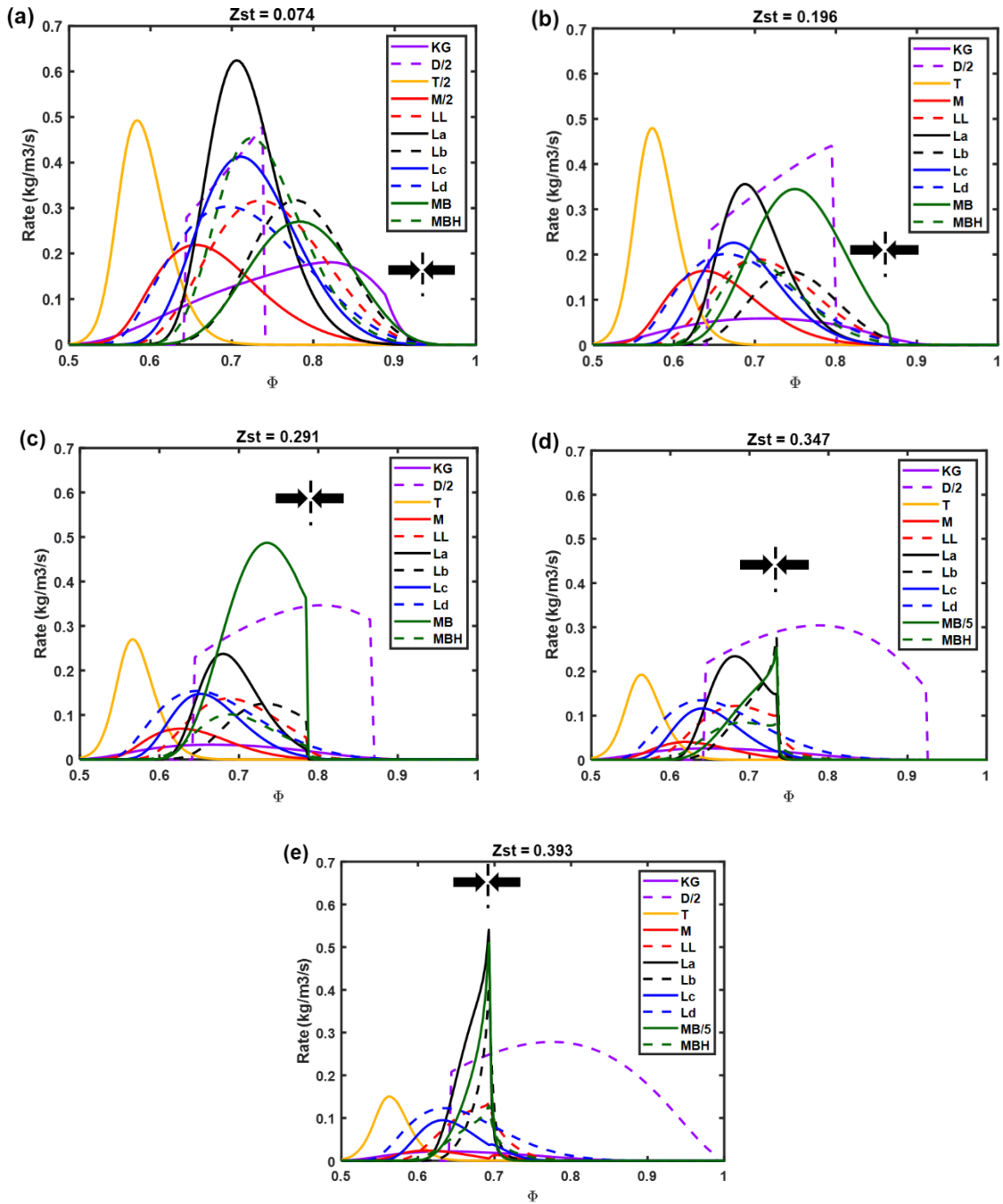
Figure 5-3. Total soot formation rate predictions from semi-empirical models vs. Φ for a) $Z_{st} = 0.064$, b) $Z_{st} = 0.196$, c) $Z_{st} = 0.291$, d) $Z_{st} = 0.347$, e) $Z_{st} = 0.393$. Some models are scaled (see legend). The arrows denote the direction of flow for particles and the dashed vertical lined indicates the *psp*. The reader is referred to the online version for color.

Results of the Khan model for *svf* and formation rate are shown in Fig. 5-4. As Z_{st} increases, the Khan model is strongly affected by dilution through its dependence on fuel concentration and by the Φ-temperature relationship. This results in a sharp reduction in soot formation rate with increasing Z_{st}, and a shift in location of peak formation to lower Φ.
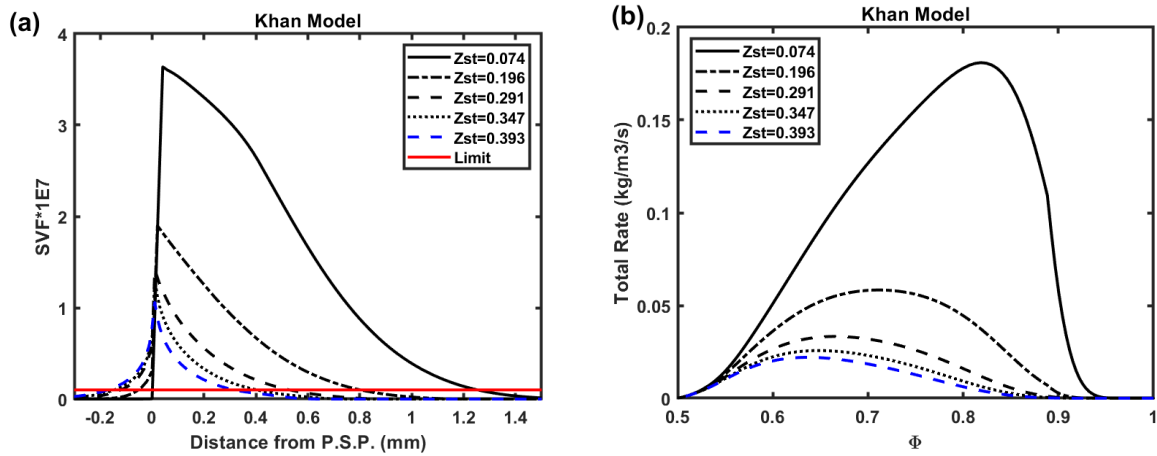
Figure 5-4. Results from the Khan model for all Z_{st} in the changing Z_{st} evalulation; a) *svf* vs. distance from *psp*; b) total formation rate vs. Φ. Soot-free flame designated in blue. Diagnostic limit for *svf* shown in a) by red line.

Results of the Delichatsios model for *svf* and formation rate are shown in Fig. 5-5. This model has a soot production profile that is unique among other models, due to its formulations of the boundaries of the soot formation zone described in Eq. (6). The "oxidation" boundary, where soot formation stops was based on an experimentally-determined local C/O ratio at the soot inception limit [35, 46]. The "critical" low-temperature onset boundary, where soot formation begins, was based on a multiple of Z_{st} (see Eq. 2-10). Consequently, the low-temperature onset boundary shifts in the wrong direction by increasing the zone of soot formation, as seen throughout Fig. 5-5. For this reason, the soot production zone grows larger for higher Z_{st}, leading to the increase of integrated *svf* with increased Z_{st} as seen in Fig. 5-1b. Also, the profile mainly trends with fuel concentration due to the low Arrhenius temperature of the model.
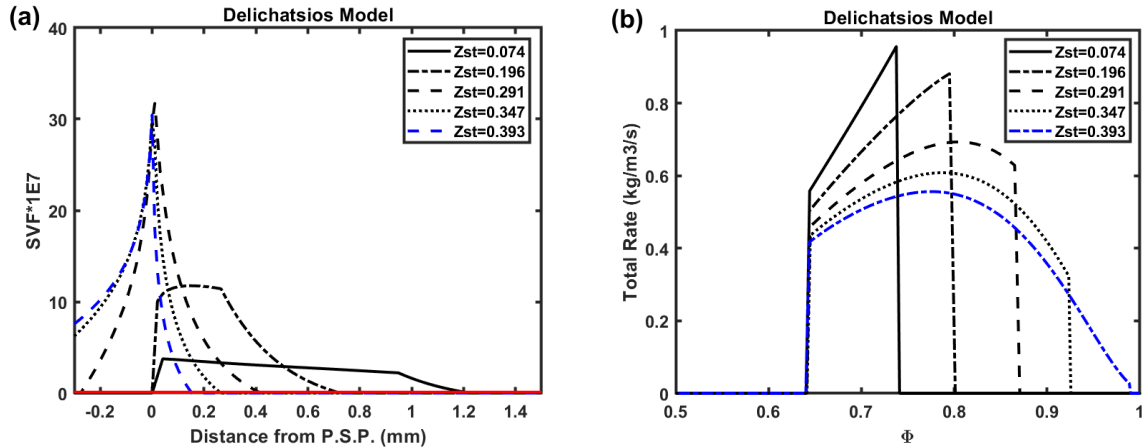
Figure 5-5. Results from the Delichatsios model for all Z_{st} in the changing Z_{st} evalulation; a) svf vs. distance from psp; b) total formation rate vs. Φ. Soot-free flame designated in blue. Diagnostic limit for svf shown in a) by red line.

The Tesner model is shown Fig. 5-6. The high Arrhenius temperature in the inception term for soot precursors (Eq. 8) biases the peak formation rate to lower Φ. For all other two-step models, any increase in the amount of mature soot mass results in increased capacity for soot production through the various surface growth functions. However, increased mature soot mass in the Tesner model does not yield a greater propensity for growth, but rather leads to diminished production due to "termination" terms in the production rate equation for both soot precursors (third term in Eq. 2-11) and mature soot (second term in Eq. 2-13).
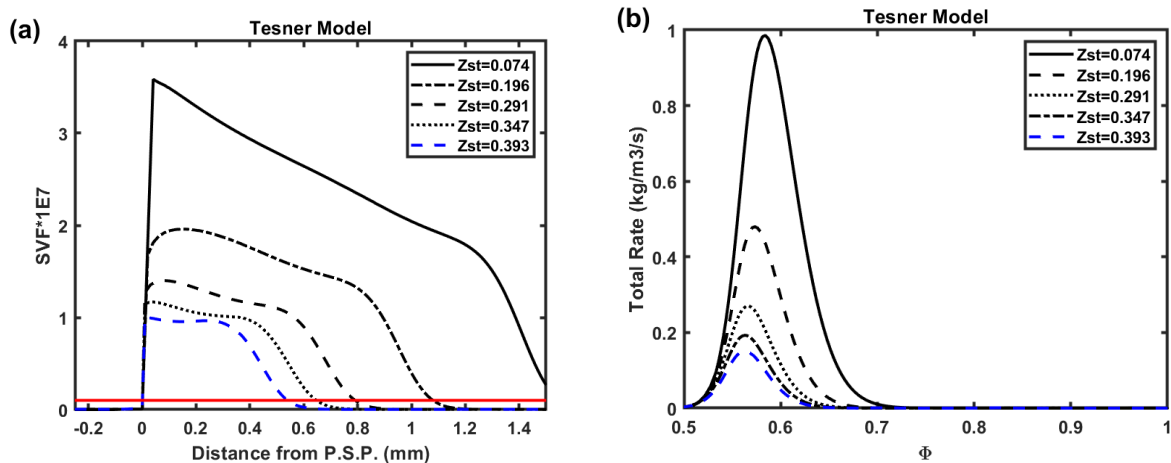
Figure 5-6. Results from the Tesner model for all Z_{st} in the changing Z_{st} evalulation; a) *svf* vs. distance from *psp*; b) total formation rate vs. Φ. Soot-free flame designated in blue. Diagnostic limit for *svf* shown in a) by red line.

Some key trends associated with the remaining two-step models are generally observed. Two-step models produce soot mass mainly through surface growth reactions, which are coupled to existing soot mass and/or particle number through the surface area term. Some unique features in these models are observed which result from the combination of surface growth dominance and the changes to flame structure for increases in Z_{st}; e.g. the counter-intuitive observation of increased peak *svf* as Z_{st} increases, which has also been observed in other modeling results [83].

Consider the case of a fuel-air flame, where soot is generated and then transported to the *psp*. Here the *svf* reaches a peak, as it accumulates on the *psp*. The magnitude of the peak is determined by the amount of soot generated chemically and by the balance in the mass flux. For these types of flames, the region of soot generation is distinct from the location of peak *svf*. When Z_{st} is increased, the region of physical space between the flame and the *psp* narrows, increasing the mass gradient and yielding a higher peak *svf*. Additionally, soot production now occurs at the *psp* (and thus the location of peak *svf*), because it shifts into the surface growth region where higher temperature and abundant growth species reside.

These simultaneous contributions lead to rapid increase in *svf* at the *psp* and can explain how peak *svf* can increase even while integrated *svf* decreases (less total soot) for many two-step models. However, to explain why some two-step models predict increased integrated *svf* with increased Z_{st}, a third factor must be considered: the positive feedback between soot mass and soot production rate which results from the two factors above. Changes in soot mass and number affect the particle surface area, which is a critical component to surface growth in these models. When soot mass increases rapidly, such as near the *psp* and especially when the first two effects are simultaneously present, the surface growth *rate* is significantly augmented, which further increases soot mass, etc. This feature can strongly affect model results (see discussion below). Feedback occurs for all two-step models, but the feedback strength is dependent on each model and its respective sensitivity to either the surface area factor or the chemical Arrhenius factor, defined in Eq. (5-3).

$$\omega_{SG} = \underbrace{f(S)^a}_{Surface\ Area\ Factor} \cdot \underbrace{[Precursor]^b \cdot \exp\left(-\frac{T_A}{T}\right)}_{Chemical\ Arrhenius\ Factor} \tag{5-3}$$

The Moss model (Fig. 5-7) results in a steep and steady decline in the total formation rate with increasing Z_{st} (but does not predict the blue limit). In this model $f(S) = n,\ a = 1,\ b = 1$ and the "surface area" is quantified by the particle number (see Eq. 2-14). As with all two-step models considered here, particle number is depleted due to coagulation. For the Moss model $\omega_{SG} \sim n$ and is therefore more strongly affected by coagulation, as compared to other models.
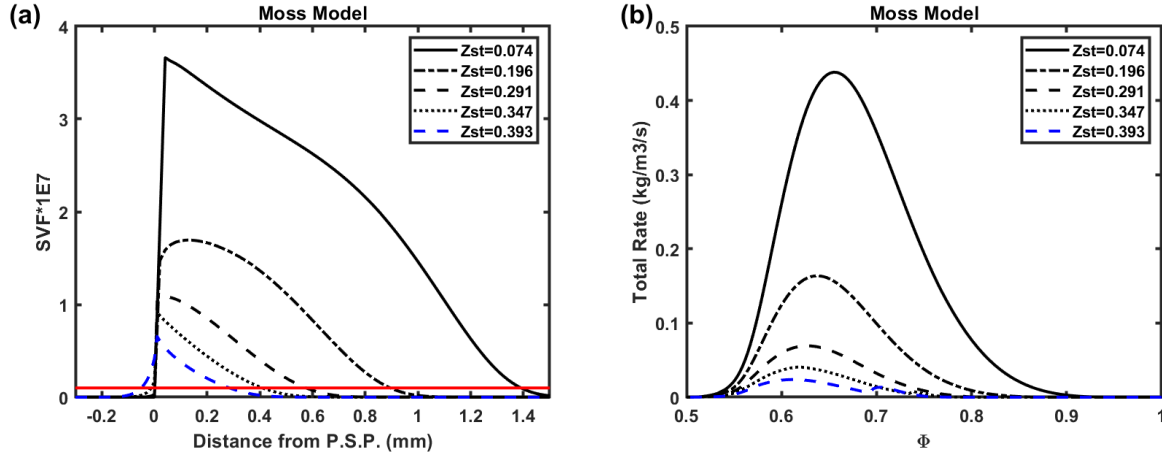
Figure 5-7. Results from the Moss model for all Z_{st} in the changing Z_{st} evalulation; a) svf vs. distance from psp; b) total formation rate vs. Φ. Soot-free flame designated in blue. Diagnostic limit for svf shown in a) by red line.

The results for the Leung-Lindstedt and Lindstedt a-d models are shown in Fig. 5-8. For Leung-Lindstedt, $(S) = A_s$, $a = 0.5$, $b = 1$, in Eq. (5-3). It has a reduced dependence on surface area which is physcially attributed to surface aging. The formation rate(s) subsequently follow the chemical Arrhenius factor unless psp interference occurs. Noticeable but minor feedback can be observed for higher Z_{st} flames. The reduced dependence on surface area prevents the feedback scenario described above.

For Lindstedt A, $f(S) = \chi A_s$, while for Lindstedt B, $f(S) = A_s$. For both of these models, $a = 1$, $b = 1$. Both models show significant feedback behavior for higher Z_{st} flames due to the linear dependence on surface area, which is a function of existing soot mass. This behavior is weaker for Lindstedt A because the χ term biases the formation rate towards lower Φ, thus reducing the psp interference. For Lindstedt C, $f(S) = n$, $a = 1$, $b = 1$. This model was considered the best performing model in the originating publication [56] and this model also performs the best for this evaluation. Because of the linear dependence on particle number of this model, its behavior is similar to that of the Moss model (see comments above), with the exception

60

of location in Φ-space due to a different soot precursor species and Arrhenius temperature. Finally, for Lindstedt D, $f(S) = constant,\ a = 0,\ b = 1$ – there is no dependence on particle number or existing soot mass (this model can be classified as a one-equation model). The soot formation zone is therefore broader with no effects from the *psp* and only decreases due to the reduction in C_2H_2 and temperature as Z_{st} increases.
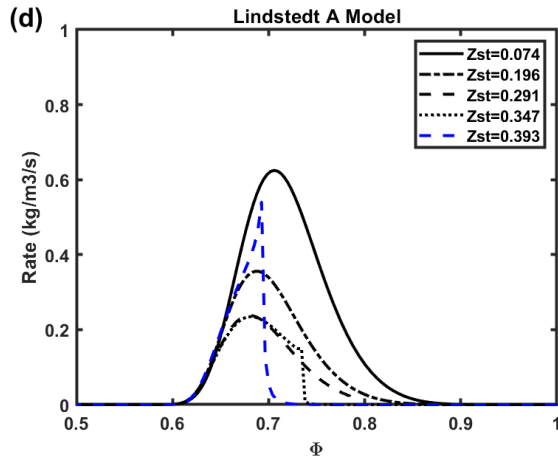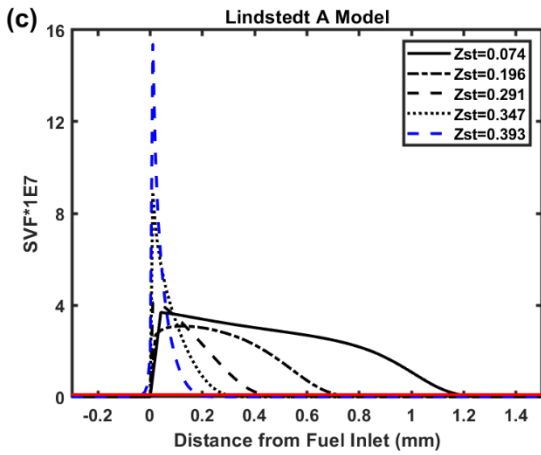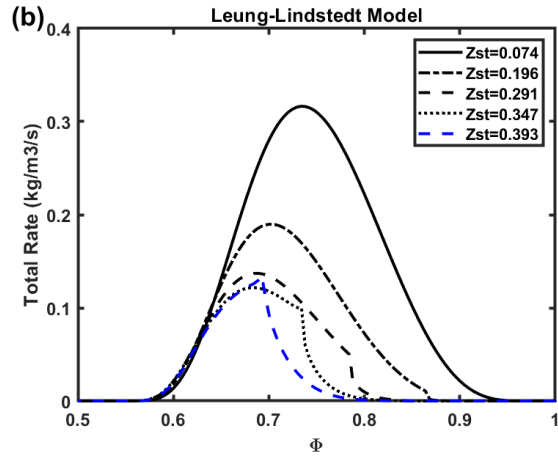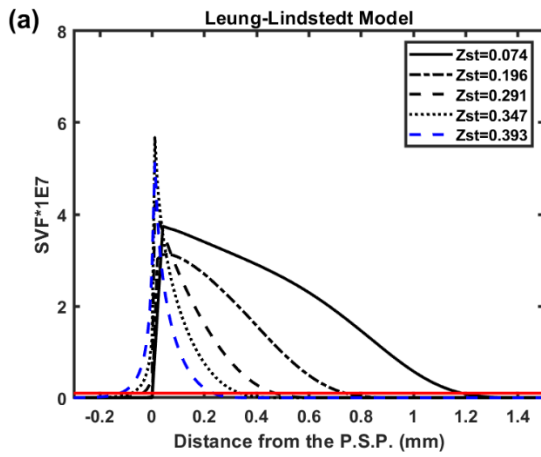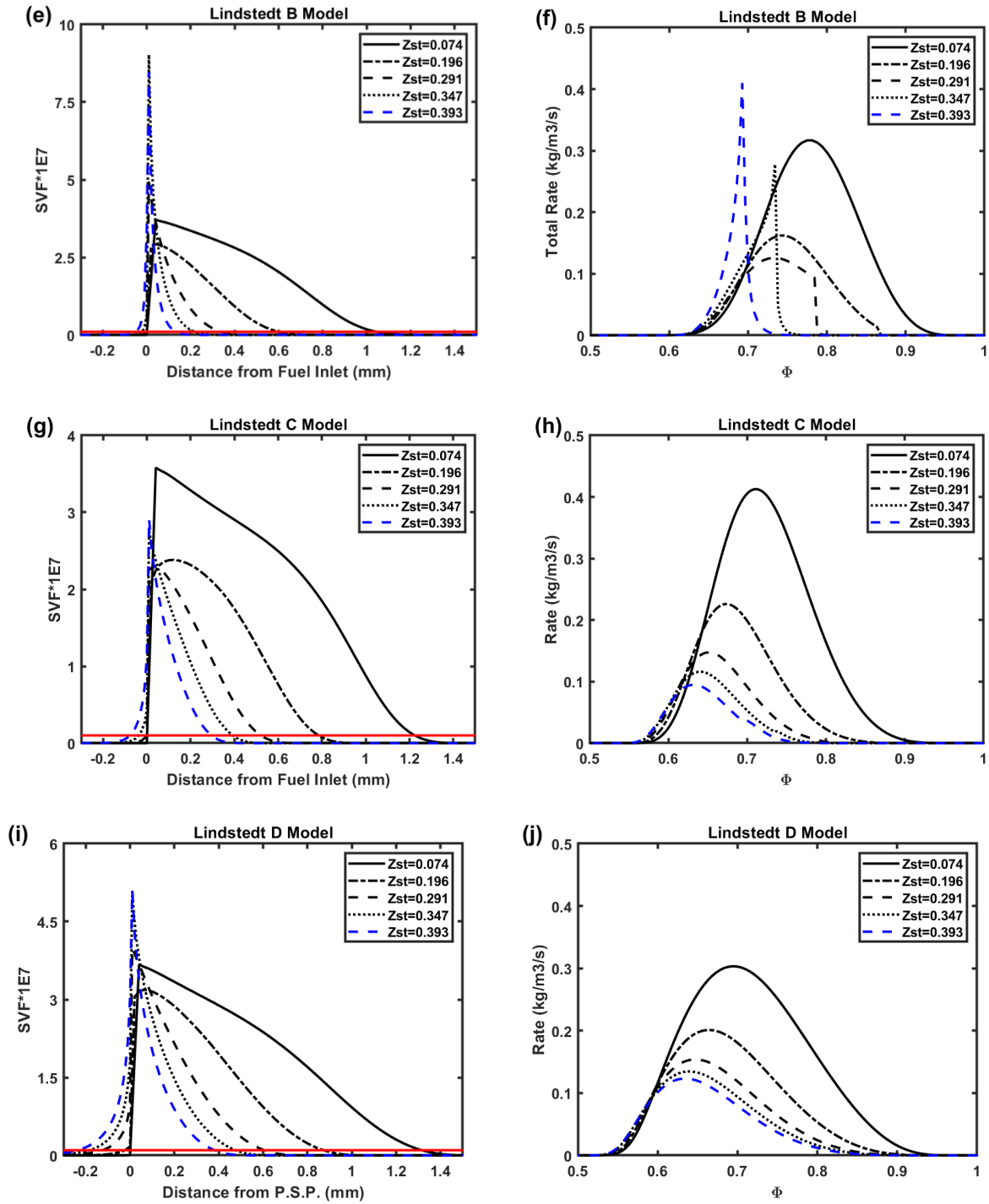
Figure 5-8. Results for all Z_{st} in the changing Z_{st} evaluation; a) Leung-Lindstedt *svf* vs. distance from *psp*; b) Leung-Lindstedt total formation rate vs. Φ. c) Lindstedt A *svf* vs. distance from *psp*; d) Lindstedt A total formation rate vs. Φ; e) Lindstedt B *svf* vs. distance from *psp*; f) Lindstedt B total formation rate vs. Φ; g) Lindstedt C *svf* vs. distance from *psp*; h) Lindstedt C total formation rate vs. Φ; i) Lindstedt D *svf* vs. distance from *psp*; j) Lindstedt D total formation rate vs. Φ; Soot-free flame designated in blue. Diagnostic limit for *svf* shown in a) by red line.

The results for the Moss-Brookes and Moss-Brookes-Hall models are shown in Fig. 5-9. For both models $(S) = A_s$, $a = 1$, $b = 0.4$ in Eq. (5-3) and surface growth production consequently is heavily dependent on surface area and less dependent on the chemical Arrhenius factor. The Moss-Brookes model hits a critical feedback as described above and incorrectly predicts an increase in integrated *svf* (total soot formed) with increased Z_{st}. This result could be interpreted to confirm the surface area aging and/or call into question the difference in chemical growth of soot between counterflow and coflow flames, since Leung-Lindstedt was developed for the former and Moss-Brookes was developed for the latter. This feedback behavior could also be expected for the Moss-Brookes-Hall model, but this model has such a high inception rate that it (incorrectly) contributes largely to soot mass formation and reduces the dependence of the total formation rate on surface growth, see Fig. 5-10. Such a high inception rate is potentially due to this model's targeted application to kerosene pool fires and not for light gaseous fuels such as C_2H_4. Note that at higher Z_{st} there is still an effect from *psp* interference even for this model.
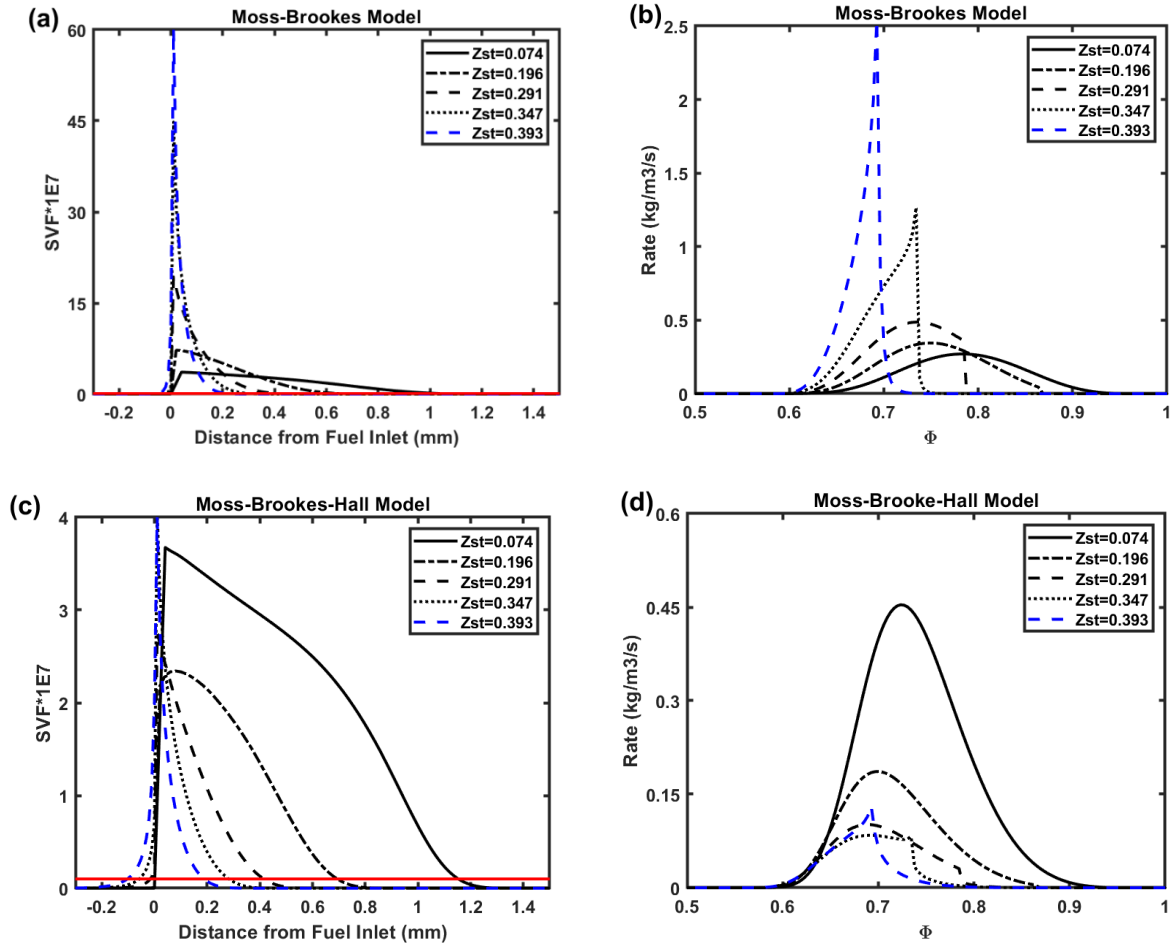
Figure 5-9. Results for all Z_{st} in the changing Z_{st} evalulation; a) Moss-Brookes *svf* vs. distance from *psp*; b) Moss-Brookes total formation rate vs. Φ; c) Moss-Brookes-Hall *svf* vs. distance from *psp*; d) Moss-Brookes-Hall total formation rate vs. Φ. Soot-free flame designated in blue. Diagnostic limit for *svf* shown in a) by red line.
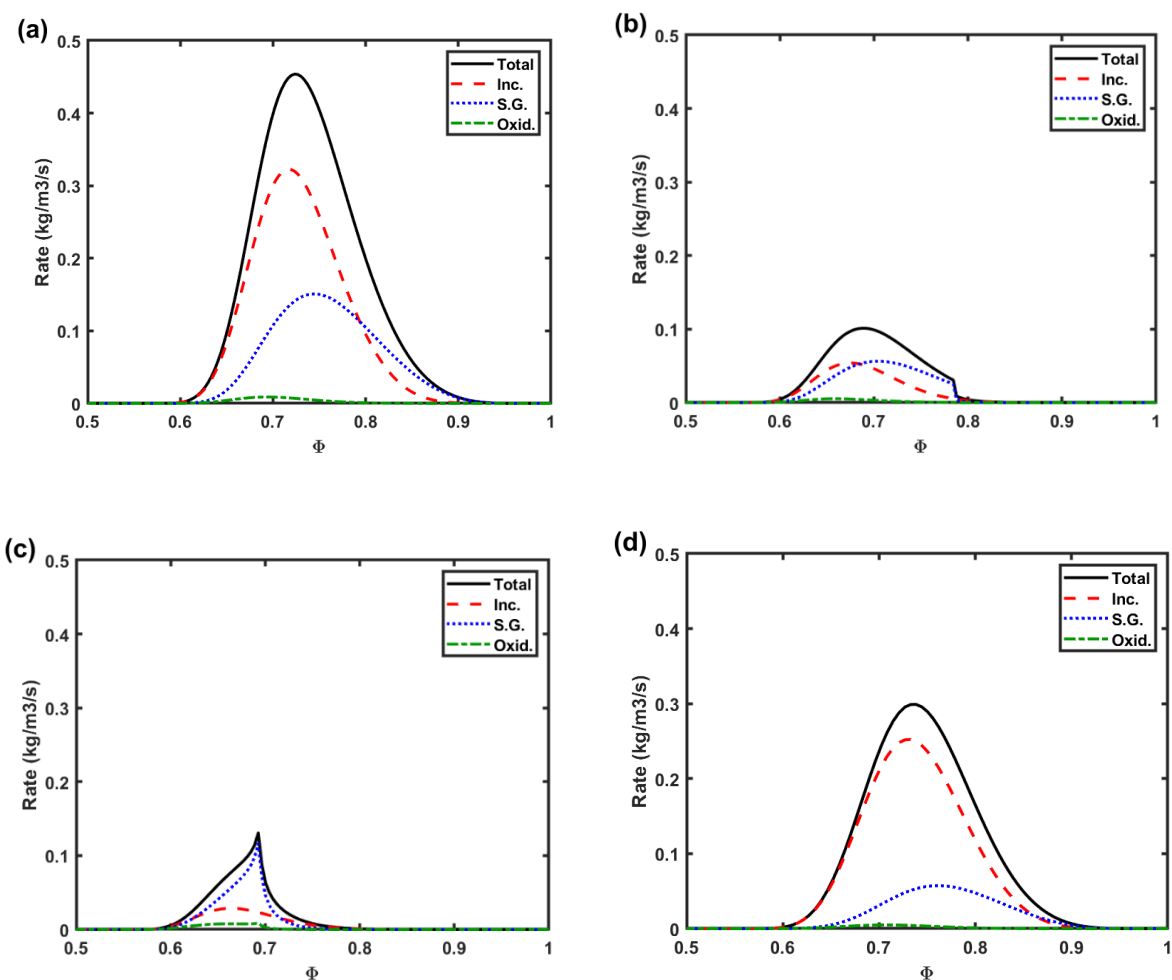
Figure 5-10. Rates of inception, surface growth, and total formation rate for the Moss-Brookes-Hall model in Φ space for: a) $Z_{st} = 0.074$, $K = 78$ 1/s, b) $Z_{st} = 0.291$, $K = 78$ 1/s, c) $Z_{st} = 0.393$, $K = 78$ 1/s, d) $Z_{st} = 0.074$, $K = 315$ 1/s

All semi-empirical models above propose soot formation to be a process of irreversible pyrolysis from fuel. This conceptual way of predicting soot cannot account for the reversibility and suppression of soot chemistry which occurs at higher Z_{st}, as mentioned in Section 2 and further investigated in Section 6 below. These processes are not typically considered in the development of semi-empirical soot models. Therefore, existing semi-empirical models which conceptualize soot inception as a direct pyrolysis pathway and cannot predict this reversibility and subsequent

soot suppression. For these models, soot will always form in the presence of sufficient fuel and temperature.

5.2 K Evaluation

Results for the strain (K) evaluation are shown in Fig. 5-11. Two models (MB, La) were able to predict a blue flame at the inception limit with a third model (Lb) also showing notable reduction. All other models showed only minor reductions in soot formation. The behavior of these models is more straightforward to interpret without a shifting *psp*. Individual model results are shown in Fig. 5-13(a-v); all models yield a reduction in peak *svf*, even when the formation rate is not changed significantly. The *svf* decreases necessarily when velocity is increased due to mass conservation (from an Eulerian perspective, mass is reduced to conserve the mass flux in the continuity equation as velocity increases; from a Lagrangian perspective, there is a reduced residence time for a parcel of fuel to form soot) . The clearest example can be seen in comparison of Figs. 5-13c,d where there is no change in rate but a reduction in *svf* proportional to the increase in *K*. However, many models (M, LL, La-c, MB, MBH) also show a reduction in formation rate (Figs. 5-13 h, j, l, n, p, t, v), especially for two-step models, which further contributes to reductions in *svf*. This reduction is primarily due to the feedback mechanism mentioned in the previous section. Whereas previously there existed positive feedback for increasing Z_{st} due to *psp* intrusion, there is now negative feedback: reduced soot mass and / or particle number due to increased flux reduces the surface area, which reduces the surface growth rate, which reduces the mass, etc. This feedback is strongest for Lindstedt A, B and Moss-Brookes because of the linear surface area dependence of these models (see Eq. 5-3 and notes above). While these models result in incorrect trends in the Z_{st} evaluation, they are the best-performing models for the *K* evaluation.
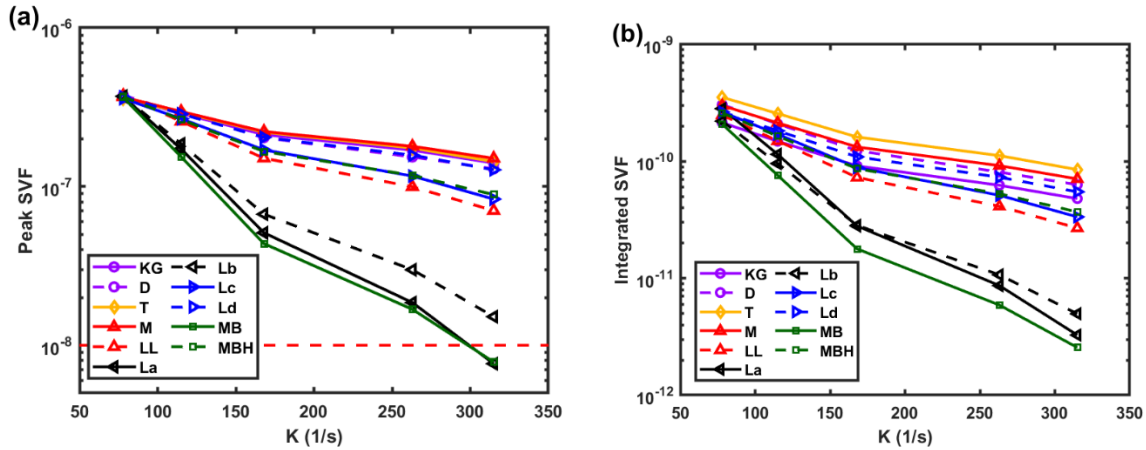
Figure 5-11: Collective results for all semi-empirical models for flames with increasing *K*. a) peak *svf* vs. *K* b) integrated *svf* vs. *K*.

A few additional notes are given on specific models, with corresponding rate profiles shown together in Fig. 5-12. The first three models show either no change in formation rate (Delichatsios model) or a slight increase in rate (Khan, Tesner models). As mentioned above, for all three of these models, *svf* drops as *K* increases solely due to mass flux.

For the Khan model, the trend in rate is based on the local temperature and the bias in peak rate caused by the use of ϕ^3, which causes the location of peak soot production to be shifted to the region of $\Phi > 0.8$. Detailed chemistry was used for the gas flame simulations with the result that there are minor differences in the temperature profiles across this series of flames. In the region of $0.7 < \Phi < 0.9$, the local temperature was found to increase by up to 25 (K) with increasing strain (Fig. 5-12). Subsequently, the Khan model predicts higher soot formation with increased strain, following the temperature trend in this region.
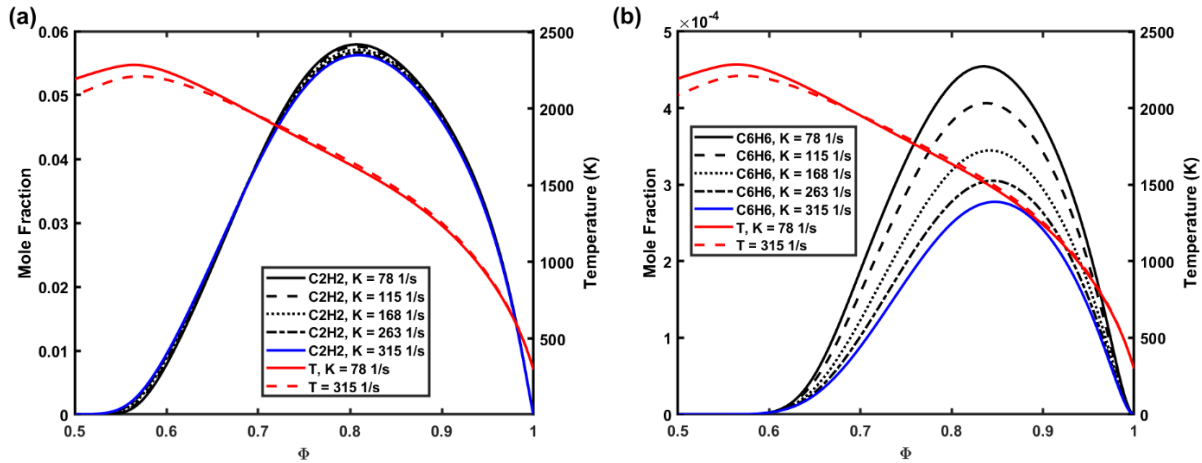
Figure 5-12. Mass fraction and temperature in Φ space for increasing K. a) C_2H_2 b) C_6H_6

Recall that the Tesner model is highly coupled, with soot number increasing linearly with particle number (nascent concentration in Eq. 2-11 and mature concentration in Eq. 2-13) and decreasing with the square of particle number (nascent multiplied by mature concentration for both Eqs. 2-11, 2-13). Also note that both the nascent and mature particle concentration will drop due to the mass flux as strain increases. This change results in a larger decrease in the coagulation terms, as compared to the formation terms, upon increasing strain. Accordingly, the net production of particles is predicted to slightly increase with strain.

The Moss model has the same temperature feature as the Khan model for increased strain. Additionally, surface growth in the Moss model is based on particle number, which drops with increased strain due to mass flux. However, the increase to rate due to temperature is greater than the decrease due to particle number.

For the remaining two-step models, all have some form of negative feedback described above in context of the Moss-Brookes model. For all these models, *svf* and/or particle number drops as K increases due to mass flux while also having notable reductions in formation rate. The

rate for the Leung-Lindstedt model decreases notably, but because of its diminished dependence on surface area (attributed to surface aging) the feedback is insufficient to predict a blue flame.

Lindstedt A and B both display strong negative feedback from their surface area dependence described above. Lindstedt A predicts a blue flame for this evaluation. The effect of the HACA term (χ) in Eq. (2-23) on Lindstedt A is a shift in the formation rate to lower Φ and a narrowing of the formation rate profile. Lindstedt C does not exhibit strong feedback behavior because its surface area function depends on particle number alone. Lindstedt D has no change in rate because there is no 'surface area' dependency (Eq. 2-25) and therefore no feedback. The surface growth is only affected by C_2H_2 and temperature, both of which are rather insensitive to K.

The Moss-Brookes rate is very sensitive to K due to the feedback from its strong surface area dependence and can thus accurately predict a blue flame (see above). The Moss-Brookes-Hall rate, because it has strong contributions from the inception rate, has a diminished feedback behavior with respect to surface growth. However, unlike Lindstedt D which was very dependent on C_2H_2, the Moss-Brookes-Hall model shows some sensitivity to K despite lacking significant feedback. This is because the Moss-Brookes-Hall inception term is dependent on aromatic species which are more sensitive to K than C_2H_2 (see Supp. Fig. 5-12). A similar trend has been noticed in turbulent combustion modeling, where a larger aromatic species (A_2) was shown to be more sensitive to scalar dissipation than C_2H_2 [65].

(m) Lindstedt B Model

(n) Lindstedt B Model

(o) Lindstedt C Model

(p) Lindstedt C Model

(q) Lindstedt D Model

(r) Lindstedt D Model

72
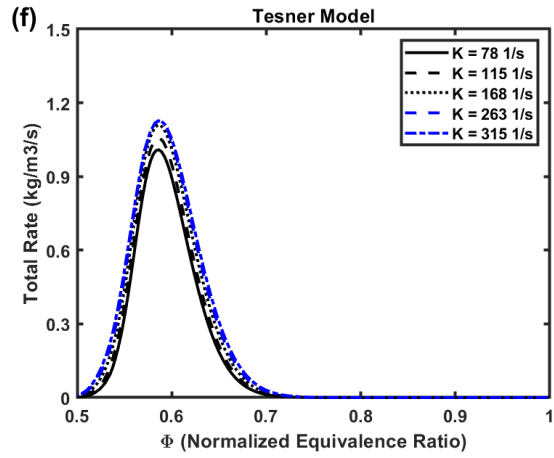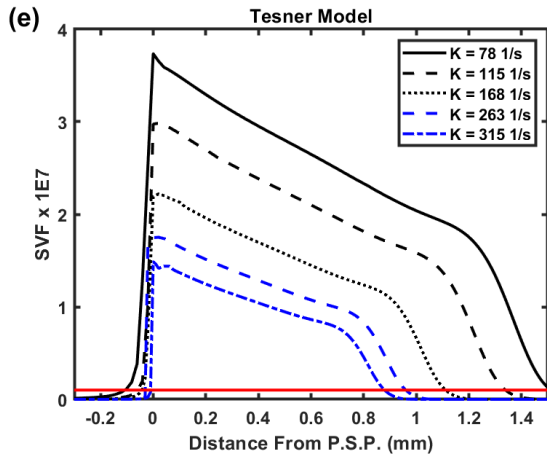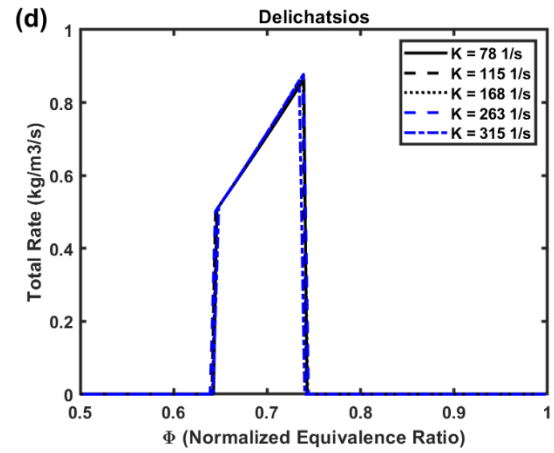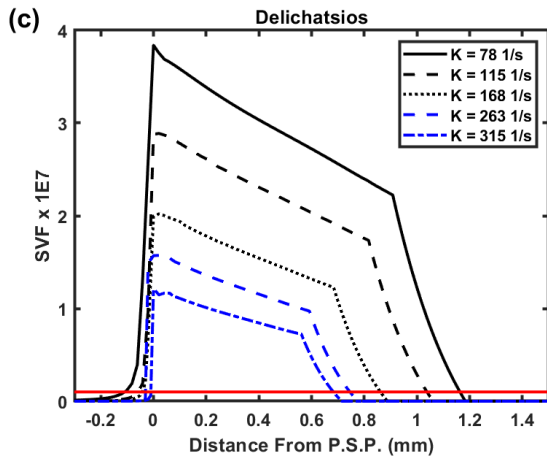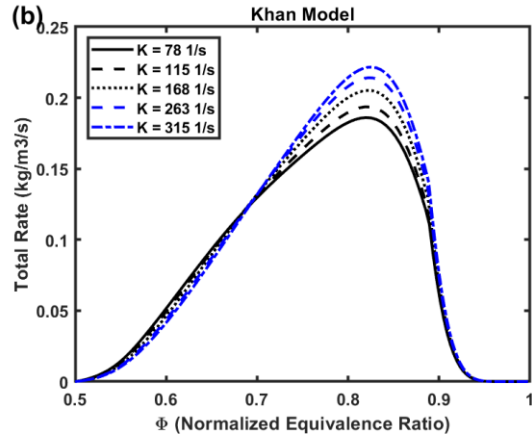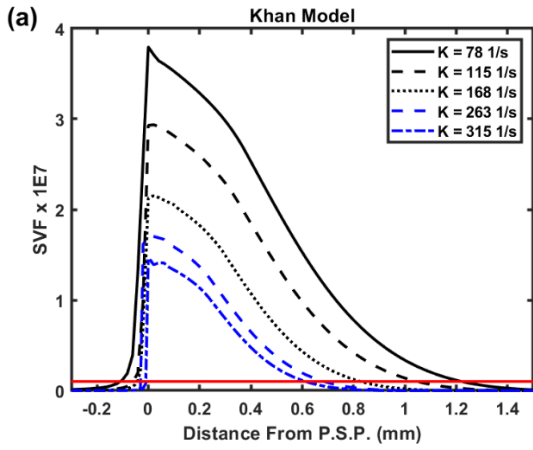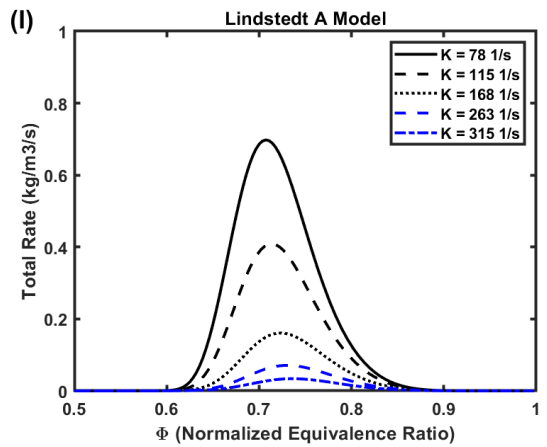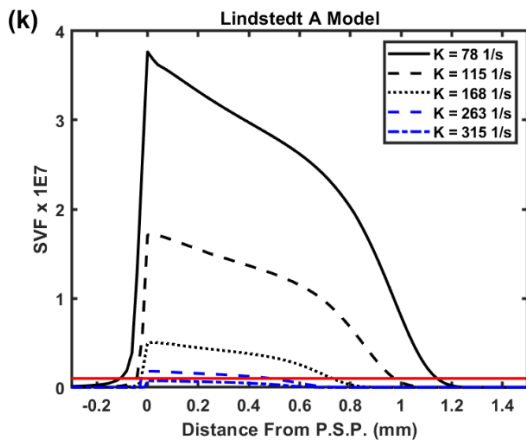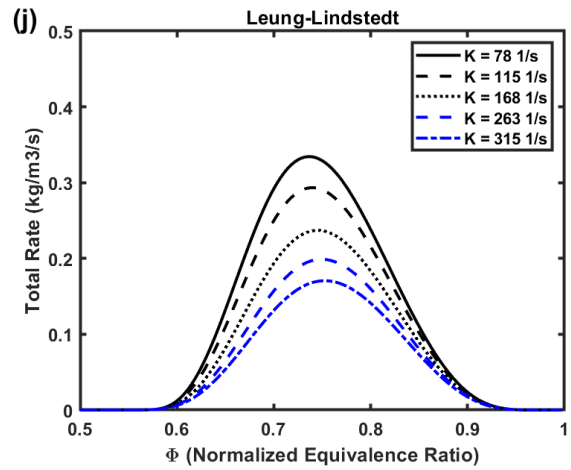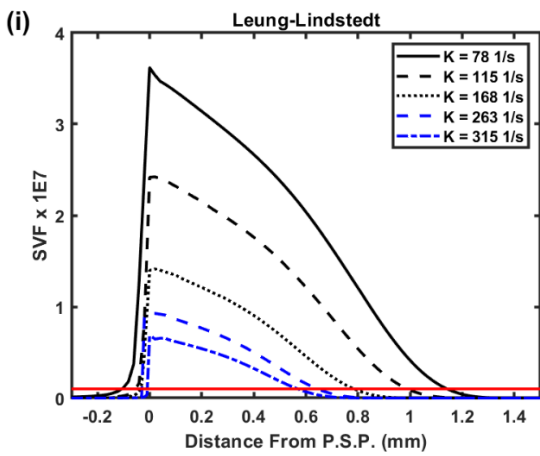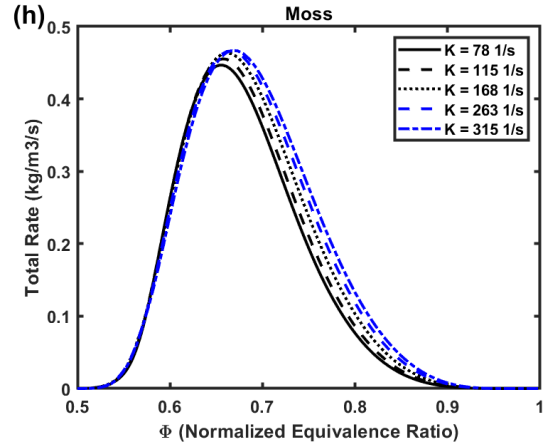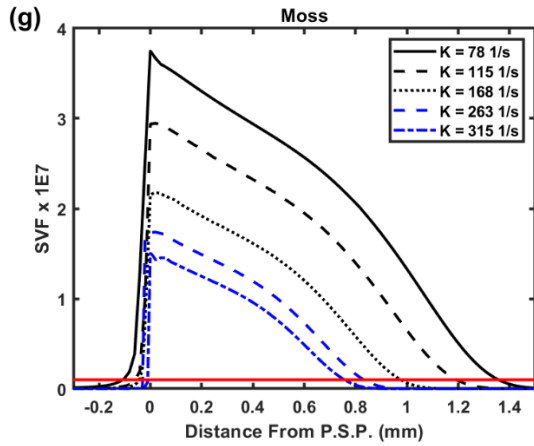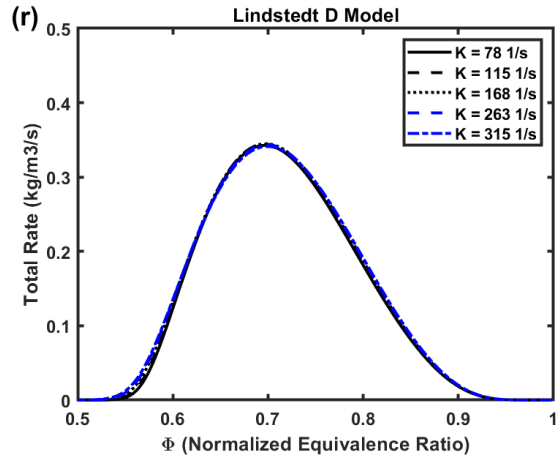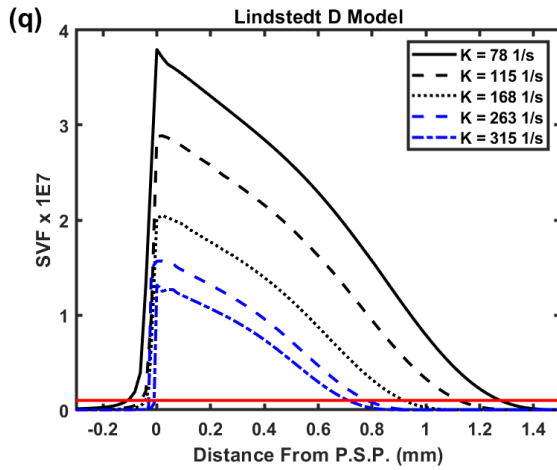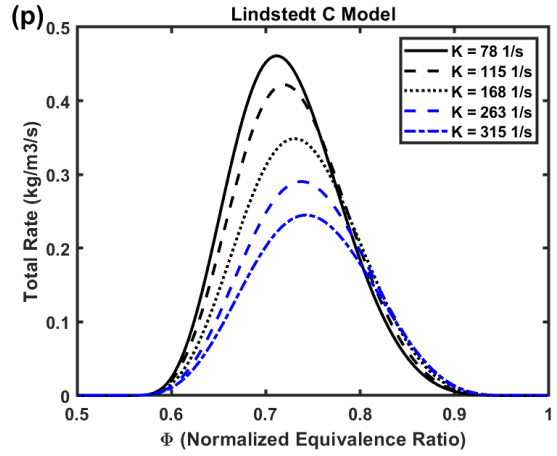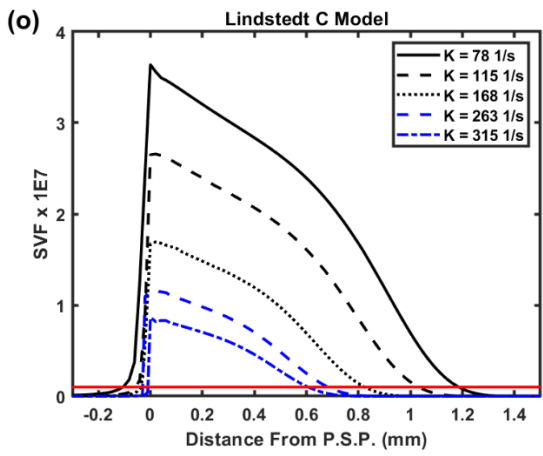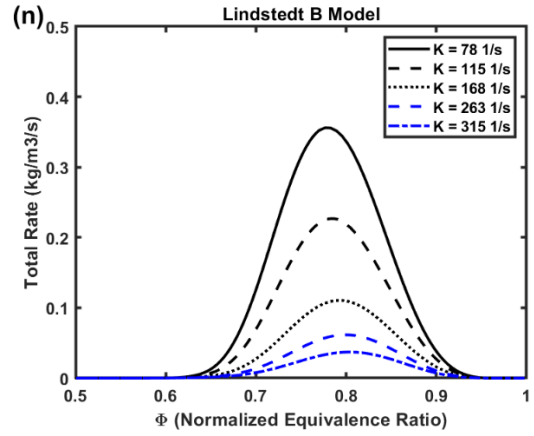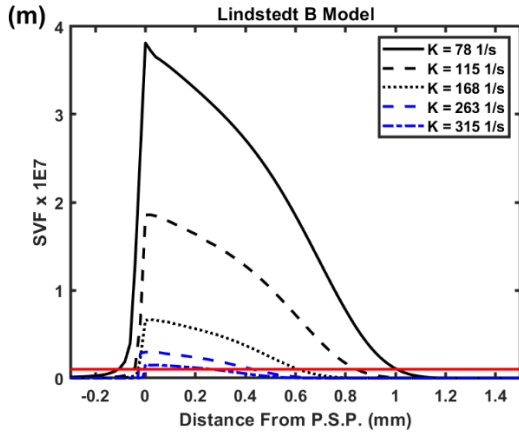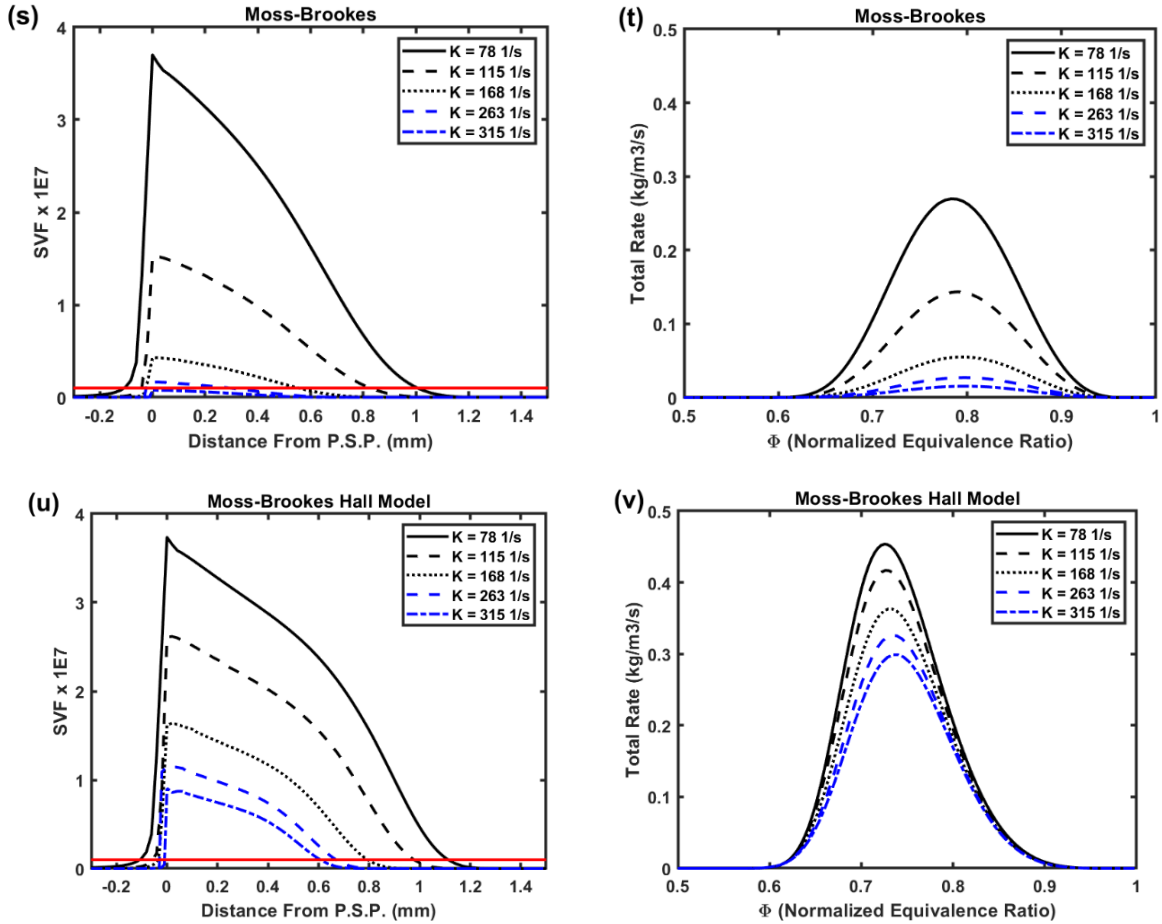
Figure 5-13. Results for all *K* in the changing *K* evaluation; a) Khan *svf* vs. distance from *psp*; b) Khan total formation rate vs. *Φ* c) Delichatsios *svf* vs. distance from *psp*; d) Delichatsios total formation rate vs. *Φ* e) Tesner *svf* vs. distance from *psp*; f) Tesner total formation rate vs. *Φ*. g) Moss *svf* vs. distance from *psp*; h) Moss total formation rate vs. *Φ* i) Leung-Lindstedt *svf* vs. distance from *psp*; j) Leung-Lindstedt total formation rate vs. *Φ*. k) Lindstedt a *svf* vs. distance from *psp*; l) Lindstedt a total formation rate vs. *Φ*; m) Lindstedt b *svf* vs. distance from *psp*; n) Lindstedt b total formation rate vs. *Φ*; o) Lindstedt c *svf* vs. distance from *psp*; p) Lindstedt c total formation rate vs. *Φ*; q) Lindstedt d *svf* vs. distance from *psp*; r) Lindstedt d total formation rate vs. *Φ*; s) Moss-Brookes *svf* vs. distance from *psp*; t) Moss-Brookes total formation rate vs. *Φ*. u) Moss-Brookes-Hall *svf* vs. distance from *psp*; v) Moss-Brookes-Hall total formation rate vs. *Φ*. Soot-free flame designated in blue. Diagnostic limit for *svf* shown in a) by red line.

5.3 Semi-Empirical Evaluation Conclusions

Semi-empirical models for soot formation were reviewed and applied to a series of non-premixed ethylene counterflow flames which span the experimental sooting-to-non-sooting transition by increasing Z_{st} and *K*. No model predicted a blue flame for increased Z_{st} and most

73

models predicted peak *svf* amounts of at least one order-of-magnitude higher than necessary to register a blue flame. Two models, (MB, La), predicted a blue flame for increased K. Many models showed an increase in peak *svf* even with a reduced integrated *svf* due to these changes in flame conditions. Some models erroneously predicted increased integrated *svf* with increased Z_{st}. A unique approach of plotting in normalized, local equivalence ratio was introduced to aid in the analysis of formation rate changes as flame conditions were modified.

An in-depth analysis was performed for each model. The varying results from two-step models were largely due to differences in the surface area dependent growth terms. All models treat soot formation as an irreversible process deriving from fuel pyrolysis and are not formulated to account for changes in flame structure and reversibilities that occur with increased Z_{st}. As such, they fail to predict soot suppression at higher Z_{st}.

Based on the results and analysis of both evaluations, the use of MB, La, and Lb is recommended for CFD simulations of highly-strained flames at low Z_{st}, with inclusion of normalization factors (Table 5-1). The KG model could also be considered for cases with elevated Z_{st} as it is one of the better performers and is sensitive to Z_{st} through the relationship between temperature and local equivalence ratio (ϕ). Many of the models evaluated are found to produce a soot formation profile that, when plotted in Φ-space, is consistent with experimental findings, and thus are well-positioned for further improvement by considering soot formation reversibilities that occur in elevated Z_{st} flames.

It is noted that all evaluated models were designed for low-Z_{st} and low-to-moderate K environments. Their authors did not propose their use in such challenging and unique environments. Nevertheless, it has been demonstrated that there remains a significant need for a

computationally-efficient model which can capture variations in soot production due to increases in Z_{st} and K, which may vary significantly in many industrial applications.

5.4 Detailed Model Results

In addition to evaluating semi-empirical soot models, results from the detailed soot mechanism of KM2 and ABF were also investigated. The methodology used to obtain these results follows that for the semi-empirical models above, with the exception that the detailed modeling results did not require a post-processing code, but were taken directly from the Chemkin solution (which includes a solid-phase mechanism in addition to the gas-phase combustion mechanism). These models were not modified or normalized for this evaluation, as these models rely upon detailed chemistry and are expected to be more robust than a semi-empirical model.

Predictions for KM2 are show in Fig. 5-14. The *svf* profiles, shown in Fig. 5-14a, appear comparable to some of the semi-empirical models above (e.g. LL), where the overall soot production decreases but the peak *svf* steadily increases along with Z_{st} due to feedback effects. A notable difference is that for $Z_{st} = 0.074$, the peak *svf* is over a factor of two lower than expected from the reference measurement of Wang. Before analyzing the reaction pathways, it is helpful to recall the overall soot mechanism for KM2 from Section 2 above.

The inception rate (Eq. 2-35) is plotted in Fig. 5-14b and rapidly decreases as Z_{st} increases. The inception rate peaks at higher Phi for $Z_{st} = 0.074$ because aromatic species are not completely destroyed but are convected to the *psp* (compare the location of A_1 in Fig. 5-12). Despite these trends, the closed sites produced by this model (Fig. 5-14c) are initially consistent for all Z_{st}, stopping only at the *psp* for each respective flame. The open site concentration (Fig. 5-14d) mirrors the earlier production of closed sites (but at a smaller magnitude), but are only available closer to the flame, where there is an abundance of H^+ radicals to create them from existing closed sites .

75

Finally, the total soot formation rate (Fig. 5-14e) is almost complete driven by surface reactions. The importance of HACA to the total formation rate as evidenced by the similarity in profile shapes between Figs. 5-14d-e. Collectively, the mechanism shows a strong reduction in inception (as PAHs are strongly diminished) as Z_{st} increases. However, the creation of reaction sites and therefore surface growth reactions are somewhat sustained and are only slightly decreased as Z_{st} increases. This leads to minor reductions in overall soot production and (as with the semi-empirical models above), an increased peak *svf* across these flames. While this model is no-less-worse than other semi-empirical models above, it does not show significant improvement in predictions of *svf*.
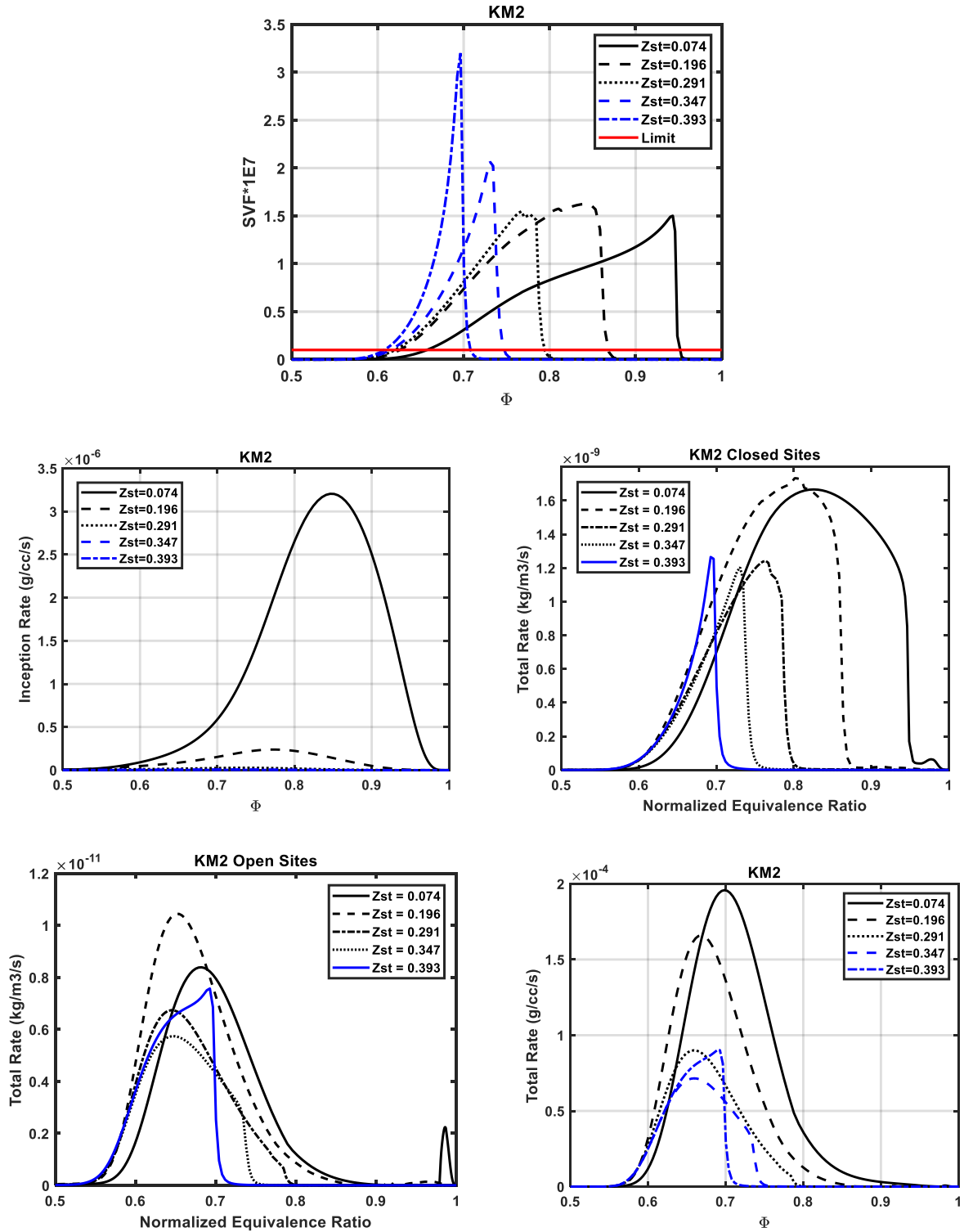
Figure 5-14. KM2 predictions of soot vs Φ.. A) *svf* , b) inception rate, c) closed site concentration, d) open site concentration, e) total formation rate

In contrast, the ABF model predicts *svf* profile (Fig. 5-15a) where very little soot is created until the *psp* is reached, at which the *svf* increases rapidly. While the inception rate for ABF (Fig. 5-15b) is somewhat similar to that of KM2, there is a defining difference in the mechanism, shown in Eqs. 2-31. Open sites are directly created from inception, being thus continually created and transported with soot particles towards the *psp*, where they stack up (compare Figs. 5-15c , 5-15b). Since surface growth will occur where this are open sites, the total formation rate (Fig. 5-15d) and the *svf* profile are all similarly shaped in a manner unlike that of experimentally measured soot profiles. Further, the peak for $Z_{st} = 0.074$ is a factor of three too small. Thus, while this model does predict a blue flame for $Z_{st} = 0.393$, it also predicts blue flames for $Z_{st} = 0.196$, 0.291, and 0.347. This model therefore cannot be recommended for use in these types of flames.
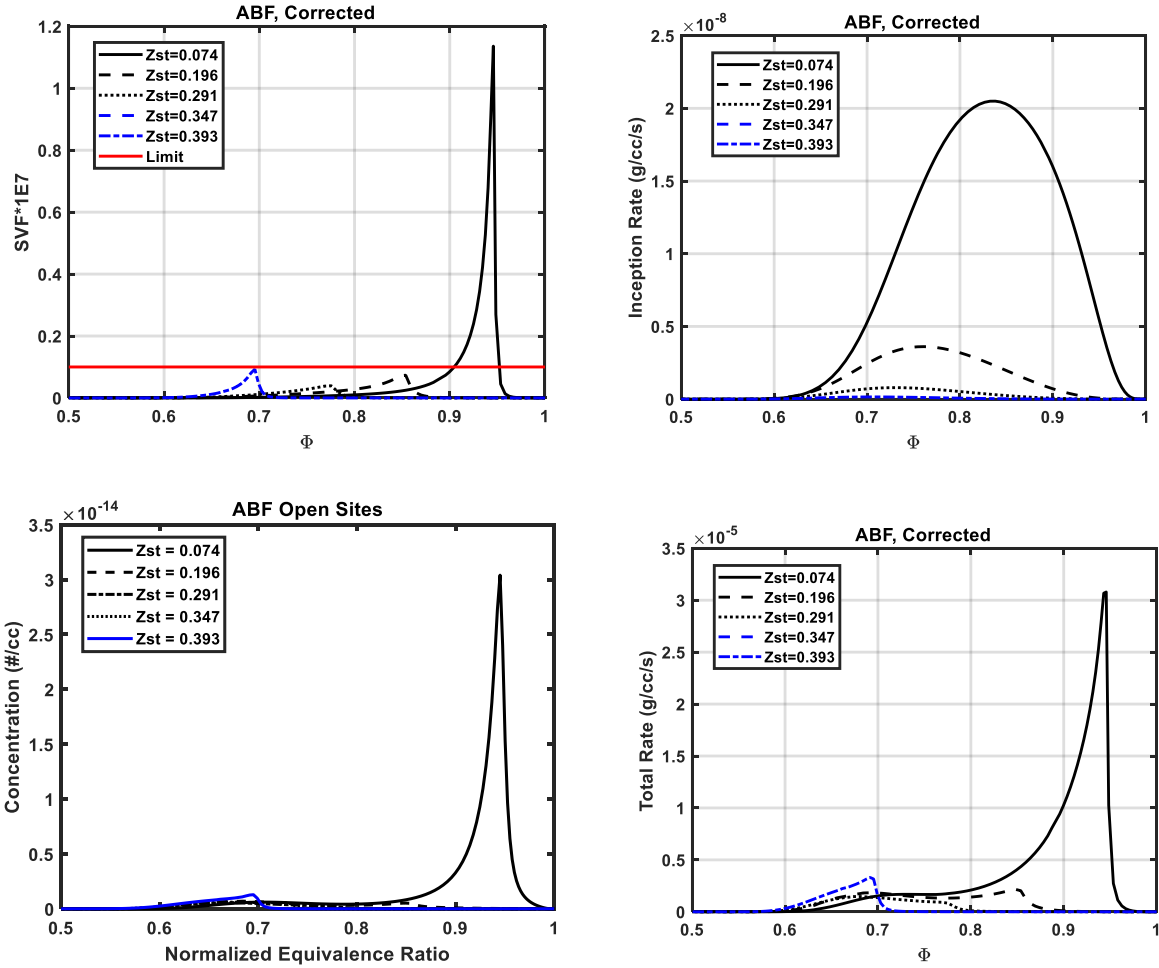
Figure 5-15. KM2 predictions of soot vs. *Φ*. A) *svf* , b) inception rate, c) closed site concentration, d) open site concentration, e) total formation rate.

5.5 Overall conclusions

For both semi-empirical and detailed models, soot formation is thought of fundamentally as irreversible pyrolysis-type process where sufficient fuel and temperature will produce soot. There are no mechanisms to counteract, reverse, or suppress soot inception or the later growth steps. Some models could be criticized for their relationships between surface growth and inception (level of feedback through a surface area term or through open site concentration), but this issue appears to be secondary to controlling for the reduction and elimination of soot inception. The model correctives introduced in the next chapter will examine this hypothesis.

Chapter 6: New Models

6.1 Detailed Chemistry and Soot Reversibility

The goal of the semi-empirical model formulations produced in this work is to capture important chemical phenomena during soot formation in the most concise and accurate manner as possible. It is helpful, then to recall important chemical pathways which are relevant in the flame environments of interest. Soot formation is often thought to proceed everywhere on the fuel-side of the non-premixed flame, until the pool of oxidative species (e.g. O_2, OH) is reached, as evidenced by the formulation of existing semi-empirical models. However, other processes counteract soot formation which occur in all flames and become more pronounced, even critical, at elevated Z_{st}. Previous studies have indicated that soot stops forming prior to reaching the location of oxidizing species, due to various reversibilities in the soot formation process. Temperature is a potential source of soot reversibility due to the exothermic nature of the C_2H_2-to-A1 pathway [9]. Temperataure can also play a role in PAH fragmentation [9]. Elvati and Violi [20] have shown that PAH dimers are thermodynamically unstable at high temperatures. Accounting for reversibility in aromatic condensation has also been shown to be important for predicting particle morphology [24].

As alluded to in Section 3.3, further analysis is not made into the role of reversible chemical pathways related to aromatics species. These results can be observed in Fig. 6-1, which shows the pathways of A_1 formation for $Z_{st} = 0.074$ (Fig. 6-1a) and for the soot inception limit flame ($Z_{st} = 0.393$, Fig. 6-1b). While Eq. 6-1 is still larger than Eq. 6-2 in terms of peak and integrated rate, these metrics mask the local importance of each reaction. In the region where Eq. 6-2 has reversed

80

$(0.6 < \Phi < 0.7)$, it is counteracting Eq. 6-1. Moving from the fuel inlet to the flame (right to left in Fig. 6-1), the main contribution to A_1 generation is initially due to Eq. 6-2, then a mix of Eqs. 6-1,6-2, then Eq. 6-1, and finally the net reaction flips and A_1 is destroyed due to a combination of Eq. 5, oxidation from OH, and other contributions. Note that in the location where Eq. 6-1 peaks, the net A_1 ROP is actually negative due to the factors of reversibility and oxidation. The overall result of these effects is that the net A_1 ROP more closely follows Eq. 6-2 in its profile shape and reverses in the high temperature zone. For $Z_{st} = 0.393$, these features are similar with the notable observation that all rates are reduced. Fig. 6-1c shows the A_1 ROP comparison for these two flames. For $Z_{st} = 0.074$, the reversal happens around $\Phi = 0.68$ and for $Z_{st} = 0.393$, $\Phi = 0.65$. Given that Eq. 3-3 reverses with the H^+ pool, these arguments further promote the overall argument of Skeen et al., that H^+ is an important contributor in the reversal of soot-promoting pathways. The novelty of these observations is the emphasis on the *locality* ($\Phi \sim 0.65$) at which this occurs for all Z_{st} rather than on the qualitative reverses which happens as Z_{st} is increased.
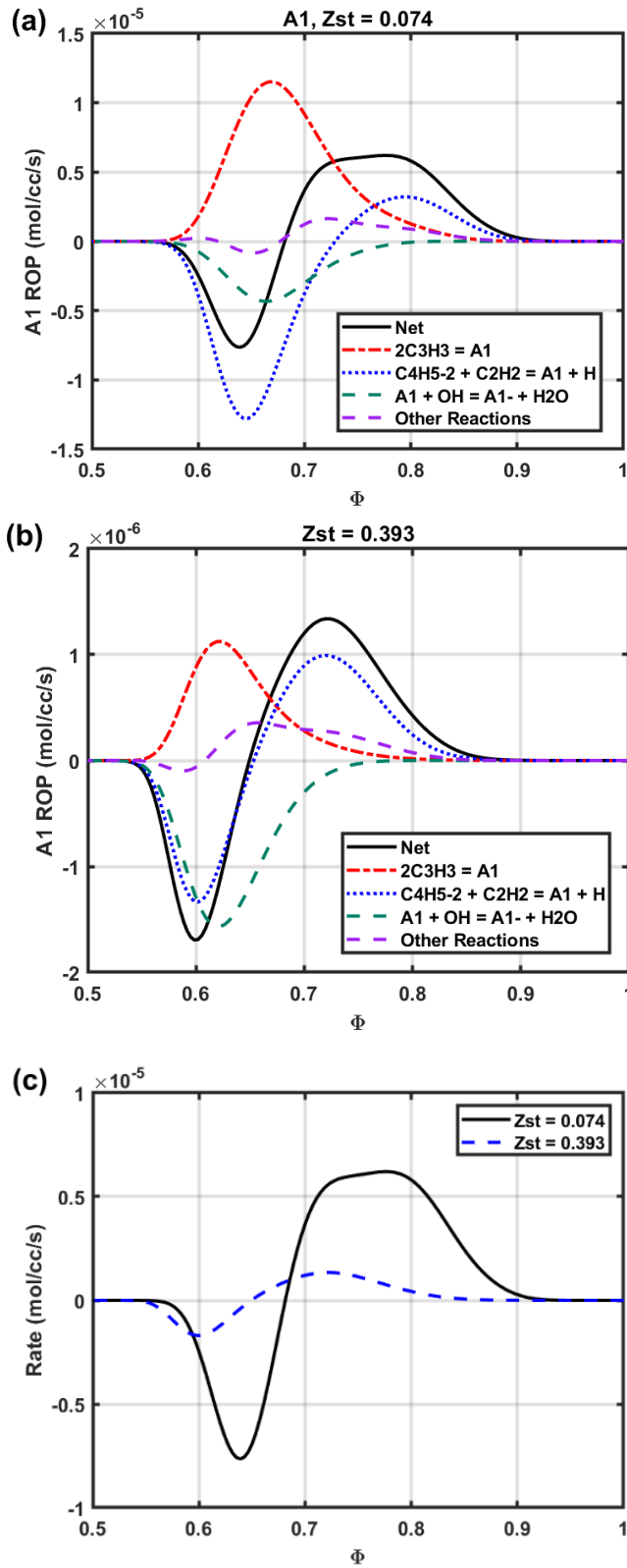
Figure 6-1. A₁ Rate of Production vs Φ. a) Various pathways for $Z_{st} = 0.074$, b) Various pathways for $Z_{st} = 0.074$, c) comparison of net A₁ ROP against $Z_{st} = 0.074$ and 0.393.

Skeen et al. also hypothesized that these behaviors would be observed for other soot-precursor-growth reactions where H^+ is generated as a product, e.g. there would be a reduction in PAH growth due to this set of reactions. To investigate this claim, an analysis was performed on all carbon addition reactions from A_1 up to A_7 in the KM2 mechanism. Examples of these types of reactions involving acetylene are shown in Eqs. 6-3 – 6-5 below.

$$A_1^- + C_2H_2 \leftrightarrow A_1C_2H + H \tag{6-3}$$

$$A_2 - 1 + C_2H_2 \leftrightarrow A_2C_2H_2 \tag{6-4}$$

$$A_2C_2HA^* + C_2H_2 \rightarrow A_3 - 4 \tag{6-5}$$

Other important carbon-addition reactions, many of which are reversible, are listed in Section 6.7 - Supplemental Material. These carbon-reactions are summed together and plotted in Fig. 6-2a, for both low-and high-Z_{st} flames. The various carbon-adding reactions are grouped according to their by-products: reactions with no by-product (Eq. 6-5), reactions with a by-product of H^+ (Eq. 6-3), and reactions with a by-product of H_2 (Eq. 6-4). These three reaction groupings are plotted separately for $Z_{st} = 0.074$ in Fig. 4b,. A complete list of reactions used is included in Section 6.7 - Supplemental Material. For the flame condition of $Z_{st} = 0.74$, at the location near $\Phi = 0.65$ there is a reversal in the net chemical rate where the reactions are no longer favorable for carbon addition; rather, reverse reactions are promoted which remove attached carbon species. For the soot inception limit flame ($Z_{st} = 0.393$), the transition occurs closer to $\Phi = 0.60$ but the trend is similar (notably, the positive quantity of carbon addition is also reduced due the diminished formation of precursors, e.g. A_1 as noted by Skeen et al.). Fig. 6-2b indicates that while there are multiple reaction types which contribute to net carbon addition, the reversal effect is solely due to

83

reactions where a by-product of H^+ is produced. This result is consistent with the H^+-based reversal of Eqs. 3-2 – 3-3 above and collectively, these reactions demonstrate that H^+-based reversals occur at all levels of soot formation (C_3H_3 formation, aromatic creation, PAH growth) and that the reversibility of soot formation occurs in the region of $0.60 < \Phi < 0.70$.
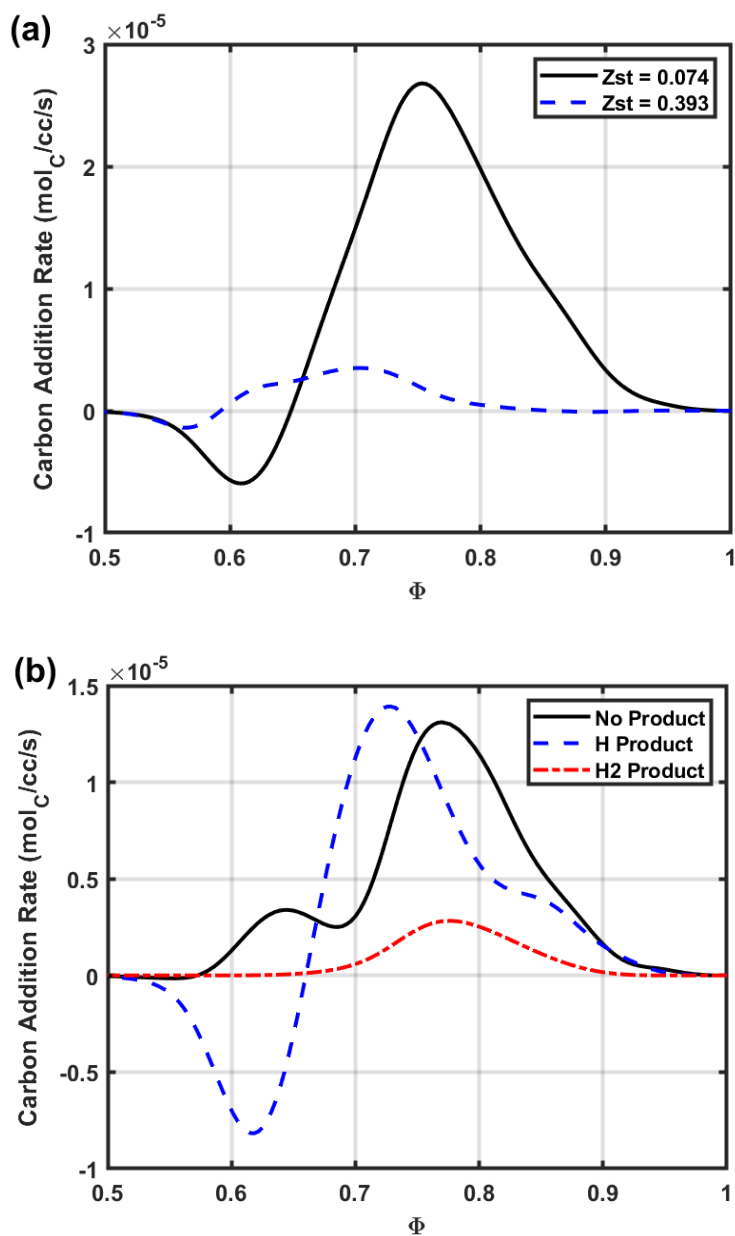
Figure 6-2. Analysis of carbon-addition pathways from A1 to A7 for the KM2 mechanism. a) All reactions summed for $Z_{st} = 0.074$ and $Z_{st} = 0.393$. b) Reactions grouped and summed according to reaction by-product for $Z_{st} = 0.074$.

These results are consistent with the findings of Kumfer, et al. concerning an observed high-temperature boundary of the soot-formation zone away from flame front where soot could no longer form. In that work, this location can be characterized by a critical local equivalence C/O ratio [46] for several different aliphatic fuels in a non-premixed coflow flame. For ethylene, C/O)$_{cr}$ was determined to be 0.53 [46], which is relatively far from the location of stoichiometry (C/O = 0.33). By converting the various C/O ratios to Φ, this boundary can be spoken of more generally. As seen in Table 6-1, the critical value(s) take a very narrow range (0.63-0.66) upon conversion from C/O to Φ, as the latter is general for all fuel species. Beyond this location the local gas composition and/or temperature are not favorable for soot inception. It is now hypothesized that there is a balance in the formation and reversing processes at this location such that there is no net soot formation beyond this location for all flame conditions. As Z_{st} increases, the soot formation zone shrinks in size until the location of initial soot formation coincides with this critical location [3].

Fuel	Measured critical C/O [54]	Stoichiometric C/O	ϕ_{cr}	Φ_{cr}
CH$_4$	0.42	0.25	1.68	0.63
C$_2$H$_6$	0.54	0.29	1.89	0.65
C$_3$H$_8$	0.58	0.30	1.93	0.66
C$_2$H$_4$	0.60	0.33	1.80	0.64
C$_2$H$_2$	0.71	0.40	1.78	0.64

Table 6-1. Critical C/O values below which no soot can form as measured by Kumfer, followed by the C/O of stoichiometry for each fuel, and the critical values converted to ϕ and Φ.

Given the observed importance of these reversible reactions and the role that hydrogen plays in this process, it would be beneficial to capture these features in a semi-empirical soot model. As with previous work, the target will be semi-empirical models due to an application focus and desire to capture important chemical details in a simple manner. The latter point is non-trivial as the

ability to concisely describe physical phenomenon coincides with elucidating important features. In brief, then, a new reversibility term is proposed for use in semi-empirical soot modeling. Because hydrogen radical modeling would require an extensive mechanism, instead a temperature-based reversibility term is added which serves as a proxy for a H^+-based reactions that counteract soot formation. This analogy is shown in Eq. 6-6 below.

$$\omega_{rev} = k_{rev} \exp\left(-\frac{T_{A,rev}}{T}\right) \sim k_{H^+}[H^+] \tag{6-6}$$

High temperature can be a good indicator of the location of H^+ radicals, as seen in Fig. 6-3 where the peak of H+ is located somewhat close to the flame (but on the fuel side) and quickly declines as temperature drops. An additional reason for basing the reversibility term below (Eq. 6-42) on temperature is the various temperature-based reversibilities hindering soot inception described above. Capturing these features, while less critical for traditional fuel-air flames, is essential for high-Z_{st} environments where these processes can suppress and even inhibit soot formation.
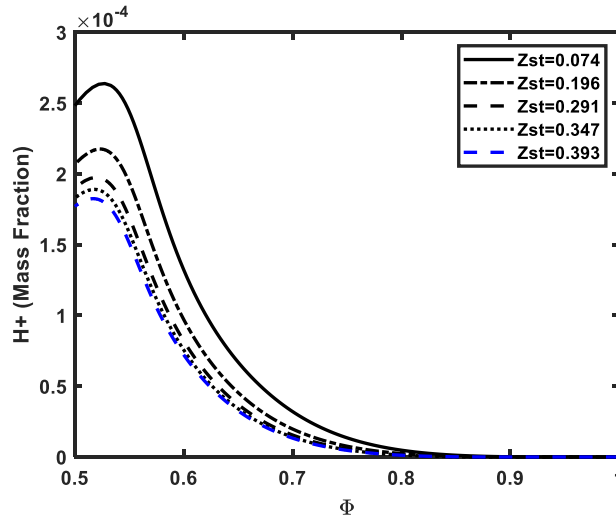
Figure 6-3. Hydrogen radical fraction vs. Φ as predicted by KM2 for various Z_{st}.

6.2 Initial One-Step Model

The development of this model begins with the classic consideration the need for sufficient fuel, temperature, and time needed to create a nascent soot particle from a parent fuel. Detailed chemistry is avoided, leaving the option of using fuel fraction (total hydrocarbon count) or acetylene as a soot precursor. It was noted above in the semi-empirical evaluation that soot formation is essentially a pyrolysis-driven process. The fault of the models at high Zst was not due to an incorrect understanding of this feature, but rather because these models did not account for other processes which become important under these flame conditions. It is now argued that the choice between fuel fraction and acetylene is one of increased accuracy and detail, but which does not fundamentally alter the model. Accordingly, the early stages of model development used a fuel-based Arrhenius term.

$$\omega_s = Y_F \exp\left(-\frac{T}{T_{Arr}}\right) \tag{6-7}$$

While this formulation satisfies the dependence of soot on fuel and temperature, the need for sufficient time is not accounted for. Comparing to a detailed model can be insightful here. By modeling each step of the soot process (see Eq. 6-8), each kinetic barrier will be accounted for and the finite time needed for soot to form will be manifest in the model. In contrast, by assuming that soot can form directly from fuel (Eq. 6-9), a series of kinetic bottlenecks are bypassed. To account for this discrepancy, a term is added to the model (τ in Eq. 6-10) to explicitly account for the available reaction time. In a sense, the addition of this variable modifies the fuel fraction in a way that together "τY_F" is a transformed species that better approximates soot precursors.

$$Fuel \rightarrow C_2H_2 \rightarrow A_i \rightarrow PAH \rightarrow n \tag{6-8}$$

$$Fuel \rightarrow n \tag{6-9}$$
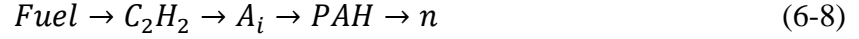
$$\omega_s = \tau Y_F \exp\left(-\frac{T}{T_{Arr}}\right) \tag{6-10}$$

The appropriate time quantity chosen for this model could vary depending on the flame type / application. For example, scalar dissipation could be considered for coflow flames. For use in counterflow flames, the inverse of the strain rate ($1/K$) is an appropriate measure of the available reaction time in the system.

Next, the soot model must account for the various reversibilities discussed above. The initial way this process was modeling was by stating that soot formation would be cut-off at a critical value of Φ. This is not unlike the approach of Delichatsios above, where soot formation was not allowed below a critical C/O value. (Recall, that the above criticism of that model centered around the low-temperature boundary, not the C/O boundary). A way to naturally shut down soot formation (rather than abruptly) is seen in the additional Φ-based term in Eq. 6-11:

$$\omega_s = kY_F \frac{(\Phi - \Phi_{crit})^n}{K^m} \exp\left(-\frac{T}{T_{Arr}}\right) \tag{6-11}$$

A rate constant (k) and two fitting constants (m, n) have also been included in the above equation to account for the fact that these terms have an empirical element to them.

Optimization of the model was performed using a grid search within certain bounds which are listed in Table 6-2 below. The bounds were the same for all runs, except for a special case where Φ_{crit} was restricted, resulting in Case 2. Results from Case 1 (full optimization) are shown in Fig. 6-4. From the *svf* profiles (Fig. 6-4a), it can be seen that this model is able to predict a blue

flame. The formation rate (Fig. 6-4b) rapidly decreases as Z_{st} increases. However, Φ_{crit} is too large, maxing out at the upper bound of the optimization range. The result is a formation rate profile that is shifted too close to the fuel inlet and is not a physically realizable result.

Variable Name	Lower Bound	Upper Bound	Case 1	Case 2
m	0	5	3	0.5
n	0	3	2.5	4
Φ_{crit}	0.55	0.75	0.75	--
Φ_{crit}	0.55	0.65	--	0.55
$T_{Arr}(1000 \text{ K})$	12	24	16	20
k	--	--	2.79E13	3E9

Table 6-2. Optimization bounds of fitting constants and values as determined by optimization procedure to minimize peak *svf* for $Z_{st} = 0.393$.
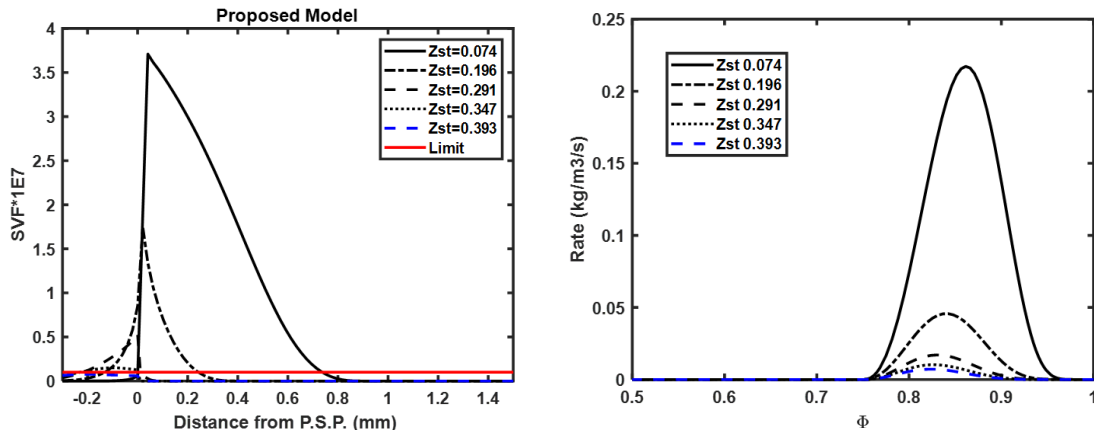
Figure 6-4. Results from full-range optimization of model in Eq. 6-11 for the Z_{st} evaluation flames, a) *svf* vs. distance from the *psp*, b) soot formation rate vs. Φ.

An attempted was made to remedy the profiles location in Φ space by lowering the cap on Φ_{crit}. However, making this adjustment prevented the model from predicting a blue flame. The results of the optimized parameters which yielded the lowest peak *svf* for $Z_{st} = 0.393$ are shown in

Fig. 6-5a. While there is a steady reduction in peak *svf* as Z_{st} increases (unlike most existing models evaluated above). As a result, this model formulation shows a mixed result: by utilizing Φ_{crit} as a cut-off, soot formation reductions can be correctly predicted; however, the fitting parameters and formation rate profile do no correlate to expected characteristics of soot formation. In conclusion, this model framework will be modified to capture the essential features while resulting in a phenomenologically-insightful model.
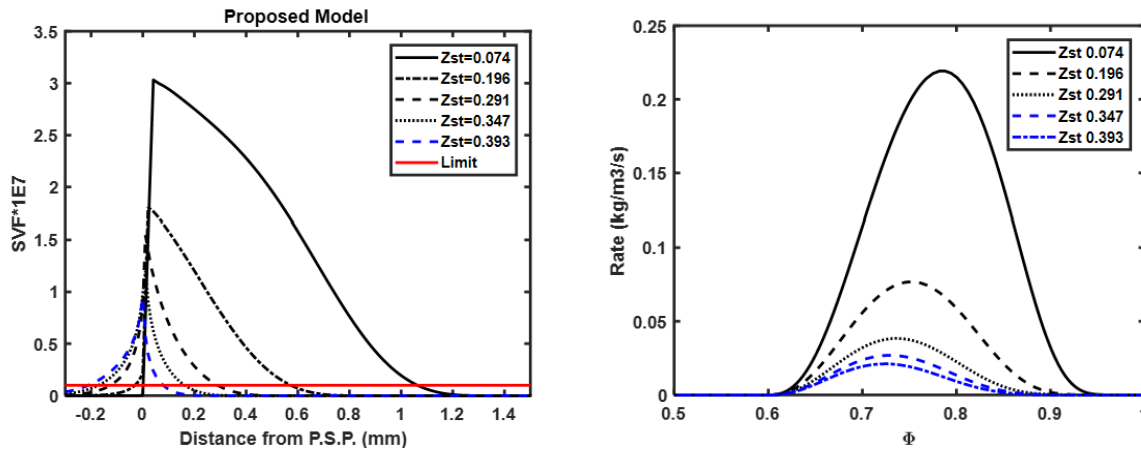
Figure 6-5. Results from constrained optimization of model in Eq. 6-11 for the Z_{st} evaluation flames, a) *svf* vs. distance from the *psp*, b) soot formation rate vs. Φ.

6.3 Kinetic-Phenomenological Derivations

To address this question and to place this early model on a firmer theoretical foundation, a series of phenomenological kinetic derivations were made in an inquiry into possible dependencies soot formation might have on a local equivalence ratio. These exercises are performed at a high level; for example, both fuel and oxygen species use a lumped quantity (O_2, OH, or even CO_2 can attack soot). These methods keep the chemistry simple and are also necessary to show any dependency on ϕ or Φ. The derivations begin with the simplest models of soot formation and

follow with progressively more complex models. None reach the level of chemistry found in detailed soot models.

Scheme 1

This is the simplest of models. Soot forms directly from fuel and oxygen attacks fuel and soot. This model is not informative, but serves as a foundation and contrast to other models.

$$F \rightarrow S \qquad\qquad\qquad F + O_{lumped} \rightarrow P$$

$$S + O_{luumped} \rightarrow P$$
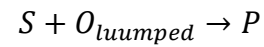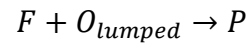
$$\frac{dS}{dt} = k_1[F] - k_3[S][O] \qquad\qquad (6\text{-}12)$$

Scheme 2

Soot is still formed directly from the fuel species. However, there are now separate inception and surface growth routes and both of these are reversible. Still, this model is not particularly insightful as these terms are all standalone.

$$F \leftrightarrow S \qquad\qquad\qquad F + O_{lumped} \rightarrow P$$

$$S + F \leftrightarrow S \qquad\qquad\qquad S + O_{luumped} \rightarrow P$$
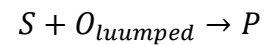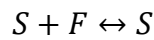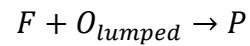
$$\frac{dS}{dt} = k_{1f}[F] - k_{1b}[S] + k_{2f}[S][F] - k_4[S][O] \qquad\qquad (6\text{-}13)$$

Scheme 3

Here, an intermediate is introduced through a reversible reaction. This variable is a precursor to soot, which is created through an irreversible reaction, and also the growth species. Without further assumptions, this model will look similar to Scheme 2, but with species [I] replaced [F] in Eq. 6-13 For the sake of exploration, the steady-steady assumption will be evoked for I, with the result shown in Eq. 6-14 and reformatted in Eq. 6-15. Interestingly, soot formation is now a function of a formation term which is driven by fuel availability and divided by the sum of processes which counteract soot formation. There is also an oxidation attack on soot.

$$F \leftrightarrow I \qquad\qquad\qquad F + O_{lumped} \rightarrow P$$

$$I \rightarrow S \qquad\qquad\qquad I + O_{lumped} \rightarrow P$$

$$S + I \rightarrow S \qquad\qquad\qquad S + O_{luumped} \rightarrow P$$

$$\frac{dS}{dt} = \frac{(k_2 + k_3[S])k_{1f}[F]}{k_{1b} + k_2 + k_3[S] + k_5[O]} - k_6[S][O] \tag{6-14}$$

$$\frac{dS}{dt} = \frac{K_{1eq}[F]}{\frac{1}{k_2 + k_3[S]} + \frac{1}{k_{1b}} + \frac{k_5[O]}{k_{1b}(k_2 + k_3[S])}} - k_6[S][O] \tag{6-15}$$

If this latter oxidation term is negligible (away from the flame front), then soot formation can be further simplified depending on which kinetic regime the model is in. When soot formation and growth are dominant over the intermediate reversibility, then soot formation is only a function of the fuel concentration and the forward rate of its pyrolysis (Eq. 6-16). When the reversibility of the first step is negative (Eq. 6-17), soot formation goes like the availability of fuel, the equilibrium constant of reaction 1, and is separately dependent on inception and surface growth. When oxidation scavenging of the intermediate is much greater than the routes of soot formation or reversibility back into fuel (Eq. 6-18), then soot formation is a function of fuel divided by the

lumped oxygen quantity. This fraction is the definition of the local equivalence ratio, shown in the second formulation of Eq. 6-18.

If $k_2 + k_3[S] \gg k_{1b}$

$$\frac{dS}{dt} = k_{1f}[F] \tag{6-16}$$

If $k_{1b} \gg k_2 + k_3[S]$

$$\frac{dS}{dt} = K_{1eq}(k_2[F] + k_3[S][F]) \tag{6-17}$$

If $(k_5 O \gg k_{1b}$ and $k_5 O \gg k_2 + k_3[S])$

$$\frac{dS}{dt} = (k_2 + k_3[S])\frac{k_{1f}}{k_5}\frac{[F]}{[O_{lumped}]} = (k_2 + k_3[S])\frac{k_{1f}}{k_5}\phi \tag{6-18}$$

While this formula achieves the intended aim of demonstrating a dependency of soot formation on ϕ, it does so by making a series of questionable assumptions regarding the SSA of [I] and the assumption about oxygen scavenging being dominant. In the derivations which follow, more chemical details were included in the hopes that addition chemistry would strengthen the above result.

Scheme 3b

A derivation similar to Scheme 3 can take place but with pyrolysis step (F -> I) occurring irreversibly from fuel and the inception step being reversible. These changes are more representative of soot precursor chemistry.

$$F \rightarrow I$$

$$I \leftrightarrow S$$

$$S + I \rightarrow S$$

$$F + O_{lumped} \rightarrow P$$

$$I + O_{lumped} \rightarrow P$$

$$S + O_{luumped} \rightarrow P$$
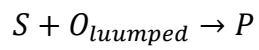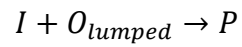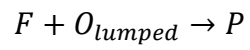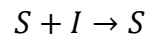
Overall Equation:

$$\frac{dS}{dt} = \frac{dS}{dt}\Big|_{formation} - \frac{dS}{dt}\Big|_{reversibility} - \frac{dS}{dt}\Big|_{oxidation} \qquad (6\text{-}19)$$

$$\frac{dI}{dt} = k_1[F] - k_{2f}[I] + k_{2b}[S] - k_3[S][I] - k_5[O_l][I] = 0 \qquad (6\text{-}20)$$

$$\frac{dS}{dt}\Big|_{form} = \frac{(k_2+k_3[S])k_{1f}[F]}{k_2+k_3[S]-k_{2b}S+k_5[O]} \qquad (6\text{-}21)$$

The results will be similar to Scheme 3, except with $-k_{2b}S$ in place of k_{1b} in Eq. 6-15.

Scheme 4

Fuel pyrolizes to an intermediate, *I*, which is like an aromatic for this scheme. It is a large precursor, since it is formed reversibly from fuel, shedding H, but does not shed any *H* when it forms soot (something comparable to an aromatic). Soot also grows from *I*. Lumped oxygenated species will attack *C-H* species. The analysis now keeps the formation, reversibility, and oxidation terms separate. By evoking the SSA again for *I*, formation (Eq. 6-24) is driven by F and reversibility (Eq. 6-25) by existing soot, although the terms are still quite involved.

$$F \leftrightarrow I + H \qquad\qquad\qquad F + O_{lumped} \to P$$

$$I \leftrightarrow S \qquad\qquad\qquad\qquad I + O_{lumped} \to P$$

$$S + I \to S \qquad\qquad\qquad\qquad H + O_{lumped} \to P$$

$$S + O_{lumped} \to P$$

$$\frac{dS}{dt} = \frac{dS}{dt}\Big|_{formation} - \frac{dS}{dt}\Big|_{reversibility} - \frac{dS}{dt}\Big|_{oxidation} \tag{6-22}$$

$$\frac{dS}{dt}\Big|_{oxidation} = k_7[S][O] \tag{6-23}$$

$$\frac{dS}{dt}\Big|_{formation} = \frac{(k_2 + k_{3f}[S])}{k_{1b}[H] + k_{2f} + k_{3f}[S] + k_5O} k_{1f}[F] \tag{6-24}$$

$$\frac{dS}{dt}\Big|_{reversibility} = \left(1 - \frac{k_2 + k_{3f}[S]}{k_{1b}[H] + k_{2f} + k_{3f}[S] + k_5O}\right) k_{2b}[S] \tag{6-25}$$

If SSA is evoke for both *I* & *H* then the reactions (Eqs. 6-26, 6-27) are still quite complex. This derivation was not ultimately fruitful in its own right, but facilitated a more enlightening example below.

$$\frac{dS}{dt}\bigg|_{formation} = \frac{(k_2 + k_{3f}[S])k_{1f}[F])}{\frac{k_{1b}k_{1f}[F]}{k_{1b}[I] + k_6[O]} + k_{2f} + k_{3f}[S] + k_5O} \tag{6-26}$$

$$\frac{dS}{dt}\bigg|_{reversibility} = \left(1 + \frac{k_2 + k_{3f}[S]}{\frac{k_{1b}k_{1f}[F]}{k_{1b}[I] + k_6[O]} + k_{2f} + k_{3f}[S] + k_5O}\right)k_{2b}[S] \tag{6-27}$$

Scheme 5

In this scheme, I is more like acetylene. It is formed irreversibly and *does* shed H when it forms soot, as if it still had aromatic growth to do and thus had to lower the C/H ratio. If SSA is evoked for H, the result is seen in Eq. 6-28. If SSA is evoked for both I & H, the result is Eq. 6-29. The latter two terms in Eq. 6-30 are higher order terms and can be assumed to be smaller than the first two terms. This simplification leads to the result of Eq. 6-31.

$$F \rightarrow I + H \qquad\qquad\qquad F + O_{lumped} \rightarrow P$$

$$I \leftrightarrow S_\alpha + H \qquad\qquad\qquad I + O_{lumped} \rightarrow P$$

$$S_\alpha + I \rightarrow S_\beta \qquad\qquad\qquad H + O_{lumped} \rightarrow P$$
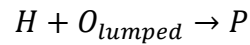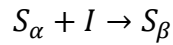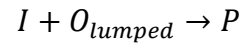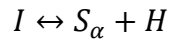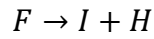
$$\frac{dS_T}{dt} = [I]\left(k_3 S_\alpha + k_{2f}\left(1 - \frac{1}{1 + \frac{k_6[O]}{k_{2b}[S_\alpha]}}\right)\right) - \frac{k_1[F]}{1 + \frac{k_6[O]}{k_{2b}[S_\alpha]}} \tag{6-28}$$

$$\frac{dS_T}{dt} = k_{1f}[F]\left(\frac{1}{1 + \frac{k_5[O]}{k_{2f} + k_3[S_\alpha]}} - \frac{1}{1 + \frac{k_6[O]}{k_{2b}[S_\alpha]}}\right) + \frac{k_{2b}[S_\alpha][H]}{1 + \frac{k_5[O]}{k_{2f} + k_3[S_\alpha]}} - \frac{k_{2f}[I]}{1 + \frac{k_6[O]}{k_{2b}[S_\alpha]}} \tag{6-29}$$

$$\frac{dS}{dt} = k_{1f}[F]\left(\frac{1}{1+\frac{k_5[O]}{k_{2f}+k_3[S\alpha]}} - \frac{1}{1+\frac{k_6[O]}{k_{2b}[S\alpha]}}\right)$$ (6-30)

Now the formula is somewhat simple, with soot formation trending with the concentration of available F and the rate constant being based on a competition between pathways promoting soot formation, the reversal of soot formation, and the attack from oxidizing species. If again, we assume that the intermediates are scavenged by oxygen faster than they participate in soot reactions, then soot formation can be shown (Eqs. 6-31 - 6-32) to be a function of inception, surface growth, and reversibility, with all terms are functions of ϕ. By re-arranging (Eq. 6-33), it is observed that soot trends with ϕ with a rate constant based on high temperature inception (k_i) and surface growth, which is a function of existing nascent soot ($[S_\alpha]$) and the competition between low temperature growth (k_{ii}) and high temperature reversibility (k_{iii}).

If $k_{5f}[O] \gg k_{2f} + k_3[S_\alpha]$ & If $k_{6f}[O] \gg k_{2b}[S_\alpha]$

$$\frac{dS_T}{dt} = \left(\frac{k_1 k_{2f}}{k_5}\right)\phi + \left(\frac{k_1 k_3}{k_5}\right)[S_\alpha]\phi - \left(\frac{k_{2b}}{k_6}\right)[S_\alpha]\phi$$ (6-31)

$$\frac{dS_\alpha}{dt} = \left(\frac{k_1 k_{2f}}{k_5}\right)\phi - \left(\frac{k_{2b}}{k_6}\right)[S_\alpha]\phi$$ (6-32)

$$\frac{dS}{dt} = \phi * \left(k_i + S_\alpha(k_{ii} - k_{iii})\right)$$ (6-33)

Scheme 6

Lastly, a derivation made by expanding the intermediates from Scheme 5. Below there are two intermediates, one of which (I) is like acetylene and the other (A) is more like an aromatic. The inception process is a two-step pyrolysis from fuel to soot, where nascent soot is formed. Surface growth can then occur on either nascent or mature soot. This level of detail makes the analysis quite complex (see Eq. 122), even with species A and H being considered small enough to treat with the SSA and the higher order terms (Eq. 6-33) removed. Several of the terms in Eq. 6-34are given underscores which communicate which process is being represented.

$$F \rightarrow I + H \qquad\qquad\qquad F + O_{lumped} \rightarrow P$$

$$I \leftrightarrow A + H \qquad\qquad\qquad I + O_{lumped} \rightarrow P$$

$$A \leftrightarrow S_\alpha + H \qquad\qquad\qquad A + O_{lumped} \rightarrow P$$

$$S_\alpha + I \rightarrow S_\beta \qquad\qquad\qquad H + O_{lumped} \rightarrow P$$

$$S_\alpha + A \rightarrow S_\beta$$
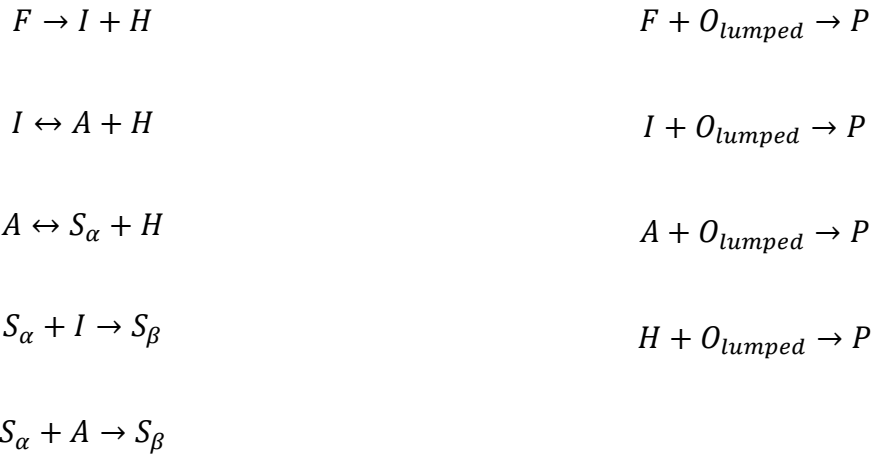
Assume A, H are in steady-state.

$$\frac{dS}{dt} = \left(k_{2f} \left(\underbrace{\frac{1}{1+\frac{k_{2b}H+k_8O}{k_{3f}+k_5S_\alpha}}}_{Incep\ \&\ SG\ from\ A} - \underbrace{\frac{1}{1+\frac{k_{2b}A+k_9O}{k_{3b}S_\alpha}}}_{Rev\ Incep\ from\ H} \right) + \underbrace{k_4 S_\alpha}_{SG\ via\ I} \right) I - \left(k_{10}S_\alpha + k_{11}S_\beta \right)O \qquad (6\text{-}34)$$

$$\frac{dS}{dt}\Big|_{H.O.T.} = \frac{k_{3b}S_\alpha H}{1+\frac{k_{2b}H+k_8O}{k_{3f}+k_5S_\alpha}} - \frac{k_{3f}A}{1+\frac{k_{2b}A+k_9O}{k_{3b}S_\alpha}} \qquad (6\text{-}35)$$

Since there are two intermediates now and I is closer to an acetylene-type species, the steady-state assumption should not be assumed for I. As a result, all soot formation in Eq. 6-34is dependent on I rather than F as with other schemes above. If SSA is used for I, the first term in Eq. 6-34becomes Eq. 6-36with another higher-ordered term in Eq. 6-37.

$$\frac{dS}{dt} = \left(k_{2f} \left(\underbrace{\frac{1}{1+\frac{k_{2b}H+k_8O}{k_{3f}+k_5S\alpha}}}_{Incep\ \&\ SG\ from\ A} - \underbrace{\frac{1}{1+\frac{k_{2b}A+k_9O}{k_{3b}S\alpha}}}_{Rev\ Incep\ from\ H} \right) + \underbrace{k_4S_\alpha}_{SG\ via\ I} \right) \frac{k_1[F]}{k_{2f}+k_4S\alpha+k_7O} \tag{6-36}$$

$$\frac{dS}{dt}\Big|_{H.O.T.} = \left(\frac{1}{1+\frac{(k_4S\alpha+k_7O)}{k_{2f}}} \left(\underbrace{\frac{1}{1+\frac{k_{2b}H+k_8O}{k_{3f}+k_5S\alpha}}}_{Incep\ \&\ SG\ from\ A} - \underbrace{\frac{1}{1+\frac{k_{2b}A+k_9O}{k_{3b}S\alpha}}}_{Rev\ Incep\ from\ H} \right) + \underbrace{k_4S_\alpha}_{SG\ via\ I} \right) k_{2b}[A][H] \tag{6-37}$$

The collective features of these models are somewhat straightforward. In the cold region away from the flame formation >> "oxidation" ($k_2 + k_3[S] \gg k[O]_l$) and then many of these models collapse to:

$$\omega_S = k_1[F] \tag{6-38}$$

i.e. soot directly forms from fuel. Here, the inception and surface growth distinction disappears. When SSA is used on the soot precursor and then it is further assumed that soot formation dominates the competition for the precursor, then effectively any fuel that becomes the intermediate will become soot. When oxidation >> formation ($k[O]_l \gg k_2 + k_3[S]$), then the models become:

$$\omega_S = \phi \left(k_{inc} + k_{SG}[S] - k_{rev}[S] \right) \tag{6-39}$$

Where the 3 important processes related to formation are distinct (oxidation would also be included for a full treatment). The fuel dependency would come through the phi parameter. While this was the desired formula, this applies to a regime close to the flame, where the intermediate is attacked by lumped oxygen but some is still available for soot formation. In between these two regimes, the chemical expression is too complex to derive a ϕ-based model. At best, soot formation can be seen as defined by the behaviors of two boundaries, with the bulk intermediate region being a mixture of these chemical regimes. While this method ultimately did not come to fruition in terms of validating the initial Φ based model, it did enable developments in the model as seen below where formation and reversibility are modeled as distinct processes.

6.4   Formation – Reversibility Soot Model

6.4.1 Motivations

Given these various considerations, we propose an alternative semi-empirical modeling approach with the aim to capture both the competition between formation and the reversing processes that occur on the fuel-side of a diffusion flame. This two-term formulation indicates competition between these processes, with the total soot formation being the net sum between the two. For this new model, the net soot production is zero at the location $\Phi_{crit} = 0.65$, indicating that the soot-formation process is balanced by reversibility. This value was chosen as the median value of the reversibility region as observed in Figs. 1, M and was in the bounds of Φ as determined by Table N. we seek to capture this effect conceptually, concisely, and recognize that to fully capture the nuances of this phenomenon would require modeling effects whose detail is beyond

the aim and scope of this project. This effect is achieved by fitting the various rate constants so that the overall rate becomes zero at this location, as described further below.

Formation-Reversible Model:

$$\omega_S = \omega_{form} - \omega_{rev} \tag{6-40}$$

$$\omega_{form} = k_{form} Y_{F,B} \exp\left(-\frac{T_{A,form}}{T}\right) \tag{6-41}$$

$$\omega_{rev} = k_{rev} \exp\left(-\frac{T_{A,rev}}{T}\right) \tag{6-42}$$

where

$$Y_{F,B} = Y_{F,0} \frac{Z - Z_{st}}{1 - Z_{st}} \tag{6-43}$$

6.4.2 Normalization Method

The formation Arrhenius temperature for a one-step soot formation process is set to $T_{A,form} = 15,600\ K$, as determined from measurements found the literature [84]. The leading constants for the two terms in the model and the activation temperature in Eq. (12) are determined by fitting to experimental data available in the literature and by using the procedure outlined below. In solving for the constants, three criteria are imposed: 1) that the resulting peak *svf* matches that of an experimental measurement for a particular reference flame condition [81] which is described below, 2) that no soot forms at $\Phi \leq 0.65$ for the soot inception limit flame (the formation and reversibility are equivalent at this location), and 3) that the model predict a blue (soot-free) flame for the sooting limit flame (as quantified in Chapter 4). With these three conditions, the three remaining unknowns of Eq. 6-41 – 6-42 (k_{form}, k_{rev}, $T_{A,rev}$) can be found.

6.4.3 Evaluation Results

The modeling constraints were satisfied with $k_{form} = 1.19E5$, $k_{rev} = 22.4$, $T_{A,rev} = 8,500$ K and the results are shown in Fig. 6-5. Predictions of *svf* are shown in Fig. 6-5a; soot forms and is transported via convection (designated by arrows) to the *psp* where it accumulates, leading to the signature *svf* profile of the counterflow flame. The new model agrees well with the measured *svf* values at $Z_{st} = 0.074$ [81], which can be directly verified by comparison with the experimental data points in Fig. 6-5a. The model also predicts the experimentally observed soot-free (blue) conditions for $Z_{st} = 0.393$, as the peak *svf* is below the limit line designating *svf* of 0.01 ppm.

The predicted soot formation rate profile is shown in Fig. 6-5b. Model results indicate that soot can form in a region between two boundaries as discussed in the theory section. Near the fuel inlet, soot beings to form ($\Phi \sim 0.92$ for $Z_{st} = 0.074$) as sufficient temperature is reached for the given fuel availability. On the high temperature side of the soot formation zone ($\Phi \sim 0.58$ for $Z_{st} = 0.074$), net soot production ceases as the reversing reactions surpass formation reactions. The region between this location and the flame front is not conducive to soot formation. As Z_{st} increases, the soot formation zone shrinks from both the right (high-Φ) and left (low-Φ) side of the zone. The model predicts a reduction of soot formation at higher-Φ due to the effect of dilution diminishes the fuel available to form soot. The model also predicts a reduction of soot formation at lower-Φ due to the effects captured by the reversibility term (Eq. 6-42). There are no direct experimental comparisons to the three intermediates Z_{st} (0.196, 0.291, 0.347) flames, which are displayed in Fig. 6-5 to indicate the gradual and continuous reduction of soot formation. Finally, at $Z_{st} = 0.393$, these reductions coincide to yield zero net soot formation. For this flame condition, no soot can form at Φ lower than the critical value, thus satisfying the third modeling constraint. This suppression of soot formation can also be seen by viewing the different formation (Eq. 6-41) and reversibility

(Eq. 6-42) rates, as shown in Fig. 6-5c for $Z_{st} = 0.074$, 0.291, and 0.393. For $Z_{st} = 0.074$, there is a region where the formation rate is significantly higher than the reversibility rate. As Z_{st} increases, this gap narrows until at $Z_{st} = 0.393$, when reversibility has overtaken the formation rate everywhere.
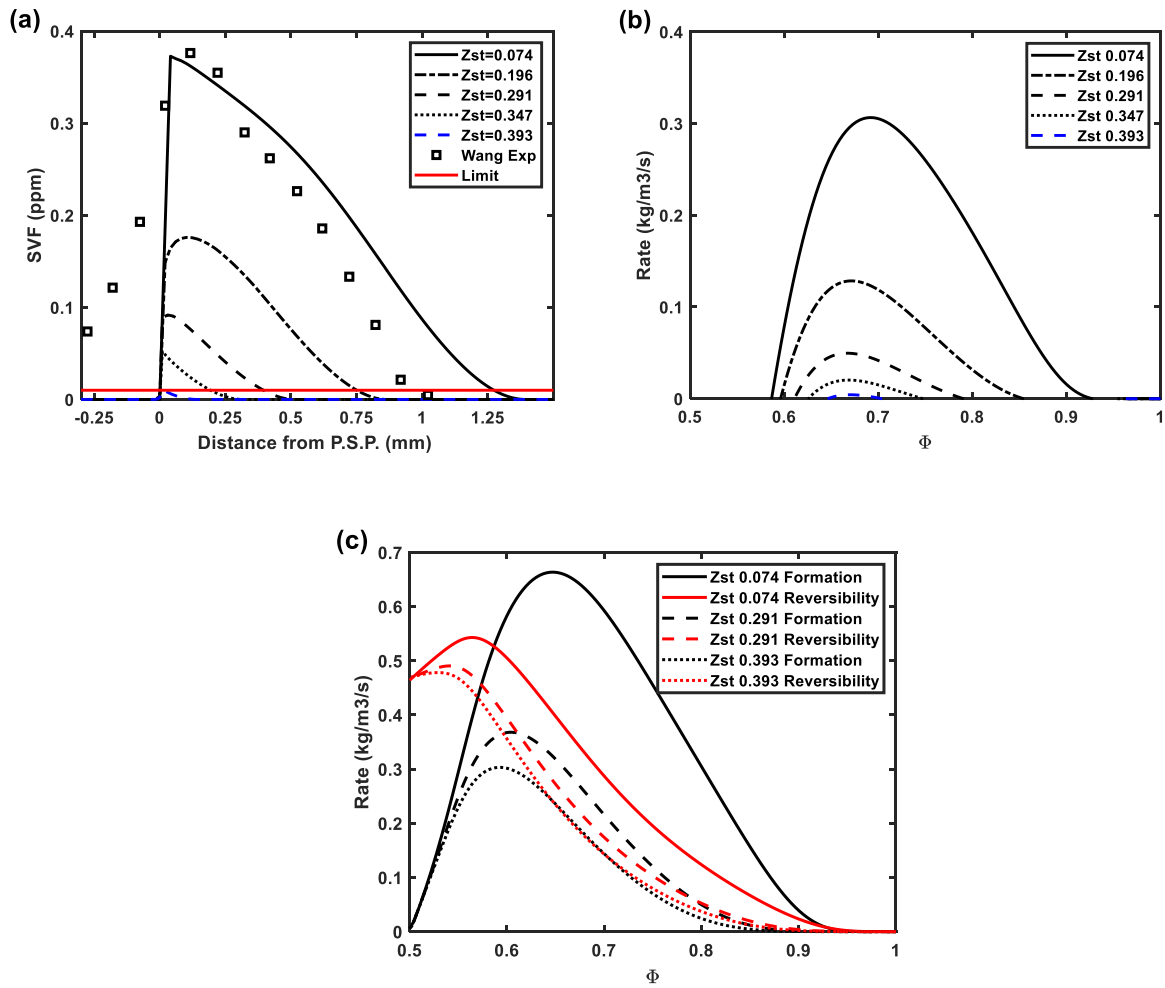
Figure 6-6: Results from the new model for all Z_{st} in the changing Z_{st} evalulation; a) predicted and experimentally measured *svf* vs. distance from *psp*; diagnostic limit for *svf* shown by red line. Arrows indicate direction of gas convection. b) total formation rate vs. Φ; c) formation and reversibility rates vs. Φ for 3 different Z_{st}; d) H+ radical mass fraction vs. Φ.

Finally, the reversibility term in Fig. 6-5c can be compared to the mass fraction of H^+ radicals predicted by the detailed KM2 model for varying Z_{st} in Fig. 6-3. It is apparent that these two curves are similar in their shape, peak location, and their trend with Z_{st}. Therefore, it is with great interest that we note that the fitting parameters and therefore the shape of the reversibility curve were determined solely by the criteria of zeroing below Φ_{cr} and balancing the limit value at high Z_{st}. While it is recognized that the reversibility process is multi-faceted, this approach appears to capture the main feature. As a final note, the reversibility processes described in this paper are more focused on precursor chemistry and therefore could be seen to more directly affect the soot inception process rather than all soot formation. The following section will use this model framework to reverse the inception process only.

6.5 Semi-Empirical Extensions

6.5.1 Motivations

Since the formation-reversible model showed considerable successes at elevated Z_{st}, another layer of detail and potential accuracy was investigated where inception and surface growth are separately considered. Rather than develop new models, two established two-step semi-empirical models were used: the Leung-Lindstedt (LL) model [47] and the Moss-Brookes (MB) model [29]. These two were chosen based on their popularity and because they show similarity of form but with varying fitting constants that result in different results for the same flame conditions (e.g. see results in [85]). Previous work by this group has shown their inadequacy at elevated Z_{st}, making them fitting candidates to investigate a reversibility-based remedy. The modified equations

are shown below with terms from the original models (Eqs. 6-46 – 6-48, 6-49 - 6-51) included. The reversible forms of the models are labelled LLR and MBR, respectively.

Semi-Empirical Models, with Modification:

$$\omega_S = k_{norm}\left((\omega_{inc} - \omega_{rev}) + \omega_{sg}\right) \tag{6-44}$$

$$\omega_n = k_{norm}\left(\frac{N_{AV}}{M_P}(\omega_{inc} - \omega_{rev})\right) - \omega_{coag} \tag{6-45}$$

Leung-Lindstedt

$$\omega_{inc} = 10^4\ [C_2H_2]\ \exp\left(-\frac{21100}{T}\right) \tag{6-46}$$

$$\omega_{sg} = f(S) * 6 * 10^3\ [C_2H_2]\exp\left(-\frac{12100}{T}\right) \tag{6-47}$$

$$f(S) = (A_s)^{0.5} = \left(\pi d_p^2 * \rho n\right)^{0.5} = \left(\pi\left(\frac{6}{\pi}\frac{1}{\rho_S}\frac{Y_S}{n}\right)^{\frac{2}{3}}\rho n\right)^{0.5} \tag{6-48}$$

Moss-Brookes

$$\omega_{inc} = 7.78 * 10^3[C_2H_2]\exp\left(-\frac{21100}{T}\right) \tag{6-49}$$

$$\omega_{sg} = f(S) * 30.7 * [C_2H_2]^{0.4}\exp\left(-\frac{12100}{T}\right) \tag{6-50}$$

$$S = A_s = \pi d_p^2 * \rho n = \left(\pi\left(\frac{6}{\pi}\frac{1}{\rho_S}\frac{Y_S}{n}\right)^{\frac{2}{3}}\rho n\right)^{1} \tag{6-51}$$

Semi-Empirical Reversible Terms

$$\omega_{rev,LL} = k_{rev,LL}\exp\left(-\frac{T_{A,rev}}{T}\right) \tag{6-52}$$

$$\omega_{rev,MB} = k_{rev,MB}\exp\left(-\frac{T_{A,rev}}{T}\right) \tag{6-53}$$

6.5.2 Normalization Method

The value of $T_{A,rev}$ is retained as used in the formation-reversible model above (8500 K). However, since the reversibility term is only applicable to inception rather than total soot formation as in the former model, k_{rev} must be found by a different condition for these models. Similar to condition (2) above, here the condition is that no soot forms at $\Phi \leq 0.65$ at the soot inception limit ($Z_{st} = 0.393$, see Chapter 4); the *inception* and reversibility are now equivalent at this location. Finally, there is a normalization factor imposed on these semi-empirical models to adjust them such that that the peak *svf* match that of an experimental measurement for a particular reference flame condition [81] which is described below, as in condition (1) above, and described previously for semi-empirical models [85]. The normalization factor is multiplied on the net inception ($\omega_{inc} - \omega_{rev}$) and mass surface growth (ω_{sg}) terms (see Eqs. 6-44 - 6-45). The values of these constants are $k_{norm} = 1.39$, $k_{rev,LL} = 1.6E-3$ (LLR) and $k_{norm} = 4.8$, $k_{rev,MB} = 1.2E-3$ (MBR). Note that these normalization factors differ from those in Table 4.2, because the equations for these models have been modified.

6.5.3 Evaluation Results

Results for the LLR model are shown in Fig. 6-6. The *svf* profiles, seen in Fig. 6-6a, show a steady decrease in peak *svf* as Z_{st} increases. At $Z_{st} = 0.074$, the peak value matches the experimental *svf*. For the experimental blue flame, the predicted peak is below the limit, thus correctly predicing soot-free conditions. In Fig. 6-6b, the predicted soot formation rate is shown. The rate is always bounded between $0.6 < \Phi < 0.9$. As Z_{st} increases, the zone region shrinks and the formation rate decreases. As the blue condition is approached, the peak formation rate location shifts to $\Phi = 0.65$. This result is consistent with the experimental observation as described above for the Φ_{cr} boundary. In Fig. 6-6c, the net nucleation rate for LLR is shown. Similar to the toal

formation rate, there is steady decrease of the inception rate magnitude and the zone size also decreases. At Z_{st} = 0.393 (blue), there is no inception. For comparison, the LL inception without reversibility is shown in Fig. 6-6d.
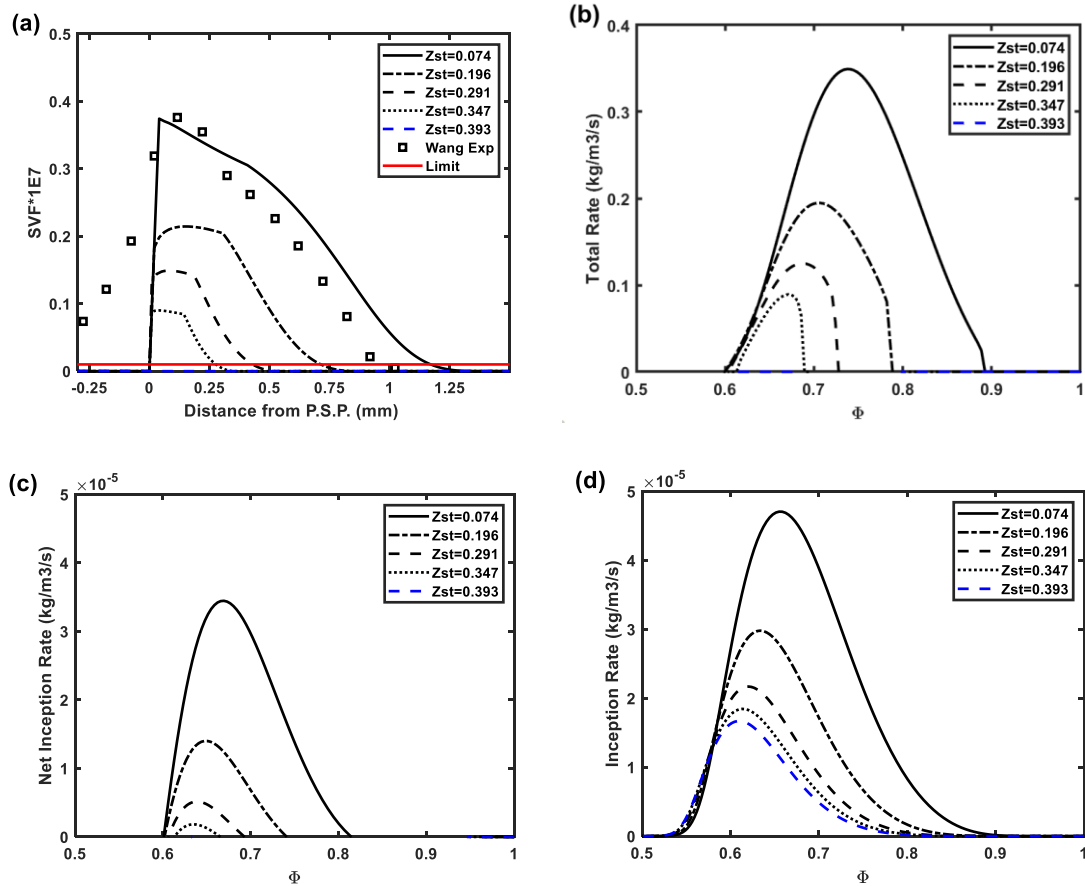
Figure 6-7: Results from the Leung-Lindstedt-Reversible model for the changing Z_{st} evalulation; a) predicted and experimentally measured *svf* vs. distance from *psp*; diagnostic limit for *svf* shown by red line. Arrows indicate direction of gas convection. b) total formation rate vs. Φ; c) net inception ($\omega_{inc} - \omega_{rev}$) rate vs. Φ; d) inception rate (ω_{inc}) vs. Φ.

The results for the MBR model are shown in Fig. 6-7 and are similar to the LLR model. The rate is more strongly affected (diminishes faster) at elevated Z_{st} due to the greater sensitivity of the surface term (Eq. 6-46 has $\omega_S \sim A_S$ while Eq. 6-43 has $\omega_S \sim A_S^{0.5}$). The comparison of this effect between two models has been previously discussed [85].
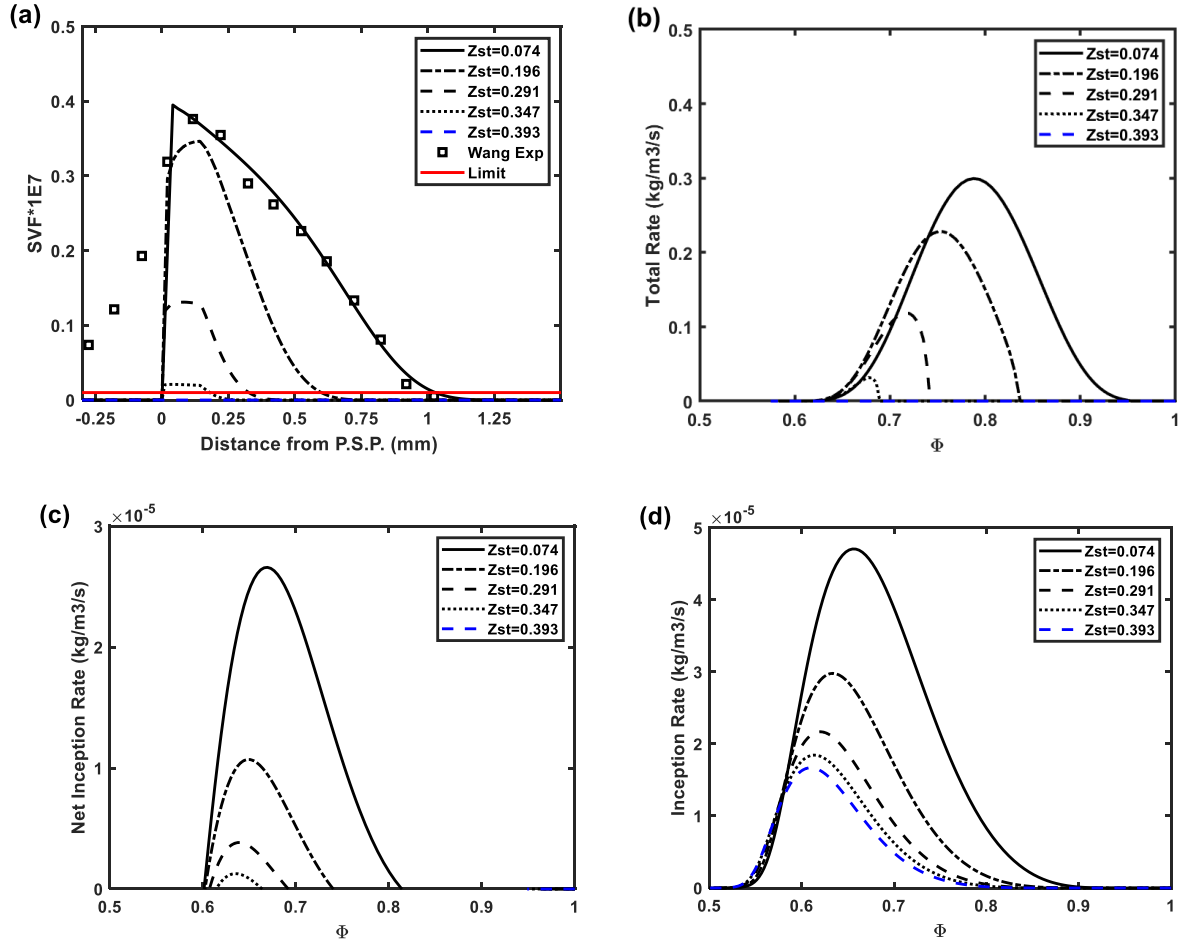
Figure 6-8: Results from the Moss-Brookes-Reversible model for the changing Z_{st} evaluation; a) predicted and experimentally measured *svf* vs. distance from *psp*; diagnostic limit for *svf* shown by red line. Arrows indicate direction of gas convection. b) total formation rate vs. Φ; c) net inception ($\omega_{inc} - \omega_{rev}$) rate vs. Φ; d) inception rate vs. Φ.

Fig. 6-8 shows the three reversible models (Eq. 6-40, LLR, MBR) plus the original models (LL, MB) for three increasing Z_{st} flame conditions, so that the model progression can be observed. While all models show agreeable predictions of *svf* compared to experimental measurements for the low Z_{st} flame (Fig. 6-8a), only the three reversible models predict soot quantities under the diagnostic limit for the blue flame, while the LL and MB models over-predict (discussed in [85]). The fact that even a one-step models can outperform standard semi-empirical models at this condition by including a single temperature-based reversibility term highlights the importance of

accounting for this feature at these conditions. Including reversibility is a necessary and sufficient condition for modeling soot at elevated Z_{st}.
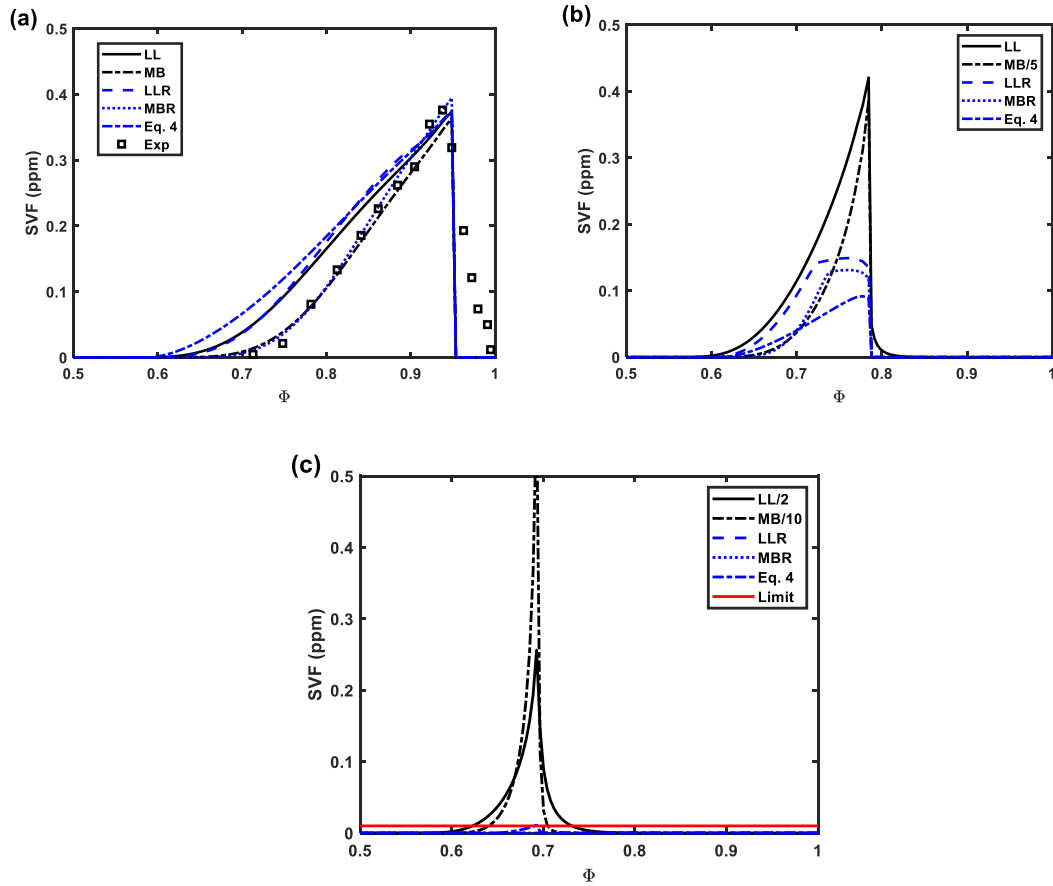
Figure 6-9. Predicted *svf* vs Φ. for all models. Arrows indicate direction of gas convection. a) $Z_{st} = 0.074$ (includes experimentally measured *svf* and diagnostic limit for *svf* shown by red line) ; b) $Z_{st} = 0.291$; c) $Z_{st} = 0.393$. Note: the reference of "Eq. 4" refers to Eq. 6-40, which was listed as "Eq. 4" in the journal manuscript from which this figure was taken.

6.5.4 Other Results

To show the robust nature of these reversible models, predictions from the five models are shown in Fig. 6-9 for two other counterflow flames where *svf* profiles have been measured. Results comparing predictions against measurements found in Hwang et al. [2] can be seen in Fig. 6-9a. This flame has different burner dimensions, inlet velocities (lower strain rate), and flame

temperature (2322 K) than the flames listed above (2517 K); full details are in Table 6-3. For this flame, the original LL model overpredicted the experimental peak *svf* by a factor of 3 while the LLR aligns with the measurements perfectly. The MB model overpredicted the peak *svf* by over an order of magnitude while the MBR underpredicted by an order of magnitude. The FR model is close to the experimental measurements, only slightly underpredicting the peak *svf*.

Flame Name, Source	$Y_{F,0}$	$Y_{O2,0}$	Z_{st}	T_{AD}	U_0 (cm/s)	D (cm)
Hwang SF 20 [2]	1.0	0.222	0.055	2322	19.5	1.42
Xu SF 30 [82]	1.0	0.329	0.088	2649	20	0.8

Table 6-3: List of flame conditions for simulations.

Results comparing predictions against measurements from Xu, et al. [82] are shown in Fig. 6-9b. This flame condition has enriched the oxygen concentration ($X_{O_2} = 0.30$) such that Z_{st} slightly increases but the flame temperature increases (2649 K) significantly compared to the flame series above. Here, both the LL and LLR are very close and both align well with the experimental *svf*. The MB and MBR models overpredict the experimental *svf* by over a factor of three and four, respectively. The model from Eq. 6-40 again performs well, with very slight overprediction. It is emphasized that the reversible models required no further adjustment to the fitting constants from the earlier results of Section 6 (but have been adjusted from Section 5). These results indicate that LLR will either maintain the same predictions or will improve them compared to LL. The results for MB and MBR are less conclusive for these flames as neither model performs very well. This is not surprising considering that the LL surface growth constants were fitted in a counterflow flame while MB was fitted for a coflow flame where growth regimes can be different (compare Eqns. 6-47, 6-48 with Eqns. 6-50, 6-51). We therefore assert that the reversibility term proposed

here is a robust feature that does not diminish prediction capability in more-traditional non-premixed counterflow flame environments. These results indicate that the Eq. 6-40 and LLR models are accurate for a wide range of counterflow flame conditions and that the reversibility framework yields a net modeling improvement, although further research is needed to fully validate these models under alternate flame conditions and flame types.
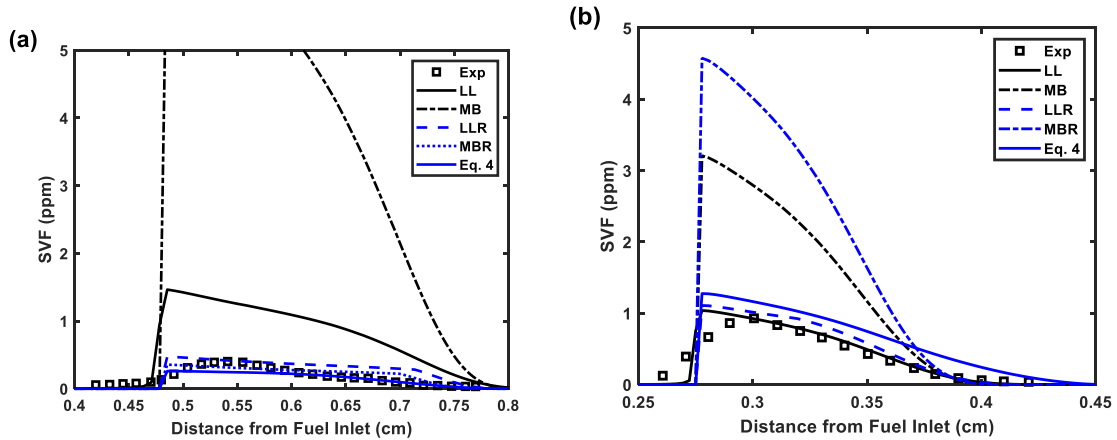
Figure 6-10. Predicted *svf* vs. distance from *psp* for all models. Arrows indicate direction of gas convection. a) Hwang SF 0.20; b) Xu SF 0.30. Note: the reference of "Eq. 4" refers to Eq. 6-40, which was listed as "Eq. 4" in the journal manuscript from which this figure was taken.

6.6 Conclusions

A new approach has been developed for semi-empirical soot models which can capture the changes in soot formation as Z_{st} is modified by accounting for both formation processes as well as important reversibilities which counteract formation. This approach uses a temperature-based term to approximate the chemical reversibilities which counter soot formation. This reversibility term was used alongside an original one-step formation model and was also added as an extension to two existing semi-empirical models (Leung-Lindstedt and Moss-Brookes).

Using this modeling approach resulted in all three models matching experimental measurements at low Z_{st} (25% O_2). More importantly, all three models correctly predicted blue (soot-free) conditions in a non-premixed counterflow flame for the first time. By comparison with models that did not include reversibility, it was demonstrated that this result cannot be obtained by considering formation processes alone. This study, therefore, shows that the performance of semi-empirical soot formation models can be dramatically improved when applied to higher-Z_{st} flames if the reversible nature of soot formation at high temperature is considered.

The models produced in this study showed good agreement with experimental svf profiles for sample flames of two other experimental data sets. Results showed that Leung-Lindstedt was either improved or that an accurate status quo was achieved while the Moss-Brookes results were less accurate (with or without the reversibility term). By using a variety of flame conditions, it is shown that while this reversibility framework is simple, it is also robust and applicable for a wide range of counterflow flames. Finally, here is a need for additional experimental measurement of svf in higher-Z_{st} flames to validate such models.

6.7 Supplemental Material

Categorization of Reactions (by Reaction Number in the KM2 mechanism):

C_1:

R: CH$_2$, P: H	R:CH$_3$, P:	R:CH$_3$, P: H	R:CH$_3$, P: H$_2$	R: CH$_2$O, P:	R:CH$_3$, P: OH	R: CH$_2$, P: H$_2$	R: CH$_4$, P: H
1153	765	-777	1165	949	-988	1137	-1138
	-990	-979		950			
	1104	-982					
	1162	1103					
	-1163	1154					
		-1157					

C_2:

R: C$_2$H, P: H	R: C$_2$H$_2$, P:	R: C$_2$H$_2$, P: H	R: C$_2$H$_3$, P: H	R: C$_2$H$_3$, P:	R: C$_2$H$_3$, P: H$_2$	R: C$_2$H$_3$, P: H$_3$
784	785	786	794	795	999	960
814	812	826	796	973	1034	961
815	-813	827	797	977		
825	835	836	927			
833	846	847	971			
834	871	872	975			
870	-980	873	1010			
966	1008	890	1015			
967	1009	1004	1021			
1036	1020	1030				
	-1031	1033				
	1032	1035				
	-1055	1054				
	1121	-1087				
	1242	-1091				
	1291	1098				
	1292	-1101				
	1306	1122				
		1234				
		1272				
		1273				

		1274			
		1275			
		1276			
		1315			
		1325			
		1333			
		1351			

C_2, continued:

R: C_2H_4, P: H	R: C_2H_4, P:	R: C_2H_4, P: H2	R: C_2H_5, P: H	R: C_2H_5, P:	R: C_2H_6, P: H
944	947	1011	-939	-943	1110
974		1016			
978		1022			

C_3 Addition:

R: C_3H_3, P: H_2	R: C_3H_3, P:	R: C_3H_3, P: H	R: C_3H_2, P:	R: C_3H_2, P: H	R: C_3H_5, P:H_2	R: CH_2CO, P: OH	R: CH_2CO, P: O
1039	1092	1119	1127	1136	1150	-1267	-1268
	1096	1120		1147	1151	-1270	-1295
	1124	1125		1148		-1294	
	1126	1146				-1297	
						-1341	

C_9 Dimerization:

1152

Aromatic-Condensation:

R: A_1, P: H	R: A_1, P:	R: A_1, P: H_2	R: A_1, P: H, H_2	R: A_2, P: H	R: A_2, P: H2
867	884	1014	959	1316	1317
868	886	1118	1013		

869					
883					
887					
1123					

List of Reactions Used:

765. A1-+CH3=C6H5CH3

777. C6H5CH2+H=A1-+CH3

784. A1+C2H=A1C2H+H

785. A1-+C2H2=n-A1C2H2

786. A1-+C2H2=A1C2H+H

794. A1+C2H3=A1C2H3+H

795. A1-+C2H3=A1C2H3

796. A1-+C2H3=i-A1C2H2+H

797. A1-+C2H3=n-A1C2H2+H

812. A1C2H*+C2H2=>A1C2HC2H2

813. A1C2HC2H2=>A1C2H*+C2H2

814. A1C2H*+C2H2=A1C2H_2+H

815. A1C2H*+C2H2=naphthyn+H

825. A1C2H+C2H=A1C2H_2+H

826. A1C2H3*+C2H2=>A2+H

827. n-A1C2H2+C2H2=>A2+H

833. A2+C2H=A2C2HA+H

834. A2+C2H=A2C2HB+H

835. A2-1+C2H2=A2C2H2

836. A2-1+C2H2=A2C2HA+H

846. A2C2HB*+C2H2=>A3-1

847. A2C2HB*+C2H2=A2C2H_2+H

867. A1C2H*+A1=>A3+H

868. A1-+A1C2H=>A3+H

869. A1-+A1C2H=>A3+H

870. A3+C2H=A3C2H+H

871. A3-4+C2H2=A3C2H2

872. A3-4+C2H2=A3C2H+H

873. A3-4+C2H2=>A4+H

883. A1+A1-=P2+H

884. A1+A1-=P2-H

886. A1-+A1-=P2

887. A1-+A1-=P2-+H

890. P2-+C2H2=>A3+H

927. A1C2H+C2H3=>A2+H

939. A1C2H5+H=A1+C2H5

943. A1C2H5=A1-+C2H5

944. A1C2H*+C2H4=>A2+H

947. A1-+C2H4=A1C2H4

949. A1-+CH2O=A1CH2O

950. A1-+CH2O=A1CHO+H

959. A2+A1-=>FLTN+H+H2

960. A2+C2H3=A2C2H2+H2

961. A2+C2H3=A2C2H2B+H2

966. A2C2H2+C2H2=>A3+H

967. A2C2H2B+C2H2=>A3+H

971. A2C2HA+C2H3=>A3+H

973. A2C2HA*+C2H3=>A3

115

974. A2C2HA*+C2H4=>A3+H

975. A2C2HB+C2H3=>A3+H

977. A2C2HB*+C2H3=>A3

978. A2C2HB*+C2H4=>A3+H

979. A2CH2+H=A2-1+CH3

980. A2CH2=C9H7+C2H2

982. A2CH3+H=A2+CH3

990. A2CH3=A2-1+CH3

999. A2R5+C2H3=A2R5C2H2+H2

1004. A2R5C2H2+C2H2=>A3R5+H

1008. A2R5C2HY+C2H2=>A3R5X

1009. A2R5-+C2H2=A2R5C2H2

1010. A2R5-+C2H3=A2R5C2H2+H

1011. A2R5-+C2H4=A2R5C2H2+H2

1013. A2-1+A1=>FLTN+H+H2

1014. A2-1+A1-=>FLTN+H2

1015. A2-1+C2H3=A2C2H2+H

1016. A2-1+C2H4=A2C2H2+H2

1020. A2-2+C2H2=A2C2H2B

1021. A2-2+C2H3=A2C2H2B+H

1022. A2-2+C2H4=A2C2H2B+H2

1030. A3R5X+C2H2=A4R5+H

1031. A3-4=>A2R5-+C2H2

1032. A2R5-+C2H2=>A3-4

1033. A3-1+C2H2=A3R5+H

1034. A3-1+C2H3=A3R5+H2

1035. A4-2+C2H2=A4R5+H

1036. C6H2+C2H=C8H2+H

1039. C9H7+C3H3=A2R5+H2

1054. C6H5CH2+C2H2=C9H8+H

1055. C6H5CH2=c-C5H5+C2H2

1087. C7H6+H=>c-C5H5+C2H2

1091. C7H5+H=C5H4+C2H2

1092. C7H5(+M)=C4H2+C3H3(+M)

1096. c-C5H5(+M)=C2H2+C3H3(+M)

1098. C3H3+C2H2=C5H4+H

1101. C5H3+H=C3H2+C2H2

1103. C6H5CH2+CH2=A1C2H3+H

1104. C6H5CH2+CH3=A1C2H5

1110. A1-+C2H6=A1C2H5+H

1118. A1-+A1-=BIPHEN+H2

1119. A1-+C3H3=A1C3H2+H

1120. A1C3H2+C3H3=P2-+H

1121. C7H6+C2H2=C9H8

1122. C7H6+C2H2=C9H7+H

1123. A1-+AC3H4=C9H8+H

1124. A1-+C3H3=C9H8

1125. A1+C3H3=C9H8+H

1126. C6H5CH2+C3H3=C10H10

1127. C6H5CH3+C3H2=C10H10

1136. C9H7+C3H2=A2R5+H

1138. C6H5CH3+H=A1-+CH4

1146. A2CH2+C3H3=>A3+H+H

1147. A2CH3+C3H2=>A3+2H

1148. A2CH2+C3H2=>A3+H

1150. A2CH2+C3H5-A=>A3+H2+H2

1151. A2CH2+C3H5-S=>A3+H2+H2

1153. A3CH2+CH2=>A4+H2+H

116

1154. A3-4+CH3=A3CH2+H

1157. A3CH3+H=A3+CH3

1162. c-C5H5+CH3=>C5H5CH3

1163. C5H5CH3=>c-C5H5+CH3

1165. c-C5H5+CH3=C5H4CH2+H2

1234. A3-1+C2H2=A3C2H-2+H

1242. A3C2H-JS+C2H2=CHRYSENJ1

1272. CHRYSENJ4+C2H2=BAPYR+H

1273. CHRYSENJ5+C2H2=BAPYR+H

1274. A4-1+C2H2=PYC2H-1+H

1275. A4-2+C2H2=PYC2H-2+H

1276. A4-4+C2H2=PYC2H-4+H

1291. PYC2H-1JP+C2H2=>BAPYRJS

1292. PYC2H-2JS+C2H2=>BAPYRJS

1306. PYC2H-4JS+C2H2=>BEPYRENJS

1315. BEPYRENJS+C2H2=>BGHIPER+H

1316. A2-1+A2-1=>PERYLEN+2H

1317. A2-1+A2=>PERYLEN+H2+H

1325. PERYLENJS+C2H2=>BGHIPER+H

1333. BAPYRJS+C2H2=>ANTHAN+H

1351. BGHIPEJS1+C2H2=>CORONEN+H

Chapter 7: Expanding Emission Predictions through Machine Learning

7.1 Introduction

Combustion process are important for a vast array of industries such as energy production, cement, food processing, and heating. However, an abundance of excess air is provided to avoid incomplete combustion which would waste fuel and create emissions such as CO and PM. By operating at more optimal conditions (closer to stoichiometric) and increasing boiler efficiency through processes such as by using less air, less heat will be rejected from the system, leading to lower fuel usage (lowering costs) and lower CO_2 emissions. Ideally, future efficiency in the system could be predicted based on current internal and external factors, and then adjustments made to the airflow in real time to mitigate low performance even before it occurs. However, external factors like weather, fuel quality, and aging equipment (the average age of American power plants is over 28 years old [2]) drastically change what are the optimal operating conditions to achieve perfect combustion. In addition to efficiency concerns, there is a continued challenge to meet increasingly stringent demands on emissions such as NO_X and PM. At times, there is a trade-off between these two types of emissions due to chemical regime which favors one or the other pollutant (low excess O_2 can favor CO creation while high excess O_2 can favor NOx creation).

A variety of potential remedies exist for pollutant related issues, such as modifying operating conditions (inputs) or processing the exhaust gas (outputs). Pursuing alternative operating conditions appears to be far cheaper than adding modifications to existing power plants such as catalytic reactors for NOx [86] and can also directly address the efficiency issues describes above.

To find these alternative operating conditions, recourse can be made to either heavy monitoring of the boiler or else to modelling the system. The current standard for combustion monitoring is to use dedicated sensors for each variable of interest – potentially several dozens for a large facility. These sensors are difficult to install, expensive to maintain,. [87] susceptible to harsh combustion environments lead to constant maintenance and frequent calibration [88, 89], and are slow to process dynamic changes in complex combustion environments. Further, by solely relying on monitoring, operators may not even be aware of certain conditions which are optimal for performance and emissions. Better understanding of the exact combustion conditions can improve power plant efficiency, reduce operating and maintenance costs, and help maintain a reliable and resilient energy infrastructure by ensuring the operators are able to achieve and maintain optimal performance.

Therefore, modelling the system has significant potential for meeting these constraints in a cost-effective manner. Several modelling options exist. One option is that of an input-output map, but these 'models' are ad-hoc and lose effectiveness with system aging. The system in question could also be modeled in a detailed manner; however, this option can be computationally expensive [87], challenging [86, 89], or even inaccurate [88] due to the multitude of complexity of NOx formation pathways. These criticisms leave open the option of developing new models using artificial intelligence (AI), which offers the ability not only to model the system but also to optimize the system operation conditions [89, 90]. Analysts can run in silico experiments with these models to optimize thermal efficiency and train algorithms to recommend ideal plant settings in real-time. Thus, using artificial intelligence and high-performance computing our proposed solution could help fossil fuel users address the challenges caused by increasing supply of intermittent energy on the grid and emission reduction goals. Next, a brief review is given of some

attempts to model combustion problems using various AI techniques, followed by the need for a novel algorithm to address operational optimization for a powerplant boiler.

Machine learning algorithms have already been developed for a range of varying combustion applications. An important application can be found in engines, which are highly complex to their high-pressure and transient nature. An overview of work done in this area can be found in Table 7-1, which includes predictions of NOx and soot and also operational parameter optimization. Machine learning techniques have also been utilized in coal combustion applications. These studies have primary focused on the emission of NO_X, a quantity which would be difficult to predict even with the availability of detailed chemical mechanisms. Many different techniques and algorithms have been used to address this prediction and are catalogued in Table 7-2. An assortment of other machine learning applications to combustion can be found in Table 7-3. The work of Tan et al. is particularly insightful. These authors have indicated that ELM was favorable to traditional ANN and LSTM was favorable to SVM and has also noted that "the training process can become intractable with a large data set (2016) and has focused on updating models to handle transient boiler operations. F. Wang lists many issues with previous attempts to use data driven methods on NOx which encompass both data collection and modelling techniques.

First Author & Citation	Year	Application	Inputs / Diagnostics	Algorithms Used	Outputs / Predictions
Alcan [91]	2019	diesel engines		gated recurrent unit (GRU) network; nonlinear autoregressive with exogenous input (NARX)	Soot emission
Potenza [92]	2020	Turbo-charged GDI		Neural Network Two Color (NNTC)	Soot
Badra [93]	2019	Gasoline compression ignition (GCI)		Machine Learning-Grid Gradient Algorithm (ML-GGA) Machine learning Genetic Algorithm (ML-GA),	optimize the operating conditions (case 1) and the piston bowl design (case 2)
Mao [94]	2019	ethanol-diesel engine	ethanol, power, engine speed.	back-propagation (BP), Elman network, radial basis network (RBF) generalized regression neural network (GRNN)	brake specific fuel consumption (BSFC), effective brake specific fuel consumption (EBSFC), effective brake thermal efficiency (EBTE), exhaust gas temperature (EGT), CO, HC, NOX, Soot
Pan [95]	2020	PCCI engine	cylinder pressure, engine	combining principal component analysis (PCA) to reduce inputs dimensions	NOx, Soot

			operations parameters	with a multi-layer perceptron (MLP) neural network	
Liu [96]	2016	diesel engine		principal component analysis (PCA) genetic algorithm (GA) support vector machine (SVM)	NOx
Lughofer [87]	2011	Internal combustion engine		(short for FLEXible Fuzzy Inference Systems)	NOx (prediction)
Yu [97]	2019	Reactivity Controlled Compression Ignition (RCCI) engines	local equivalence ratio (ER) and temperature	K-means clustering algorithm	Soot

Table 7-1. Literature survey of machine learning advancements related to engine-based combustion.

First Author & Citation	Year	Application	Inputs / Diagnostics	Algorithms	Outputs / Predictions
Buyamin [98]	2013	power generation plant		hybrid Genetic Algorithm Linear Regression (GA-LR)	NOx emissions
F. Wang [88]	2018	coal-fired power plants		deep belief network (DBN)	NO emission
P. Tan [86]	2016	coal-fired power plant	10000 samples from the real power plant, covering 7 days?	ELM (extreme learning machine) HS (harmony search)	NOx
P. Tan [99]	2019	coal-fired power plant	10000 samples from the real power plant, covering 7 days?	long short-term memory (LSTM) support vector machine (SVM)	NOx
Zheng [100]	2009	coal-fired utility boiler		Support vector regression (SVR) ant colony optimization (ACO) genetic algorithm (GA) particle swarm optimization (PSO)	NOx (optimization)
C. Wang [101]	2020	coal-fired boiler		Gaussian Process (GP) Genetic Algorithm (GA) Support Vector Machines (SVM)	NOx (optimization)

Zhou [102]	2004	large capacity pulverized coal fired boiler	over-fire-air (OFA) flow rates, coal properties, boiler load, air distribution scheme and nozzle tilt	artificial neural networks (ANN)	NOx Carbon burnout (optimization)
Lv [89, 103]	2015	coal-fired boiler	"real operation data"	adaptive least squares support vector machine (LSSVM)	NOx (prediction)
Lv [89, 103]	2013	coal-fired boiler	"real operation data"	partial least squares (PLS) adaptive least squares support vector machine (LSSVM)	NOx (prediction)
Hao [104]	2001	coal burned utility boiler		neural network	NOx (optimization)
N. Li [105]	2015	biomass combustion	flame radical imaging	deep learning (DL)	NOx emissions (Prediction)
Ilamathi	2013	210 MW pulverized coal-fired boiler	flue gas O2, coal prop, coal flow, boiler load, air dist. scheme, flue gas temp., nozzle tilt	artificial neural network (ANN) genetic algorithm (GA)	NOx (prediction and optimization)
P. Tan [90]	2016	coal-fired utility boilers		principle component analysis (PCA) support vector regression (SVR)	NO$_X$ emissions

124

		coal and biomass combustion applications		artificial neural network (ANN)	
Han [106]		coal and biomass combustion applications		stacked sparse autoencoder based deep neural networks	combustion stability monitoring

Table 7-2. Literature survey of machine learning advancements related to powerplant (coal-based) combustion.

First Author & Citation	Year	Application	Inputs / Diagnostics	Algorithms	Outputs / Predictions
Cuccu	2017	heavy-duty gas turbines	Operating parameters		Emission predictions
Li [107]	2020	Roadside		Random Forest (RF)	PM2.5 and NOx
Ren [108]	2019	Hencken flat flame	spectral infrared emission measurements	neural networks	Temperature, CO, CO_2, and H_2O
Grant-Jacob	2018	general	images	Neural networks	Material, number of microspheres, mapping of location on the substrate, real-time detection of airborne pollutants
Tamas [109]	2016	air quality	ozone (O3), nitrogen dioxide (NO2) and particulate matter (PM10)	MultiLayer Perceptron (MLP), hybridized with hierarchical clustering and with a combination of self-organizing map and k-means clustering	forecasting models
Garcés [110]		total radiation, flame temperature		extreme learning machines (ELM) based methods and partial least squares (PLS) regression	of estimating energy efficiency

Table 7-3. Miscellaneous machine learning applications to combustion.

Research in the area of machine-learning based approaches to combustion is a developing field, with the above survey attesting to the willingness of investigators to develop new models. However, the ultimate success of such models is largely dependent upon the availability of sufficient operating data for model training and validation. The objective of this work is to perform a series of experiments in a laboratory-scale combustor to provide data to train, via machine learning, and to validate a combustion emissions model through exploratory data analysis and supervised simulations. In so doing, the feasibility and utility of machine learning-based combustion models can be demonstrated and evaluated. A validated combustion emissions model can be used to determine the ideal operating conditions for a system through stochastic optimization and, ultimately, enable operators to run fast, inexpensive in silico experiments on their facilities without disrupting operations and an optimizer that maximizes combustion efficiency with more accurate controls, lowering greenhouse gas emissions, saving operators' time and the company money in fuel costs.

7.2 Experimental Methods

Experiments were performed in a 25 kW horizontally-fired reaction with a triaxial burner was used and has been previously described [111]. The burner was of a tri-axial configuration with three gas flow inputs: fuel (methane), primary oxidizer (PO), and secondary oxidizer (SO). The secondary oxidizer was split into axial and swirl streams. Axial flow was achieved in the former stream by passing through flow straighteners. The swirl stream was introduced tangentially to the wall, mixing with the axial stream. The proportion of these two streams determines the extent of

swirl in the SO and is quantified by Eq. 7-3. All gas flows were set manually with control valves and measured with rotameters.

The combustion chamber was 2.43 m in length with a 16.7 cm inner diameter and was followed downstream by a second section for complete exhaust gas mixing, soot burnout, and heat rejection that was 120 cm in length and 37 cm inner diameter. Eight type-K thermocouples were placed at intervals along the reactor, with the first thermocouple measuring the entering air velocity and the last thermocouple placed in the burnout section. The burnout section was connected to the facility ventilation system which pulled a slight vacuum. Exhaust gas was extracted for measurement via sampling probe which was inserted into the burnout section of the reactor. A diagram of the burner and diagnostics are shown in Fig. 7-1.
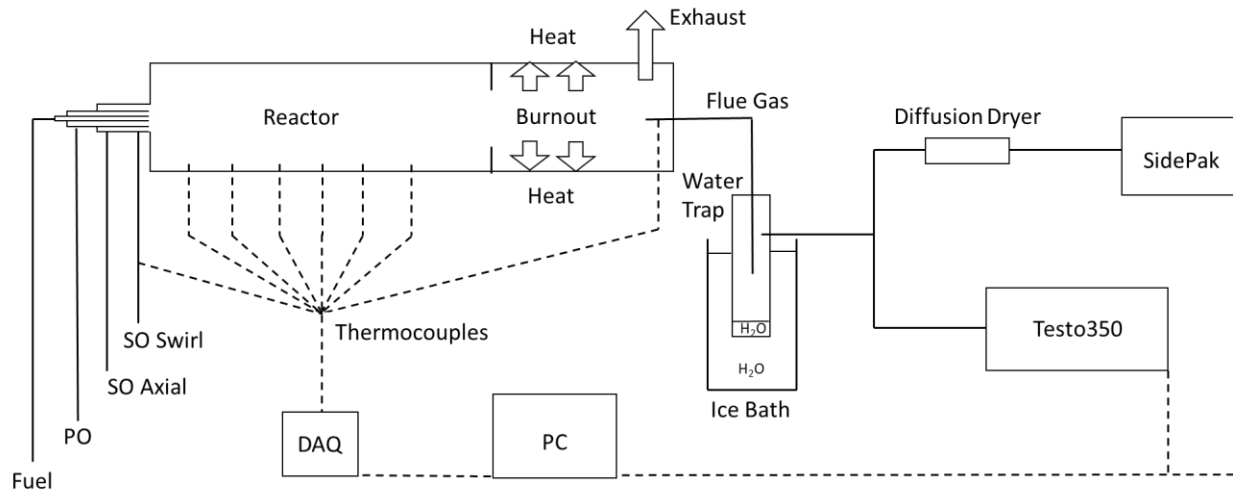
Figure 7-1. Experimental setup of combustor with gas inputs, exhaust outputs, and various diagnostics to measure temperature, exhaust composition and emission quantities.

The sampling line was passed to an in-house condensation trap surrounded by an ice bath. After exiting the trap, the sampling line was split. One section was passed through an inline filter

before entering a Testo350 continuous emissions monitor (CEM) which measured concentrations of O_2, CO, NO, and CO_2. The accuracy of these quantities are listed in Table 7-4 below. N_2 concentration was calculated by the Testo as the remaining quantity. The second split in the sampling line was passed to a SidePak™ Personal Aerosol Monitor AM520 (light-scattering laser photometer) to measure the scattering signal of particulate matter under 2.5 micrometers (PM2.5). All measured gaseous and PM emission concentrations were converted to units of weight per unit thermal input. Since the SidePak is calibrated using Arizona road dust, and the carbonaceous particulate formed in this system differs from road dust with respect to size distribution and optical properties, the measured quantity is a relative rather than absolute amount. Therefore, PM2.5 emissions are reported in arbitrary units.

Quantity	Measurement Range	Accuracy
CO	0 to 199 ppm CO	±5 ppm
	200 to 2000 ppm CO	±5% of mv
	2001 to 10000 ppm CO	±10% of mv
NOx	0 to 99 ppm NO	± 5 ppm
	100 to 1999.9 ppm NO	±5% of mv
	2000 to 4000 ppm NO	±10% of mv
CO_2	0 to 25 vol.% CO_2	±0.3 vol. % CO_2+ 1% of mv
	>25 to 50 vol.% CO_2	±0.5 vol. % CO_2+ 1.5% of mv
O_2	0 to 25 vol.% O_2	± ±0.2% of vol.

Table 7-4. Accuracy listings from the Testo350 for the gas quantities as a function of the measurement range.

Combinations of the four input controls of the reactor (fuel, PO, SO Swirl, and SO Axial) lead to four calculated quantities which characterize the combustion process: thermal input, stoichiometric ratio (λ), stoichiometric ratio of the PO (λ_{PO}), and swirl percent. These quantities are defined in Eqs. 7-1 – 7-3.

$$\lambda = \frac{(F/A)}{(F/A)_{st}} \tag{7-1}$$

$$\lambda_{PO} = \frac{(F/A)_{PO}}{(F/A)_{st}} \tag{7-2}$$

$$Swirl\ \% = \frac{\dot{m}_{Swirl}}{\dot{m}_{Swirl} + \dot{m}_{Axial}} \tag{7-3}$$

The relationships between the primary inputs (gas flows) and derived inputs (Eqs. 7-1 – 7-3, plus thermal input), and measured outputs (Table 7.4) are shown in Fig. 7-2. While the relationships between primary and derived inputs can be interconnected, the relationships are algebraic in nature and therefore deterministic. On the contrary, the relationship between derived inputs and outputs can be complex (see CO, NO, and PM in Fig. 7-2) and dependent on multiple kinetic pathways. The algorithm developed here will be trained to capture these complexities and be able to predict future outputs from given inputs. To provide a comprehensive data set for algorithm training, these quantities were varied in a systematic manner in order to obtain all possible combinations of input variables ($kW, \lambda, \lambda_{PO}, Swirl\ \%$). A summary of these conditions is listed in Table 7-5, which the varied quantity in italics. A full set of the conditions (rather than ranges) can be found in Section 7.6 (Supplemental Material).
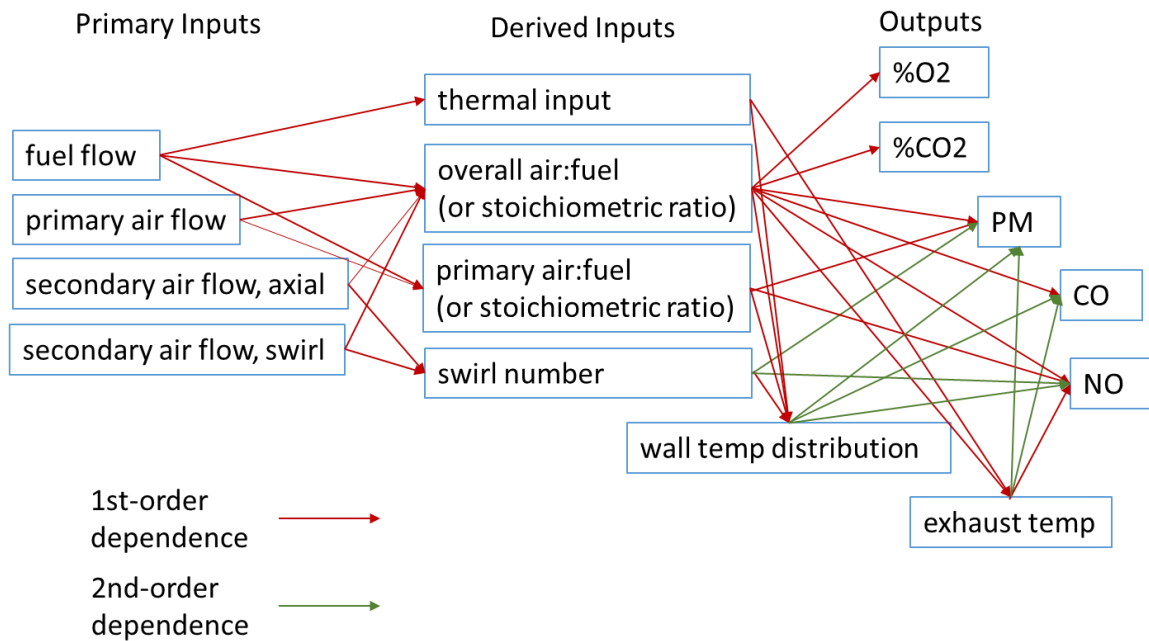
Figure 7-2 Causal diagram indicating the relationships between primary inputs (physical quantities controlled in the system), derived inputs (calculated quantities), and outputs (measured quantities).

Recordings were made of temperature, O_2, CO_2, CO, NO, and PM2.5. Experiments were typically performed by preheating the reactor for 2-3 hours to achieve a steady temperature distribution. Then, 5-6 conditions were met between the range in consideration, with each condition being held at 30 minutes. Diagnostic resolution was initially at 5 sec, but later refined to 1 sec. In sum, over 66 hours were spent running the reactor with over 57 hours being allocated to data-generating conditions, generating over 140,000 total data points for the algorithm training.

Fuel (kW)	SR, Total (λ)	SR, PO (λ)	Swirl %	Experiment #
12	*1.2-1.4*	0.3	66.7%	6, 12
14	*1.07-1.37*	0.3	66.7%	5, 13
14	1.39	*0.2-0.29*	66.7%	3
16	*1.06-1.55*	0.3	66.7%	1
16	1.07-1.11	0.3	*0-100%*	*11*
16	1.35-1.52	0.3	*0-100%*	*10*
16	1.39	*0.2-0.39*	66.7%	3
16	1.1	*0.2-0.38*	66.7%	14
18	*1.08-1.46*	0.3	66.7%	8
20	*1.08-1.41*	0.3	66.7%	9
20	1.3	*0.16-0.36*	66.7%	16
20	1.1	0.2-0.34	66.7%	15
20	1.05	0.3	*0-100%*	*17*
20	1.05	0.4	*0-100%*	*18*

Table 7-5. Operating condition ranges for experimental base set used to train algorithm. The experiment number is used as a reference for the figures legends in the results section.

7.3 Results

While producing this data set for model training, several noteworthy trends were observed regarding the role that gas inputs have on emission outputs. Firstly, NOx emission was contingent on several operating parameters as seen in Fig. 7-3. Each data point plotted contains approximately thirty minutes worth of data averaged out over that time span. The role of thermal input is seen in Fig. 7-3a, where the collective data from all experiments shows NOx values steadily increasing with greater thermal input. This trend is consistent with the known tendency for increased temperature to promote NOx formation, and thermal input typically correlated with increased temperatures in these experiments. Next, λ_{PO} played an important role on NOx (Fig. 7-3b), as these two quantities increased together. The reason for this behavior is that by increasing λ_{PO}, there is a greater presence of NOx precursors (N_2, O_2) in the high-temperature regions of the flame, creating a reaction environment conducive to NOx formation. Finally, increased swirl promoted NOx emission, as seen in Fig. 7-3c. The reasons is that swirl increases the mixing of air into a high temperature zone compared to the axial case.
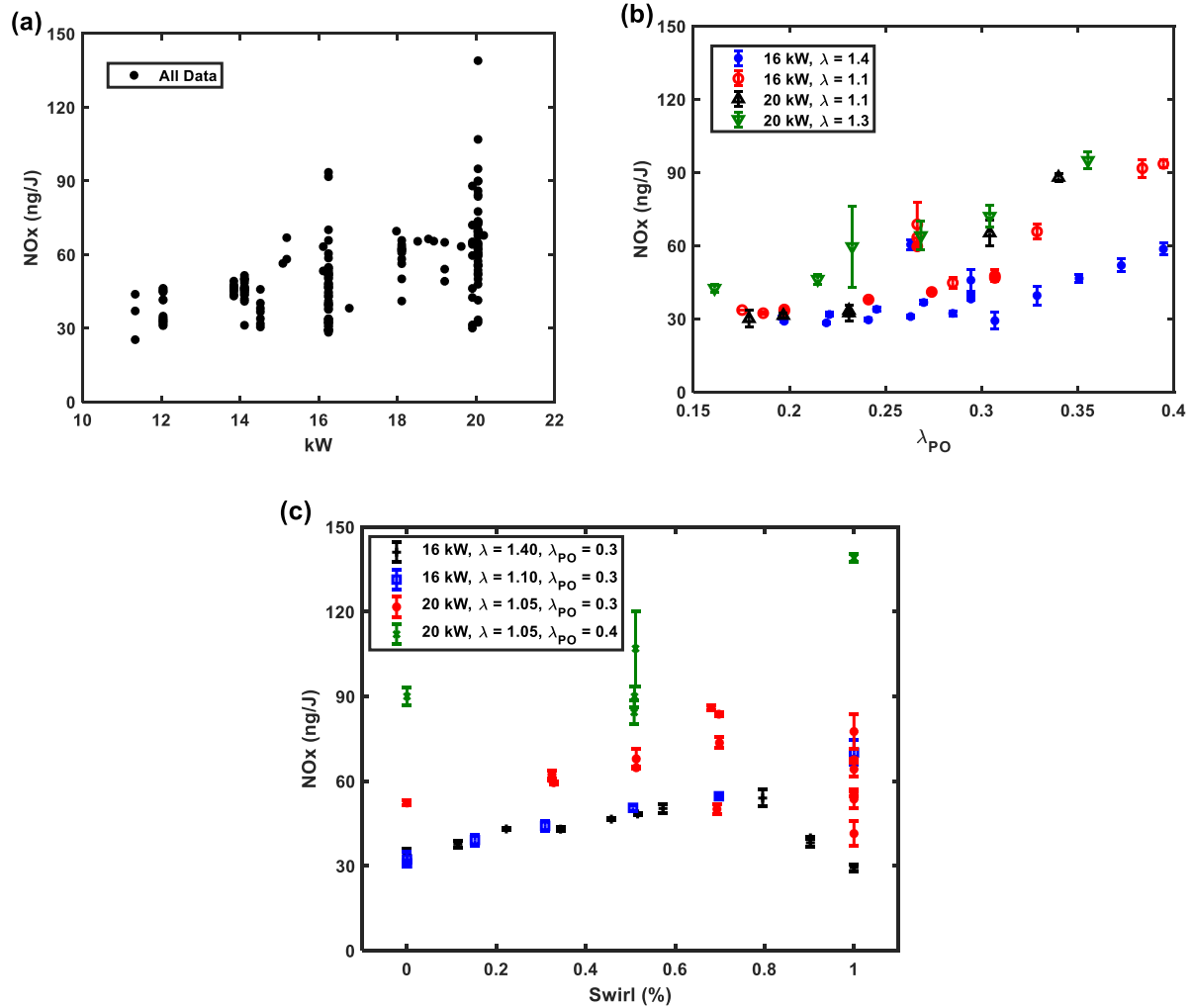
Figure 7-3. Measurements of NOx averaged over a thirty-minute condition vs. a) thermal inputs (kW), b) primary air ratio λ_{PO}, c) swirl %.

The emission of CO was comparatively straightforward, as seen in Fig. 7-4. The dominant factor was overall excess air (Fig. 7-4a). The role of λ_{PO} (Fig. 7-4b) had a secondary effect, but the underlying reasons are not obvious, but is likely related back to the overall excess air.
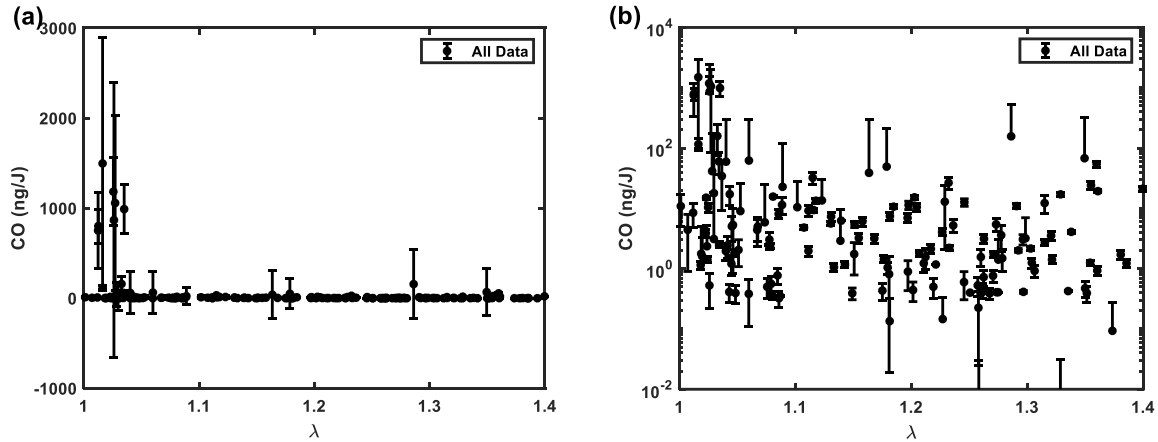
Figure 7-4. Measurements of CO averaged over a thirty-minute condition vs. total air (λ) with emissions shown in a) linear scaling and b) logarithmic scaling.

The emission of PM was similarly increased by reducing the air inputs. For $\lambda < 1.1$, there is significant PM emission as seen in Fig. 7-5a, although there is significant production for $\lambda \geq 1.2$ for cases when λ_{PO} is low. The effect of λ_{PO} on PM can be seen in Fig. 7-5b, where there is an uptick in PM creation for $\lambda_{PO} < 0.25$. These two values work in tandem. When λ is lowered, the λ_{PO} threshold for PM emission is also lowered and vice-versa. There was no correlation observed between swirl and PM (not shown).
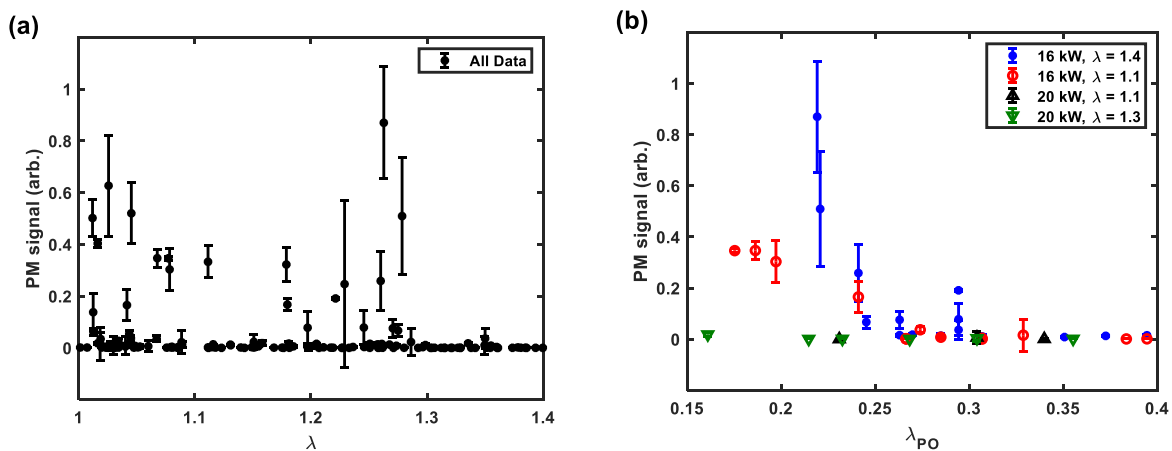
Figure 7-5. Measurements of particulate matter (PM) averaged over a thirty-minute condition vs. a) total air ratio (λ), b) primary air ratio λ_{PO}.

135

7.4 Conclusions

A full test campaign has been performed in a 25-kW combustor using CH_4 fuel and measuring temperature, exhaust gas composition, and pollutants. This data is being used to train a machine learning algorithm, still under development. Several important trends were noted experimentally regarding the effects that primary air ratio and swirl number can have on the production and emission of NOx and PM2.5.

7.5 Supplemental Material

Below is a list of every condition used in the test campaign to train the algorithm. The vast majority of these conditions were for thirty minutes.

Fuel (kW)	SR, Total (λ)	SR, PO (λ)	Swirl %
12	*1.2*	0.3	66.7%
12	*1.25*	0.3	66.7%
12	*1.3*	0.3	66.7%
12	*1.36*	0.3	66.7%
12	*1.39*	0.3	66.7%
12	*1.4*	0.3	66.7%
12	*1.2*	0.3	66.7%
12	*1.25*	0.3	66.7%
12	*1.3*	0.3	66.7%
12	*1.36*	0.3	66.7%
12	*1.39*	0.3	66.7%
12	*1.4*	0.3	66.7%
14	*1.07*	0.3	66.7%
14	*1.12*	0.3	66.7%
14	*1.16*	0.3	66.7%
14	*1.21*	0.3	66.7%
14	*1.25*	0.3	66.7%
14	*1.3*	0.3	66.7%

14	*1.37*	0.3	66.7%
14	*1.07*	0.3	66.7%
14	*1.12*	0.3	66.7%
14	*1.16*	0.3	66.7%
14	*1.21*	0.3	66.7%
14	*1.25*	0.3	66.7%
14	*1.3*	0.3	66.7%
14	*1.37*	0.3	66.7%
16	*1.06*	0.3	66.7%
16	*1.12*	0.3	66.7%
16	*1.16*	0.3	66.7%
16	*1.20*	0.3	66.7%
16	*1.24*	0.3	66.7%
16	*1.28*	0.3	66.7%
16	*1.32*	0.3	66.7%
16	*1.38*	0.3	66.7%
16	*1.47*	0.3	66.7%
16	*1.55*	0.3	66.7%
16	1.07	0.3	*0.0%*
16	1.07	0.3	*15.0%*
16	1.05	0.3	*31.0%*
16	1.04	0.3	*51.0%*
16	1.06	0.3	*70.0%*
16	1.11	0.3	*100.0%*

16	1.39	*0.20*	66.7%
16	1.39	*0.22*	66.7%
16	1.39	*0.24*	66.7%
16	1.39	*0.26*	66.7%
16	1.39	*0.28*	66.7%
16	1.39	*0.31*	66.7%
16	1.39	*0.33*	66.7%
16	1.39	*0.35*	66.7%
16	1.39	*0.37*	66.7%
16	1.39	*0.39*	66.7%
16	1.1	0.2	66.7%
16	1.1	0.24	66.7%
16	1.1	0.27	66.7%
16	1.1	0.31	66.7%
16	1.1	0.33	66.7%
16	1.1	0.37	66.7%
16	1.1	0.38	66.7%
16	1.49	0.3	*0.0%*
16	1.33	0.3	*11.0%*
16	1.36	0.3	*22.0%*
16	1.35	0.3	*34.0%*
16	1.35	0.3	*46.0%*
16	1.36	0.3	*52.0%*
16	1.37	0.3	*57.0%*

16	1.40	0.3	*80.0%*
16	1.43	0.3	*90.0%*
16	1.52	0.3	*100.0%*
18	*1.08*	0.3	66.7%
18	*1.12*	0.3	66.7%
18	*1.15*	0.3	66.7%
18	*1.19*	0.3	66.7%
18	*1.2*	0.3	66.7%
18	*1.25*	0.3	66.7%
18	*1.32*	0.3	66.7%
18	*1.40*	0.3	66.7%
18	*1.46*	0.3	66.7%
20	*1.08*	0.3	66.7%
20	*1.12*	0.3	66.7%
20	*1.15*	0.3	66.7%
20	*1.21*	0.3	66.7%
20	*1.24*	0.3	66.7%
20	*1.28*	0.3	66.7%
20	*1.30*	0.3	66.7%
20	*1.39*	0.3	66.7%
20	*1.41*	0.3	66.7%
20	1.3	0.16	66.7%
20	1.3	0.21	66.7%
20	1.3	0.27	66.7%

20	1.3	0.30	66.7%
20	1.3	0.36	66.7%
20	1.1	0.20	66.7%
20	1.1	0.23	66.7%
20	1.1	0.27	66.7%
20	1.1	0.30	66.7%
20	1.1	0.34	66.7%
20	1.05	0.3	*0.0%*
20	1.05	0.3	*31.0%*
20	1.05	0.3	*50.0%*
20	1.05	0.3	*68.0%*
20	1.05	0.3	*100.0%*
20	1.05	0.4	*0.0%*
20	1.05	0.4	*50.0%*
20	1.05	0.4	*100.0%*
16.3	1.4	0.3	66.7%
11.3	1.4	0.3	66.7%
20	1.4	0.3	66.7%
11.3	1.4	0.3	66.7%
13.8	1.4	0.3	66.7%
18.5	1.4	0.3	66.7%
15.2	1.4	0.3	66.7%
12.05	1.25	0.3	66.7%

14.11	1.24	0.3	66.7%
16.12	1.25	0.3	66.7%
18.11	1.29	0.3	66.7%
20.19	1.27	0.3	66.7%
20.05	1.18	0.3	66.7%
17.89	1.20	0.3	66.7%
16.12	1.15	0.3	66.7%
14.11	1.16	0.3	66.7%
12.05	1.20	0.3	66.7%
14.52	1.39	*0.29*	66.7%
14.52	1.39	*0.27*	66.7%
14.52	1.39	*0.25*	66.7%
14.52	1.39	*0.22*	66.7%
14.52	1.39	*0.20*	66.7%

Table 7-6. All experimental conditions for test campaign which generated data to train the machine learning algorithm.

Chapter 8: Conclusions and Future Work

8.1 Conclusions

This research has developed new modeling capabilities for the prediction of combustion emissions through diverse toolsets ranging from semi-empirical soot modeling for unique flame applications to machine learning algorithms targeting industrial combustion processes at large.

Several notable achievements have been made with regard to soot modeling at high Z_{st}. The first is the demonstration that existing soot-models are inadequate to predict soot fraction under these conditions. Next, the subsequent analysis of the physical-chemical processes in soot formation granted insights into the importance of reversibility. As part of this analysis, the utilization of plotting gas species and soot in equivalence ratio (Φ) space was established as tool which has universal appeal to combustion applications. Developments were made in understanding the high-temperature region prior to the flame where soot particles cannot form and Φ-space was an essential aid in this analysis. Taking this new knowledge together, a semi-empirical framework was proposed which includes soot reversibility as a solution for soot modeling a high Z_{st}. This framework was used to introduce a new model with one-step formation and also to modify two popular semi-empirical models. All three of these models were able to predict blue (soot-free) flames, which is a novel achievement for this field. In addition to offering these modeling tools, a fundamental point has been made that reversibility is an important process which should be considered for soot formation, especially the inception process for all flames (both for low, but especially for, high Z_{st}).

Finally, machine learning techniques offer a fresh approach to modeling complex physical and chemical processes which occur in combustion systems. A large data set has been generated which has demonstrated several important trends for the reactor regarding operational parameters and pollutants of interest such as NOx and PM2.5. Next steps involve model validation and prediction of optimized input conditions for this system.

8.2 Future Work

The research accomplishments here provide significant opportunities for advancement. The developed soot models can and should be applied to other flame types to determine their universal validity. More experimental data could be generated in the counterflow flame, where full soot profiles of intermediate Z_{st} would aid in the optimization of the current model. A proposed immediate step for modeling purposes would be to introduce these models into coflow flames, where there already exists a data set [4] of measured soot fraction across a wide range of Z_{st}. Given that the semi-empirical focus was chosen for its appeal to large-scale applications, these models should also be applied to furnaces, engines, and gas turbines. For these flame types, some measures must be taken to include oxidation reactions. The research included in this dissertation intentionally designed the counterflow flame conditions to focus on soot formation and non-oxidation counteractive effects. Oxidation terms exist in wide variety for semi-empirical models, but use of such terms would require refitting of the empirical constants and would be contingent on which proposed model is used.

In regards to machine learning efforts, future work is already underway, as validation test cases are being run and the model is continually refined. Further tests will examine the ability of

the model to notify operators of needed input changes in real-time. Finally, application of this

model to industrial settings will be pursued.

References

[1] U. Vandsburger, I. Kennedy, I. Glassman, Sooting counterflow diffusion flames with varying oxygen index, Combust. Sci. Technol. 39 (1984) 263-285.

[2] J. Hwang, S. Chung, Growth of soot particles in counterflow diffusion flames of ethylene, Combust. Flame 125 (2001) 752-762.

[3] B. Kumfer, S. Skeen, R. Axelbaum, Soot inception limits in laminar diffusion flames with application to oxy–fuel combustion, Combust. Flame 154 (2008) 546-556.

[4] C. Lou, X. Chen, W. Yan, Y. Tian, B.M. Kumfer, Effect of stoichiometric mixture fraction on soot fraction and emission spectra with application to oxy-combustion, Proc. Combust. Inst. 37 (2019) 4571-4578.

[5] J. Du, R. Axelbaum, The effect of flame structure on soot-particle inception in diffusion flames, Combust. Flame 100 (1995) 367-375.

[6] V.R. Lecoustre, P.B. Sunderland, B.H. Chao, R.L. Axelbaum, Numerical investigation of spherical diffusion flames at their sooting limits, Combust. Flame 159 (2012) 194-199.

[7] Z. Dai, G.M. Faeth, Hydrodynamic suppression of soot formation in laminar coflowing jet diffusion flames, Proc. Combust. Inst. 28 (2000) 2085-2092.

[8] Y. Wang, S.H. Chung, Effect of strain rate on sooting limits in counterflow diffusion flames of gaseous hydrocarbon fuels: Sooting temperature index and sooting sensitivity index, Combust. Flame 161 (2014) 1224-1234.

[9] H. Wang, Formation of nascent soot and other condensed-phase materials in flames, Proc. Combust. Inst. 33 (2011) 41-67.

[10] Y. Wang, A. Raj, S.H. Chung, Soot modeling of counterflow diffusion flames of ethylene-based binary mixture fuels, Combust. Flame 162 (2015) 586-596.

[11] M. Sander, R.I. Patterson, A. Braumann, A. Raj, M. Kraft, Developing the PAH-PP soot particle model using process informatics and uncertainty propagation, Proc. Combust. Inst. 33 (2011) 675-683.

[12] A. Cuoci, A. Frassoldati, T. Faravelli, E. Ranzi, Formation of soot and nitrogen oxides in unsteady counterflow diffusion flames, Combust. Flame 156 (2009) 2010-2022.

[13] V. Chernov, M.J. Thomson, S.B. Dworkin, N.A. Slavinskaya, U. Riedel, Soot formation with C1 and C2 fuels using an improved chemical mechanism for PAH growth, Combust. Flame 161 (2014) 592-601.

[14] D. Chen, Z. Zainuddin, E. Yapp, J. Akroyd, S. Mosbach, M. Kraft, A fully coupled simulation of PAH and soot growth with a population balance model, Proc. Combust. Inst. 34 (2013) 1827-1835.

[15] C. Saggese, S. Ferrario, J. Camacho, A. Cuoci, A. Frassoldati, E. Ranzi, H. Wang, T. Faravelli, Kinetic modeling of particle size distribution of soot in a premixed burner-stabilized stagnation ethylene flame, Combust. Flame 162 (2015) 3356-3369.

[16] J. Appel, H. Bockhorn, M. Frenklach, Kinetic modeling of soot formation with detailed chemistry and physics: laminar premixed flames of C 2 hydrocarbons, Combust. Flame 121 (2000) 122-136.

[17] A. Fluent, 12.0 Theory Guide, Ansys Inc 5 (2009).

[18] K.B. Lee, M.W. Thring, J.M. Beér, On the rate of combustion of soot in a laminar soot flame, Combust. Flame 6 (1962) 137-145.

[19] S.A. Skeen, G. Yablonsky, R.L. Axelbaum, Characteristics of non-premixed oxygen-enhanced combustion: II. Flame structure effects on soot precursor kinetics resulting in soot-free flames, Combust. Flame 157 (2010) 1745-1752.

[20] P. Elvati, A. Violi, Thermodynamics of poly-aromatic hydrocarbon clustering and the effects of substituted aliphatic chains, Proc. Combust. Inst. 34 (2013) 1837-1843.

[21] K.O. Johansson, M.P. Head-Gordon, P.E. Schrader, K.R. Wilson, H.A. Michelsen, Resonance-stabilized hydrocarbon-radical chain reactions may explain soot inception and growth, Science 361 (2018) 997-1000.

[22] M.E. Mueller, G. Blanquart, H. Pitsch, Hybrid Method of Moments for modeling soot formation and growth, Combust. Flame 156 (2009) 1143-1155.

[23] Q. Zhang, H. Guo, F. Liu, G. Smallwood, M. Thomson, Modeling of soot aggregate formation and size distribution in a laminar ethylene/air coflow diffusion flame with detailed PAH chemistry and an advanced sectional aerosol dynamics model, Proc. Combust. Inst. 32 (2009) 761-768.

[24] N.A. Eaves, S.B. Dworkin, M.J. Thomson, The importance of reversibility in modeling soot nucleation and condensation processes, Proc. Combust. Inst. 35 (2015) 1787-1794.

[25] A. Raj, M. Celnik, R. Shirley, M. Sander, R. Patterson, R. West, M. Kraft, A statistical approach to develop a detailed soot growth model using PAH characteristics, Combust. Flame 156 (2009) 896-913.

[26] A. Raj, M. Sander, V. Janardhanan, M. Kraft, A study on the coagulation of polycyclic aromatic hydrocarbon clusters to determine their collision efficiency, Combust. Flame 157 (2010) 523-534.

[27] H.-B. Zhang, X. You, H. Wang, C.K. Law, Dimerization of polycyclic aromatic hydrocarbons in soot nucleation, The Journal of Physical Chemistry A 118 (2014) 1287-1292.

[28] I.M. Kennedy, Models of soot formation and oxidation, Prog. Energy Combust. Sci. 23 (1997) 95-132.

[29] S.J. Brookes, J.B. Moss, Predictions of soot and thermal radiation properties in confined turbulent jet diffusion flames, Combust. Flame 116 (1999) 486-503.

[30] R. Hall, M. Smooke, M. Colket, Predictions of soot dynamics in opposed jet diffusion flames, Physical and Chemical Aspects of Combustion: A Tribute to Irvin Glassman 4 (1997) 189-229.

[31] C.W. Lautenberger, J.L. de Ris, N.A. Dembsey, J.R. Barnett, H.R. Baum, A simplified model for soot formation and oxidation in CFD simulation of non-premixed hydrocarbon flames, Fire Safety Journal 40 (2005) 141-176.

[32] T. Beji, J.P. Zhang, M. Delichatsios, Determination of Soot Formation Rate from Laminar Smoke Point Measurements, Combust. Sci. Technol. 180 (2008) 927-940.

[33] T. Beji, J.P. Zhang, W. Yao, M. Delichatsios, A novel soot model for fires: Validation in a laminar non-premixed flame, Combust. Flame 158 (2011) 281-290.

[34] W. Yao, J. Zhang, A. Nadjai, T. Beji, M.A. Delichatsios, A global soot model developed for fires: Validation in laminar flames and application in turbulent pool fires, Fire safety journal 46 (2011) 371-387.

[35] W. Yao, J. Zhang, A. Nadjai, T. Beji, M. Delichatsios, Development and validation of a global soot model in turbulent jet flames, Combust. Sci. Technol. 184 (2012) 717-733.

[36] I. Khan, G. Greeves, D. Probert, Prediction of soot and nitric oxide concentrations in diesel engine exhaust, Air Pollution Control in Transport Engines C 142 (1971) 205-217.

[37] I. Khan, G. Greeves, A method for calculating the formation and combustion of soot in diesel engines, Heat transfer in flames 25 (1974).

[38] B. Simmons, A. Williams, A shock tube investigation of the rate of soot formation for benzene, toluene, and toluene/n-heptane mixtures, Combust. Flame 71 (1988) 219-232.

[39] P. Coelho, M. Carvalho, Modeling of soot formation and oxidation in turbulent diffusion flames, Journal of thermophysics and heat transfer 9 (1995) 644-652.

[40] R. Backreedy, L. Fletcher, L. Ma, M. Pourkashanian, A. Williams, Modelling pulverised coal combustion using a detailed coal combustion model, Combust. Sci. Technol. 178 (2006) 763-787.

[41] L. Chen, A.F. Ghoniem, Modeling CO2 Chemical Effects on CO Formation in Oxy-Fuel Diffusion Flames Using Detailed, Quasi-Global, and Global Reaction Mechanisms, Combust. Sci. Technol. 186 (2014) 829-848.

[42] L. Álvarez, M. Gharebaghi, M. Pourkashanian, A. Williams, J. Riaza, C. Pevida, J.J. Pis, F. Rubiera, CFD modelling of oxy-coal combustion in an entrained flow reactor, Fuel Processing Technology 92 (2011) 1489-1497.

[43] M. Delichatsios, A phenomenological model for smoke-point and soot formation in laminar flames, Combust. Sci. Technol. 100 (1994) 283-298.

[44] R. Axelbaum, W. Flower, C. Law, Dilution and temperature effects of inert addition on soot formation in counterflow diffusion flames, Combust. Sci. Technol. 61 (1988) 51-73.

[45] R.L. Axelbaum, C.K. Law, Soot formation and inert addition in diffusion flames, Symp. (Int.) Combust. 23 (1991) 1517-1523.

[46] B. Kumfer, S. Skeen, R. Chen, R. Axelbaum, Measurement and analysis of soot inception limits of oxygen-enriched coflow flames, Combust. Flame 147 (2006) 233-242.

[47] K.M. Leung, R.P. Lindstedt, W.P. Jones, A simplified reaction mechanism for soot formation in nonpremixed flames, Combust. Flame 87 (1991) 289-305.

[48] P.A. Tesner, T.D. Smegiriova, V.G. Knorre, Kinetics of dispersed carbon formation, Combust. Flame 17 (1971) 253-260.

[49] Ahmad, S. Plee, J. Myers, Computation of nitric oxide and soot emissions from turbulent diffusion flames, Journal of engineering for gas turbines and power 107 (1985) 49.

[50] J.B. Moss, C.D. Stewart, K.J. Syed, Flowfield modelling of soot formation at elevated pressure, Symp. (Int.) Combust. 22 (1989) 413-423.

[51] A. Datta, A. Saha, Contributions of self-absorption and soot on radiation heat transfer in a laminar methane—air diffusion flame, Proceedings of the Institution of Mechanical Engineers, Part A: Journal of Power and Energy 221 (2007) 955-970.

[52] G.H. Yeoh, R.K.K. Yuen, S.C.P. Chueng, W.K. Kwok, On modelling combustion, radiation and soot processes in compartment fires, Building and Environment 38 (2003) 771-785.

[53] A. Cuoci, A. Frassoldati, T. Faravelli, E. Ranzi, Kinetic modeling of soot formation in turbulent nonpremixed flames, Environmental Engineering Science 25 (2008) 1407-1422.

[54] I.M. Kennedy, W. Kollmann, J.Y. Chen, A model for soot formation in a laminar diffusion flame, Combust. Flame 81 (1990) 73-85.

[55] I.M. Kennedy, The evolution of a soot aerosol in a counterflow diffusion flame, Combust. Flame 68 (1987) 1-16.

[56] P.R. Lindstedt, Simplified soot nucleation and surface growth steps for non-premixed flames, Soot Formation in Combustion, Springer1994, pp. 417-441.

[57] Z. Wen, S. Yun, M.J. Thomson, M.F. Lightstone, Modeling soot formation in turbulent kerosene/air jet diffusion flames, Combust. Flame 135 (2003) 323-340.

[58] B. Wu, S.P. Roy, X. Zhao, Detailed modeling of a small-scale turbulent pool fire, Combust. Flame 214 (2020) 224-237.

[59] K.M. Pang, M. Jangi, X.-S. Bai, J. Schramm, J.H. Walther, Modelling of diesel spray flames under engine-like conditions using an accelerated Eulerian Stochastic Field method, Combust. Flame 193 (2018) 363-383.

[60] S.F. Fernandez, C. Paul, A. Sircar, A. Imren, D.C. Haworth, S. Roy, M.F. Modest, Soot and spectral radiation modeling for high-pressure turbulent spray flames, Combust. Flame 190 (2018) 402-415.

[61] A. Felden, E. Riber, B. Cuenot, Impact of direct integration of Analytically Reduced Chemistry in LES of a sooting swirled non-premixed combustor, Combust. Flame 191 (2018) 270-286.

[62] M.A. Chishty, M. Bolla, E.R. Hawkes, Y. Pei, S. Kook, Soot formation modelling for n-dodecane sprays using the transported PDF model, Combust. Flame 192 (2018) 101-119.

[63] C. Paul, S. Ferreyro Fernandez, D.C. Haworth, S. Roy, M.F. Modest, A detailed modeling study of radiative heat transfer in a heavy-duty diesel engine, Combust. Flame 200 (2019) 325-341.

[64] F. Nmira, J. Consalvi, R. Demarco, L. Gay, Assessment of semi-empirical soot production models in C 1–C 3 axisymmetric laminar diffusion flames, Fire Safety Journal 73 (2015) 76-90.

[65] F. Bisetti, G. Blanquart, M.E. Mueller, H. Pitsch, On the formation and early evolution of soot in turbulent nonpremixed flames, Combust. Flame 159 (2012) 317-335.

[66] S.A. Skeen, G. Yablonsky, R.L. Axelbaum, Characteristics of non-premixed oxygen-enhanced combustion: I. The presence of appreciable oxygen at the location of maximum temperature, Combust. Flame 156 (2009) 2145-2152.

[67]

V. Lecoustre, P. Sunderland, B.-H. Chao, D. Urban, D. Stocker, R. Axelbaum. Effects of C/O Ratio and Temperature on Sooting Limits of Spherical Diffusion Flames. In: editor^editors. 46th AIAA Aerospace Sciences Meeting and Exhibit; 2008. p. 827.

[68] B. Chao, S. Liu, R. Axelbaum, On soot inception in nonpremixed flames and the effects of flame structure, Combust. Sci. Technol. 138 (1998) 105-135.

[69] Y. Wang, S.H. Chung, Soot formation in laminar counterflow flames, Prog. Energy Combust. Sci. 74 (2019) 152-238.

[70] D.X. Du, R.L. Axelbaum, C.K. Law, Experiments on the sooting limits of aerodynamically-strained diffusion flames, Symp. (Int.) Combust. 22 (1989) 387-394.

[71] R.J. Kee, F.M. Rupley, J.A. Miller, Chemkin-II: A Fortran chemical kinetics package for the analysis of gas-phase chemical kinetics, Sandia National Labs., Livermore, CA (USA), 1989.

[72] A.N. Osiptsov, Investigation of regions of unbounded growth of the particle concentration in disperse flows, Fluid Dynamics 19 (1984) 378-385.

[73] G. Continillo, W.A. Sirignano, Counterflow spray combustion modeling, Combust. Flame 81 (1990) 325-340.

[74] E. Gutheil, W.A. Sirignano, Counterflow Spray Combustion Modeling with Detailed Transport and Detailed Chemistry, Combust. Flame 113 (1998) 92-105.

[75] F.N. Egolfopoulos, C.S. Campbell, Dynamics and structure of dusty reacting flows: inert particles in strained, laminar, premixed flames, Combust. Flame 117 (1999) 206-226.

[76] L.P. Gao, Y. D'Angelo, I. Silverman, A. Gome, M.D. Smooke, Quantitative comparison of detailed numerical computations and experiments in counterflow spray diffusion flames, Symp. (Int.) Combust. 26 (1996) 1739-1746.

[77] I. Hernández, G. Lecocq, D. Poitou, E. Riber, B. Cuenot, Computations of soot formation in ethylene/air counterflow diffusion flames and its interaction with radiation, Comptes Rendus Mécanique 341 (2013) 238-246.

[78] F. Liu, H. Guo, G. J. Smallwood, M. El Hafi, Effects of gas and soot radiation on soot formation in counterflow ethylene diffusion flames, Journal of Quantitative Spectroscopy and Radiative Transfer 84 (2004) 501-511.

[79] K. Gleason, F. Carbone, A. Gomez, Effect of temperature on soot inception in highly controlled counterflow ethylene diffusion flames, Combust. Flame 192 (2018) 283-294.

[80] J.B. Moss, C.D. Stewart, K.J. Young, Modeling soot formation and burnout in a high temperature laminar diffusion flame burning under oxygen-enriched conditions, Combust. Flame 101 (1995) 491-500.

[81] Y. Wang, S.H. Chung, Strain rate effect on sooting characteristics in laminar counterflow diffusion flames, Combust. Flame 165 (2016) 433-444.

[82] L. Xu, F. Yan, M. Zhou, Y. Wang, S.H. Chung, Experimental and soot modeling studies of ethylene counterflow diffusion flames: Non-monotonic influence of the oxidizer composition on soot formation, Combust. Flame 197 (2018) 304-318.

[83] K.C. Kalvakala, V.R. Katta, S.K. Aggarwal, Effects of oxygen-enrichment and fuel unsaturation on soot and NOx emissions in ethylene, propane, and propene flames, Combust. Flame 187 (2018) 217-229.

[84] D.X. Du, R.L. Axelbaum, C.K. Law, Soot formation in strained diffusion flames with gaseous additives, Combust. Flame 102 (1995) 11-20.

[85] P.R. Johnson, R.K. Chakrabarty, B.M. Kumfer, Evaluation of semi-empirical soot models for nonpremixed flames with increased stoichiometric mixture fraction and strain, Combust. Flame 219 (2020) 70-85.

[86] P. Tan, J. Xia, C. Zhang, Q. Fang, G. Chen, Modeling and reduction of NOX emissions for a 700 MW coal-fired boiler with the advanced machine learning method, Energy 94 (2016) 672-679.

[87] E. Lughofer, V. Macián, C. Guardiola, E.P. Klement, Identifying static and dynamic prediction models for NOx emissions with evolving fuzzy systems, Applied Soft Computing 11 (2011) 2487-2500.

[88] F. Wang, S. Ma, H. Wang, Y. Li, J. Zhang, Prediction of NOX emission for coal-fired boilers based on deep belief network, Control Engineering Practice 80 (2018) 26-35.

[89] Y. Lv, J. Liu, T. Yang, D. Zeng, A novel least squares support vector machine ensemble model for NOx emission prediction of a coal-fired boiler, Energy 55 (2013) 319-329.

[90] P. Tan, C. Zhang, J. Xia, Q. Fang, G. Chen, NO$_X$ Emission Model for Coal-Fired Boilers Using Principle Component Analysis and Support Vector Regression, JOURNAL OF CHEMICAL ENGINEERING OF JAPAN 49 (2016) 211-216.

[91] G. Alcan, E. Yilmaz, M. Unel, V. Aran, M. Yilmaz, C. Gurel, K. Koprubasi, Estimating Soot Emission in Diesel Engines Using Gated Recurrent Unit Networks, IFAC-PapersOnLine 52 (2019) 544-549.

[92] M. Potenza, M. Milanese, F. Naccarato, A. de Risi, In-cylinder soot concentration measurement by Neural Network Two Colour technique (NNTC) on a GDI engine, Combustion and Flame 217 (2020) 331-345.

[93]

J. Badra, F. Khaled, M. Tang, Y. Pei, J. Kodavasal, P. Pal, O. Owoyele, C. Fuetterer, M. Brenner, A. Farooq. Engine Combustion System Optimization Using CFD and Machine Learning: A Methodological Approach. In: editor^editors. ASME 2019 Internal Combustion Engine Division Fall Technical Conference; 2019. p.

[94] G. Mao, C. Zhang, K. Shi, P. Wang, Prediction of the performance and exhaust emissions of ethanol-diesel engine using different neural network, Energy Sources, Part A: Recovery, Utilization, and Environmental Effects, doi:10.1080/15567036.2019.1656307(2019) 1-15.

[95] W. Pan, M. Korkmaz, J. Beeckmann, H. Pitsch, Nonlinear Identification Modeling for PCCI Engine Emissions Prediction Using Unsupervised Learning and Neural Networks, SAE International, 2020.

[96] B. Liu, J. Hu, F. Yan, R.F. Turkson, F. Lin, A novel optimal support vector machine ensemble model for NOX emissions prediction of a diesel engine, Measurement 92 (2016) 183-192.

[97] W. Yu, F. Zhao, W. Yang, H. Xu, Integrated analysis of CFD simulation data with K-means clustering algorithm for soot formation under varied combustion conditions, Applied Thermal Engineering 153 (2019) 299-305.

[98]

M.A. Bunyamin, K.S. Yap, N.L.A.A. Aziz, S.K. Tiong, S.Y. Wong, M.F. Kamal. A hybrid genetic algorithm and linear regression for prediction of NOx emission in power generation plant. In: editor^editors. IOP Conference Series: Earth and Environmental Science; 2013: IOP Publishing. p. 012101.

[99] P. Tan, B. He, C. Zhang, D. Rao, S. Li, Q. Fang, G. Chen, Dynamic modeling of NOX emission in a 660 MW coal-fired boiler with long short-term memory, Energy 176 (2019) 429-436.

[100] L.-G. Zheng, H. Zhou, K.-F. Cen, C.-L. Wang, A comparative study of optimization algorithms for low NOx combustion modification at a coal-fired utility boiler, Expert Systems with Applications 36 (2009) 2780-2793.

[101] C. Wang, Y. Liu, S. Zheng, A. Jiang, Optimizing combustion of coal fired boilers for reducing NOx emission using Gaussian Process, Energy 153 (2018) 149-158.

[102] H. Zhou, K. Cen, J. Fan, Modeling and optimization of the NOx emission characteristics of a tangentially fired boiler with artificial neural networks, Energy 29 (2004) 167-183.

[103] Y. Lv, T. Yang, J. Liu, An adaptive least squares support vector machine model with a novel update for NOx emission prediction, Chemometrics and Intelligent Laboratory Systems 145 (2015) 103-113.

[104] Z. Hao, C. Kefa, M. Jianbo, Combining neural network and genetic algorithms to optimize low NOx pulverized coal combustion, Fuel 80 (2001) 2163-2169.

[105] N. Li, G. Lu, X. Li, Y. Yan, Prediction of NOx Emissions from a Biomass Fired Combustion Process Based on Flame Radical Imaging and Deep Learning Techniques, Combustion Science and Technology 188 (2016) 233-246.

[106] Z. Han, M.M. Hossain, Y. Wang, J. Li, C. Xu, Combustion stability monitoring through flame imaging and stacked sparse autoencoder based deep neural network, Applied Energy 259 (2020) 114159.

[107] Z. Li, S.H. Lam Yim, K.-F. Ho, High temporal resolution prediction of street-level PM2.5 and NOx concentrations using machine learning approach, Journal of Cleaner Production, doi:https://doi.org/10.1016/j.jclepro.2020.121975(2020) 121975.

[108] T. Ren, M.F. Modest, A. Fateev, G. Sutton, W. Zhao, F. Rusu, Machine learning applied to retrieval of temperature and concentration distributions from infrared emission measurements, Applied Energy 252 (2019) 113448.

[109] W. Tamas, G. Notton, C. Paoli, M.-L. Marie-Laure Nivet, C. Voyant, Hybridization of Air Quality Forecasting Models Using Machine Learning and Clustering: An Original Approach to Detect Pollutant Peaks, Aerosol and Air Quality Research 16 (2016) 405-416.

[110] H.O. Garcés, J. Abreu, P. Gómez, C. Carrasco, L. Arias, A.J. Rojas, A. Fuentes, Energy Efficiency Monitoring in a Coal Boiler Based on Optical Variables and Artificial Intelligence, IFAC-PapersOnLine 50 (2017) 13904-13909.

[111] M.L. Holtmeyer, G. Li, B.M. Kumfer, S. Li, R.L. Axelbaum, The Impact of Biomass Cofiring on Volatile Flame Length, Energy & Fuels 27 (2013) 7762-7771.